University of São Paulo
Luiz de Queiroz College of Agriculture

Pedogenesis, clay mineralogy, and silicon geochemistry in hypersaline tidal flat soils on the Brazilian coast

Lucas Resmini Sartor

Thesis presented to obtain the degree of Doctor in Science. Area: Soils and Plant Nutrition

Piracicaba
2018

Lucas Resmini Sartor
Agronomist

Pedogenesis, clay mineralogy, and silicon geochemistry in hypersaline tidal flat soils on the Brazilian coast

versão revisada de acordo com a resolução CoPGr 6018 de 2011

Advisor:
Prof. Dr. TIAGO OSÓRIO FERREIRA

Thesis presented to obtain the degree of Doctor in Science. Area: Soils and Plant Nutrition

Piracicaba
2018

Dados Internacionais de Catalogação na Publicação
DIVISÃO DE BIBLIOTECA – DIBD/ESALQ/USP

Sartor, Lucas Resmini

Pedogenesis, clay mineralogy, and silicon geochemistry in hypersaline tidal flat soils on the Brazilian coast / Lucas Resmini Sartor. - - versão revisada de acordo com a resolução CoPGr 6018 de 2011. - - Piracicaba, 2018.

90 p.

Tese (Doutorado) - - USP / Escola Superior de Agricultura “Luiz de Queiroz”.

1. Processos redox 2. Feições redoximórficas 3. Argilominerais 4. Áreas úmidas 5. Interestratificados I. Título

ACKNOWLEDGEMENTS

I would like to acknowledge and dedicate this dissertation to my family, especially my parents Eloi and Rose and my brother Bruno, for all support over these years, without which this dissertation would never have been realized.

This work was funded cooperatively by São Paulo Research Foundation (FAPESP)/CAPES. I am grateful for the financial support and the doctorate and research internship abroad grants (2014/11776-2, 2016/09024-8, and 2016/21026-6).

Special thanks are extended to my advisor Tiago O. Ferreira, and my supervisors Robert Graham and Samantha Ying from the University of California Riverside for all guidance with the project and friendship.

I am also appreciative to professors Antonio Azevedo, Marcelo Alves, and Pablo Vidal Torrado.

I would like to thank my friends Gabriel Andrade, Rodrigo Yeis, Marcio Nunes, Ana Paula Bettoni, Renata Beltz PG, Cybelle Oliveira, Jean Santos, Leandro Almeida, Renato Paiva, Gabriel Nuto, Hermano Melo, Laís Zayas, Felipe Lurial, Amy Salvador, Nathan Jumps, and Claudia Avila. Thanks to my friends from GRM Xapadão: Édiño, M'Boi, Diz-graça, K-pa, Q-ñé, Péd-Pano, Geleca, D-k-π-tado, Pagódiz, Lixero, and Vidi-baxo.

Special thanks to Leandro Goia for all help in the laboratory and field work.

SUMMARY

RESUMO

Pedogênese, mineralogia da fração argila e geoquímica de silício em solos de planícies hipersalinas da costa brasileira

Planícies hipersalinas costeiras (PHCs) são ecossistemas transicionais comumente encontrados em regiões áridas e semiárias. Estes ambientes são encontrados em várias regiões do mundo, tais como Oceania (e.g. Austrália e Nova Caledónia), África (e.g. Senegal, Gambia e Madagascar), América Central (e.g. Nicarágua), América do Sul (e.g. Equador e as costas norte, nordeste e sudeste do Brasil). Por estarem posicionados na transição entre os ecossistemas marinhos e de terras altas, os solos de PHCs devem exercer um controle biogeoquímico na ciclagem de nutrientes (e.g. Si e Fe), afetando o fluxo dos mesmo para o oceano e ecossitemas adjacentes. Este controle biogeoquímico é governado pelas condições fisico-químicas do meio (e.g. pH e salinidade) e pelos processos pedogenéticos atuantes nos solos (e.g. processos redox). Desta forma, o estudo da fração coloidal, da pedogênese e da distribuição do Si nos diferentes componentes do solo possibilita caracterizar detalhadamente os solos de PHCs e desvendar os processos que controlam a dinâmica de Si no ambiente. Portanto, duas PHCs localizadas na costa brasileira foram estudadas e os resultados estão apresentados em três capítulos nesta tese. O primeiro capítulo teve por objetivo investigar a pedogênese em PHCs com base em estudos morfológicos e extrações sequenciais de Fe e Mn. O segundo discute a geoquímica de silício nos solos com base em extrações sequenciais, MEV e modelagem de raios-X da fração argila fina. O terceiro capítulo discorre sobre as características, distribuição e gênese de argilominerais nos solos com base em modelagem de raios-X, MET-EDS, FTIR e FRX. As reações redox parecem controlar a evolução pedogenética nestes solos, as quais levam à mobilização ascendente de Fe^{2+} e Mn^{2+} nos perfis, oxidação da pirita e, consequentemente, transformação dos horizontes mais profundos. Estes processos também são responsáveis pela formação de oxihidróxidos de Fe e Mn nos horizontes superiores dos perfis de solo, levando à um controle do Si por reações de co-precipitação e adsorção envolvendo oxihidróxidos de Fe. O Si associado aos oxihidróxidos de Fe e silicatos amorfos são os principais componentes da fração mais solúvel de Si nos solos estudados. As condições ambientais nas PHCs são favoráveis às transformações minerais. Os dados indicam que a caulinita é alterada para esmectitas magnesianas por processos de interestratificação, removendo Si da solução do solo.

Palavras-chave: Processos redox; Feições redoximórficas; Argilominerais; Áreas úmidas; Interestratificados

ABSTRACT

Pedogenesis, clay mineralogy, and silicon geochemistry in hypersaline tidal flat soils on the Brazilian coast

Hypersaline tidal flats (HTFs) are transitional ecosystems commonly occurring in arid and semiarid coastal areas. (e.g. Australia and New Caledonia), Africa (e.g. Senegal, Gambia, and Madagascar), Central America (e.g. Nicaragua), South America (e.g. Ecuador and on the north, northeast, and southeast Brazilian coasts). Due to their location, HTFs might exert biogeochemical control over cycling of nutrients (e.g. Fe and Si) across the land to ocean transition, accelerating or retarding the nutrient export to the ocean and other adjacent ecosystems. This biogeochemical control is governed by soil physicochemical conditions (e.g. pH and salinity) and pedogenesis (e.g. redox processes). Thus, study of the soil coloidal fraction, the pedogenic processes, and the distribution of Si in the different soil components can provide a detailed characterization of HTF soils and give insights into the Si dynamics in these environments. In view of this, two HTFs on the Brazilian coast were studied on the Brazilian coast and the data are presented here. The first chapter aims to investigate the pedogenesis in HTF soils based on detailed morphological descriptions and Fe and Mn sequential extractions. The second chapter discusses silicon geochemistry in HTF soils based on sequential extractions, SEM, and XRD modeling of the fine clay fraction. And lastly, the third one reports the characteristics, distribution, and genesis of clay minerals in HTF soils on the basis of XRD modeling, TEM-EDS, FTIR, and XRF analysis. Redox reactions control the pedogenic evolution in HTF soils. These processes lead to a mobilization of Fe^{2+} and Mn^{2+} upward in the soils profiles, followed by oxidation and precipitation of Fe and Mn oxyhydroxides. These reactions, along with pyrite oxidation, lead to a transformation of the deeper soil horizons. Formation of Fe oxyhydroxides in the uppermost soil horizons exerts control on Si dynamics by co-precipitation and adsorption reactions. Together, Si associated with Fe oxyhydroxides and amorphous silicates are the main components of the readily soluble Si pool in HTF soils. The environmental conditions are conducive to clay transformations in the soils. Our data indicate that kaolinite is progressively altered to Mg-rich smectite through mixed-layering, withdrawing Si from the soil porewater.

Keywords: Redox processes; Redoximorphic features; Clay minerals; Wetlands; Mixed-layered minerals

1. INTRODUCTION

Wetlands are complex ecosystems driven by many physical, chemical, and biological processes. Approximately 6 % of Earth's surface is covered by wetlands. They are a critical feature of the global landscape because of their role in regulating global biogeochemical cycles (Reddy and DeLaune, 2008). Because of permanent or temporary water saturation, chemical, and biological processes in wetlands dramatically differ from those in terrestrial ecosystems. Hypersaline tidal flats (HTFs) and mangroves are among the globally widespread coastal wetlands (Giri et al., 2010; Albuquerque et al., 2014a).

These two ecosystems are the dominant wetlands on the Brazilian coast and are commonly associated in the estuary. Previous studies showed that the formation of HTFs is a natural process in which mangrove is replaced by a new hypersaline environment (Marius, 1985). Although HTFs may have been formed after mangrove dieback, they are substantially different with respect to vegetation, soils, and hydrology. The infrequent flooding events at HTFs along with high evaporation rates can cause an increase in soil salinity up to five times normal seawater (Ridd and Stieglitz, 2002), leading to a sparse colonization of halophytes on the area and formation of hypersaline soils. When compared with other coastal ecosystems, studies of these HTFs are recent and still very little is known, specifically with regard to ecosystem formation and soil genesis (Albuquerque et al., 2014a).

Since HTF soils represent a link between terrestrial and aquatic environment, they attract special attention for cycling of elements across the land to ocean transition. Pedologic studies can certainly bring light to understand these geochemical processes and are capable to unveil important basic information about the soil system (Barbiero et al., 2008; Furquim et al., 2017). For instance, Fe, Mn, and S dynamics are strongly affected by redox reactions in HTF soils (Albuquerque et al., 2014b), since they act as electron acceptors during microbial respiration under suboxic and anoxic conditions (Reddy and DeLaune, 2008). In addition, these pedogenic processes influence the biogeochemical dynamics of Si (Saccone et al., 2007; Loucaides et al. 2008; Cornelis et al., 2014). Silicon is an abundant element in the Earth crust and one of the most important elements for the marine primary production (Kristiansen and Hoell, 2002; Struyf and Conley, 2009). Reactions involving Si in HTF soils are poorly understood and are a relevant approach to better assess the Si terrestrial fluxes.

Clay minerals are also extremely important in these ecosystems since clay formation impacts Si dynamic in soils through transformation and neoformation processes (Dixit et al.,

2001; Presti and Michalopoulos, 2008; Andrade et al., 2018). These evaporative environments tend to form disordered clays with complex structure, such as mixed-layered and trioctahedral minerals (Hover et al., 1999). Mixed-layered minerals are commonly found in a wide range of environments, like sedimentary basins and surface environments (lacustrine deposits, saline-alkaline soils, and weathered saprolite), and may also exist in HTF soils.

Therefore, three chapter are presented here to characterize and give insights into the functioning of HTF soils:

Chapter 1: Investigates the pedogenesis in HTF soils based on morphological and geochemical (Fe and Mn) studies;

Chapter 2: characterizes and investigates the formation and distribution of the readily soluble Si pool in HTF soils;

Chapter 3: investigates the clay mineralogy of HTF soils and its formation processes.

References

Albuquerque, A.G.B.M., Ferreira, T.O., Cabral, R.L., Nóbrega, G.N., Romero, R.E., Meireles, A.J.A., Otero, X.L., 2014a. Hypersaline tidal flats (*apicum* ecosystems): the weak link in the tropical wetlands chain. Environ. Rev. 22, 1-11.

Albuquerque, A.G.B.M., Ferreira, T.O., Nóbrega, G.N., Romero, R.E., Souza Júnior, V.S., Meireles, A.J.A., Otero, X.L., 2014b. Soil genesis on hypersaline tidal flats (HTF ecosystem) in a tropical semi-arid estuary (Ceará, Brazil). Soil Res. 52, 140-154.

Andrade, G.R.P., Cuadros, J., Partiti, C.S.M., Cohen, R., Vidal-Torrado, P., 2018. Sequential mineral transformation from kaolinite to Fe-illite in two Brazilian mangrove soils. Geoderma 309, 84-99.

Barbiéro, L., Rezende Filho, A., Furquim, S.A.C., Furian, S., Sakamoto, A.Y., Valles, V., Graham, R.C., Fort, M., Ferreira, R.P.D., Queiroz Neto, J.P., 2008. Soil morphological control on saline and freshwater lake hydrogeochemistry in the Pantanal of Nhecolândia, Brazil. Geoderma 148, 91-106.

Cornelis, J.T., Dumon, M., Tolossa, A.R., Delvaux, B., Deckers, J., Van Ranst, E., 2014. The effect of pedological conditions on the sources and sinks of silicon in the Vertic Planosols in south-western Ethiopia. Catena 112, 131-138.

Dixit, S., Van Cappellen, P., van Bennekom, A.J., 2001. Processes controlling solubility of biogenic silica and pore water build-up of silicic acid in marine sediments. Mar. Chem. 73, 333-352.

Furquim, S.A.C., Santos, M.A., Vidoca, T.T., Balbino, M.A., Cardoso, E.L., 2017. Salt-affected soils evolution and fluvial dynamics in the Pantanal wetland, Brazil. Geoderma 286, 139-152.

Giri, C., Ochieng, E., Tieszen, L.L., Zhu, Z., Singh, A., Loveland, T., Masek, L., 2010. Status and distribution of mangrove forests of the world using earth observation satellite data. Global Ecol. Biogeogr. 20, 154-159.

Hover, V.C., Walter, L.M., Peacor, D.R., Martini, A.M., 1999. Mg-smectite authigenesis in a marine evaporative environment, salina Ometepec, Baja California. Clay Clay Miner. 47, 252-268.

Kristiansen, S., Hoell, E.E., 2002. The importance of silicon for marine production. Hydrobiologia 484, 21-31.

Loucaides, S., van Cappellen, P., Behrends, T., 2008. Dissolution of biogenic silica from land to ocean: Role of salinity and pH. Limnol. Oceanogr. 53, 1614-1621.

Marius, C., 1985. Mangroves du Senegal et de la Gambie: ecologie, pédologie, géochimie. Mise en valeur et aménagement. Cahiers. Orstom Série Pédologique.

Michalopoulos, P., Aller, R., 1995. Rapid clay mineral formation in Amazon delta sediments: reverse weathering and oceanic elemental cycles. Science 270, 614-617.

Presti, M., Michalopoulos, P., 2008. Estimating the contribution of the authigenic mineral component to the long-term reactive silica accumulation on the western shelf of the Mississippi River Delta. Cont. Shelf Res. 28, 823-838.

Reddy, K.R., DeLaune, R.D., 2008. Biogeochemistry of wetlands, Taylor & Francis Group, Boca Raton, FL.

Ridd, P.V., Stieglitz, T., 2002. Dry Season Salinity Changes in Arid Estuaries Fringed by Mangroves and Saltflats. Estuar. Coastal Shelf Sci. 54, 1039-1049.

Saccone, L., Conley, D. J., Koning, E., Sauer, D., Sommer, M., Daczorek, D., Blecker, S. W., Kelly, E.F., 2007. Assessing the extraction and quantification of amorphous silica in soils of forest and grassland ecosystems. Eur. J. Soil Sci. 58, 1446–1459.

Struyf, E., Conley, D.J., 2009. Silica: an essential nutrient in wetland biogeochemistry. Front. Ecol. Environ. 7, 88-94.

2. ROLE OF REDOX PROCESSES IN PEDOGENESIS OF HYPERSALINE TIDAL FLAT SOILS

Abstract

Hypersaline tidal flats (HTFs) are transitional ecosystems where the ocean, land, and freshwater meet. These places are globally widespread and their soils are an important environmental component controlling chemical reactions in wetland ecosystems. Here we present a pedogenic study of two HTFs on the Brazilian coast (NE and SE) based on the solid-phase geochemistry of Fe and Mn and morphological studies. Broken and irregular topographies and strong expression of redoximorphic concentrations (e.g. mottles, nodules, and pore linings) are present throughout the soil profiles. Although lepidocrocite is the most abundant Fe fraction in the soils (more than 50% of all extractions), deeper horizons show pyrite as the main Fe fraction due to the presence of buried mangrove soils. Actual more oxidizing conditions in these deeper horizons indicate that pyrite is not stable and is undergoing degradation. Fe released in this process is moving upwards and precipitating as Fe oxyhydroxides in more oxidized portions of the soil profiles. Co-precipitation of Mn and ferrihydrite seems to be an important process controlling the geochemistry of Mn in HTF soils. Our data indicate that deeper horizons have been transforming driven mainly by water table oscillation and, consequently, redox processes. These processes allow translocation of Mn^{2+} and Fe^{2+} throughout the soil profiles, followed by oxidation and precipitation of $Mn^{3+/4+}$ and Fe^{3+} oxyhydroxides in preferential sites.

Keywords: Pedogenic processes; Iron; Manganese; Redoximorphic features; Pyrite

2.1. Introduction

Coastal wetlands are globally widespread and can be found in almost all climates (Reddy and DeLaune, 2008). Active biological, chemical, and physical reactions taking place in these complex environments impose great impact on global biogeochemical processes (Frings et al., 2016; Kolditz et al., 2012; Sperlich et al., 2015; Zhang et al., 2013). Two examples of coastal wetland are hypersaline tidal flats (HTF) and mangroves. Although both ecosystems are commonly associated in the estuary, flooding frequency and seawater residence are substantially less expressive at HTFs, leading to different pedogenetic processes and, consequently, formation of soils with different properties (Albuquerque et al., 2014b; Ferreira et al., 2010; Ridd and Stieglitz, 2002).

HTF soils are commonly found in regions where evapotranspiration exceeds precipitation in some months of the year (Albuquerque et al., 2014a; Hadlich and Ucha, 2009). These soils are very common on north, northeast and southeast Brazilian coasts, and in many other countries around the world (Albuquerque et al., 2014a; Ridd and Stieglitz, 2002). Previous studies evidenced that formation of HTFs is a natural process in which mangrove

ecosystems are replaced by a new hypersaline environment (Albuquerque et al., 2014a). This process is driven by an increase in soil salinity due to hydrodynamic alterations in the estuary plain, leading to mangrove dieback followed by formation of hypersaline soils. Pedogenetic relationships between mangrove and HTF soils are noticeable by the presence of deeply buried soils in HTF soils produced by the previous mangrove ecosystem (Albuquerque et al., 2014b; Ucha et al., 2008).

HTF soils are characterized by contrasting morphological, physical, and chemical attributes when compared to mangrove and most well drained and aerated soils (Albuquerque et al., 2014b). Nevertheless, these soils undergo pedogenic processes similar to those of evaporative environments, such as precipitation of calcium carbonate and soluble salts, solonization, salinization, and redox processes (Albuquerque et al., 2014b). Since these environments are under alternating redox conditions, Mn and Fe oxyhydroxides are very important soil components acting as electron acceptors during microbial respiration under suboxic and anoxic conditions (Reddy and DeLaune, 2008). These redox fluctuations lead to the formation of redoximorphic features in the soil profiles, which can be investigated using morphological approaches (Lindbo et al., 2010; Vepraskas, 2001, 2004). Although sulfate-reduction and accumulation of authigenic Fe sulfides are important biogeochemical processes in coastal wetlands (Berner, 1984), these reactions seem not to be relevant in these soils due to more oxidized conditions imparted by the formation of HTFs (Albuquerque et al., 2014b). Investigation of these processes is important to better understand fundamental properties and mechanisms of these soils and how they control the dynamics of elemental cycles in their respective environments.

Few studies have investigated the formation and fundamental properties of HTF soils. We investigated the pedogenesis of two HTFs on the Brazilian coast (NE and SE regions). Our discussion is based on morphological and geochemical studies, with the latter focusing on Fe and Mn sequential extractions to understand forms and distribution of these redox-sensitive elements in HTF soils.

2.2. Environmental settings

Two hypersaline tidal flats (HTFs) were studied along the Brazilian coast (Fig. 1 and 2). One site is in the Acaraú River Basin (northeast region) and is referred as HTF-CE. Regional geology of Acaraú River Basin consists of Pre-Cambrian metamorphic rocks (gneisses, schists

and phyllites). The study area is encompassed by the Barreiras Tablelands, which is composed of Cenozoic sand- and clay-size sediments (Bezerra et al., 2001; Hesp et al., 2009). Rainfall distribution is irregular, with a dry season between July and December. Climate is mild semiarid (Bw, according to Köppen) with an average annual precipitation of about 1,200 mm and evapotranspiration of about 1,700 mm. Tidal regime is semi-diurnal with the amplitude varying between 1.4 and 2.6 m. The area is flooded several days throughout the month with major tidal flooding during spring tides.

The second study site is in the southeast region of Brazil and is included in the Sepetiba-Guaratiba coastal complex (referred as HTF-RJ). Regional geology is composed of Quaternary coastal plains and Pre-Cambrian crystalline basement (granites, gneisses, and migmatites; Borges and Nittrouer, 2015). The estuary, which includes mangroves and HTFs, is a semi-confined environment that is physically protected from the Atlantic Ocean (Muehe et al., 2006). Rainfall distribution is more homogeneous than HTF-CE, with a shorter dry season taking place from June to August. Climate is tropical wet-dry (Aw, according to Köppen), and the average annual precipitation and evapotranspiration are about 1,016 and 1,450 mm, respectively. Both HTFs have an irregular distribution of halophyte plants on the soil surface.

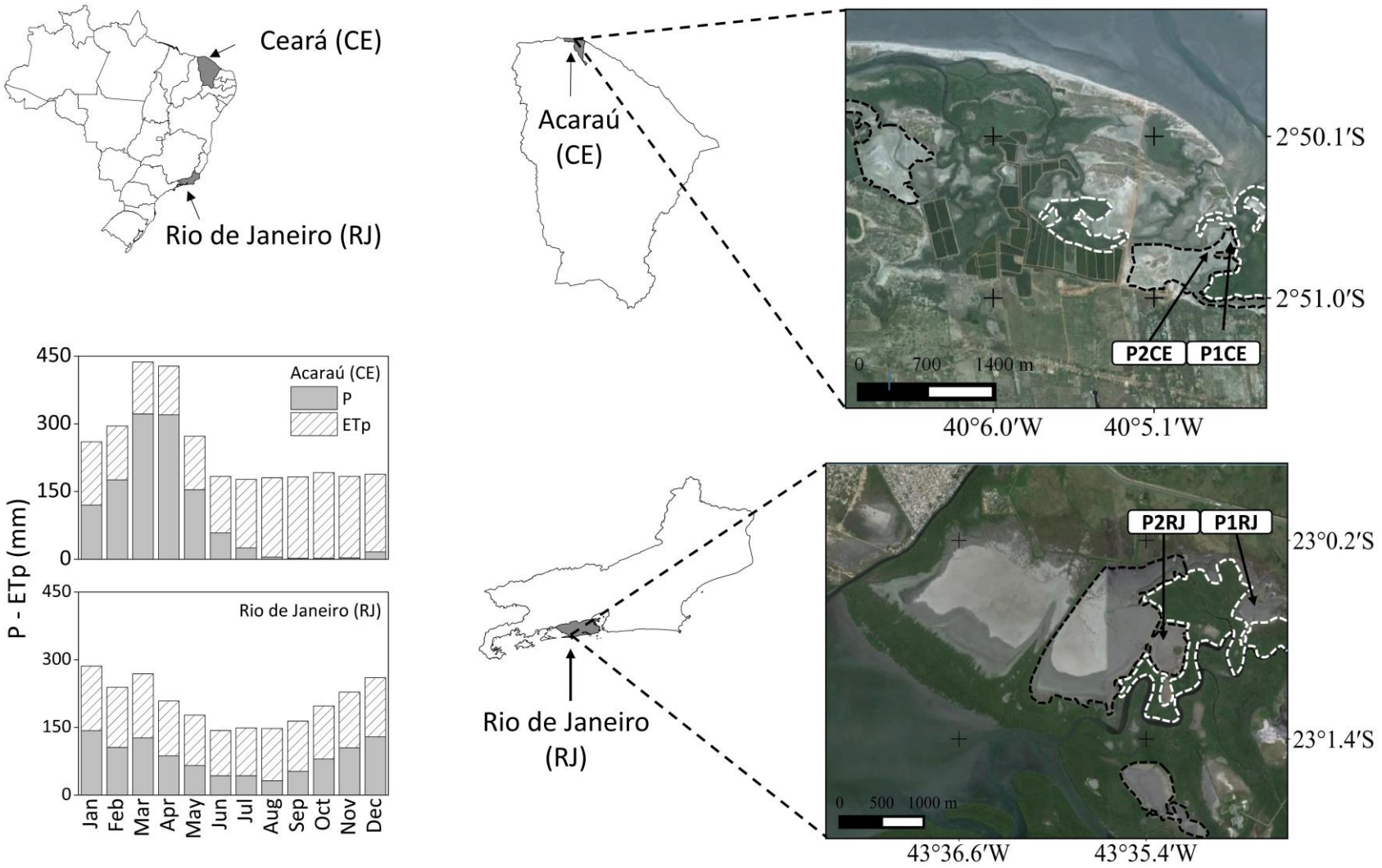

Fig. 1. Location of the study sites and soil profiles. The white and black dashed lines delineate the mangrove forests and HTFs, respectively. Images source: Google™ Earth (2015)

Fig. 2. Study sites during low and high tides

2.3. Materials and methods

Soil morphologic description (Schoeneberger et al., 2002) and soil sampling were carried out during low tide in two soil pits at each site. Soil profiles were labeled as P1CE and P2CE (HTF-CE), and P1RJ and P2RJ (HTF-RJ). Samples were taken by horizon and were maintained at approximately (4 ^{o}C) during transportation to the laboratory, where part of each sample was air dried and another part was stored at low temperature (-5 ^{o}C) to minimize Fe and Mn oxidation.

Soluble salts were removed from the samples using ethanol (70 %) prior to chemical and physical analysis. Particle size distribution was determined by pipette method after removal of organic matter with H_2O_2 30 % v/v (Gee and Or, 2002). Calcium carbonate equivalent (CCE) was determined by titration of the solution with NaOH after dissolution of carbonates with HCl (AOAC, 1970). Total organic carbon (TOC) was determined by wet oxidation (Walkley et al., 1934). Exchangeable K^+ and Na^+ were extracted with H_2SO_4 0.0125 mol L^{-1} + HCl 0.05 mol L^{-1} solution and determined by flame spectroscopy (Digimed DM-62), whereas exchangeable Ca^{2+} and Mg^{2+} were extracted with KCl 1.0 mol L^{-1} solution and determined using atomic absorption spectroscopy (Perkin Elmer 1100B). Potential acidity (H+Al) was measured by titration of the solution with NaOH after extraction with Ca acetate at pH 7.0. Electrical conductivity was measured in a saturation extract (USDA, 2014), and pH and Eh were determined in the field using a glass electrode and an oxidation-reduction potential Pt electrode, respectively. Final readings for Eh measurements were corrected by adding the potential of a calomel reference electrode (244 mV). In order to investigate the presence of sulfidic material, total potential acidity (TPA) was determined by measuring the pH after oxidation of the samples with H_2O_2 30% v/v at pH 5.5 (soil to solution ratio of 1:5, Konsten et al., 1988).

Iron and Mn extractions were carried out using wet samples previously stored at low temperatures. Extractions were performed using a sequential extraction procedure derived from the combination of methods proposed by Fortin et al. (1993), Huerta-Díaz and Morse (1990), and Tessier et al. (1979). This methodology has been used widely for wetland soils (see Ferreira et al., 2010; Nóbrega et al., 2014; Otero et al., 2009 for more details) and allows differentiation of six operationally-defined fractions: exchangeable Fe and Mn (F1); Fe and Mn associated with carbonates (F2); ferrihydrite and Mn associated with this extraction (F3); lepidocrocite and Mn associated with this extraction (F4); crystalline Fe oxyhydroxides and

Mn associated with this extraction (F5); Fe and Mn associated with pyrite (F6). Degree of iron pyritization (DOP) was calculated as follows:

$$DOP\ (\%) = \left(\frac{Fe_{pyrite}}{Fe_{reactive} + Fe_{pyrite}} \right) \times 100$$

This equation determines the percentage of reactive Fe incorporated in the pyritic fraction (Berner, 1970). In this study, reactive Fe was defined as $\sum(F_1 \rightarrow F_5)$.

Values measured for F6 in the Mn extractions were very low (mean value for all samples: 0.07 ± 0.1 mmol kg^{-1}) and thus were not considered in this study. Iron and Mn concentrations in the extracts were determined by atomic absorption spectroscopy (Perkin Elmer AAnalyst 400).

Redox concentration samples from 12 horizons were selected for diffuse reflectance spectroscopy (DRS) to identify Fe oxyhydroxides present in order to support the Fe sequential extractions. DRS spectra were obtained from freeze-dried and ground powders. Spectra were taken from 350 to 840 nm at 1 nm increments with a 110 mm integrating sphere using a Varian Cary 5 Spectrophotometer. Reflectance function was transformed into remission function applying the Kubelka Munk theory, and second derivative was calculated using a cubic spline fitting procedure (Malengreau et al., 1996).

2.4. Results

2.4.1. Characterization of the soil profiles

Morphological data are shown in Table 1 and the soil profiles can be visualized in Fig. 3. P1CE and P2CE profiles were classified as Tidalic Episalic Endogleyic Fluvisol (Thapto-Thionic, Sodic), whereas P1RJ and P2RJ profiles were classified as Tidalic Episalic Endogleyic Fluvisol (Thapto-Thionic, Sodic, Epiclayic) (IUSS Working Group WRB, 2006). All the studied soils were classified as Gleissolos Tiomórficos Órticos Sódicos based on the Brazilian Soil Classification System (Embrapa, 2013).

Topographies of the horizon boundaries vary widely among and within the soil profiles. Broken topographies (tongues) appear above C4 (P1CE) and C3 (P2CE) horizons, which are related to the buried mangrove soils. Wavy and irregular boundaries were found in the C2 (P1RJ) and C1 (P2RJ) horizons. As in the HTF-CE profiles, these boundaries appear above the

buried mangrove soils. The existence of buried mangrove soils is discussed in more detail below.

All profiles have yellowish, reddish or brownish hues (2.5Y, 5Y, and 10YR) in the uppermost horizons, with strong expression of redoximorphic concentrations (2.5YR, 5YR, 7.5YR, 10YR hues, with high chroma). Reduced matrix (5B, 10B, 5GB, 10GB hues) occurs in the buried mangrove soils (Table 1 and Fig. 3). Most of horizons are structureless (massive), with only surface horizons displaying granular structure (all soil profiles) and platy structure with shiny peds (only in the HTF-RJ soil profiles). Particle size distribution is erratic in the profiles at HTF-CE (Fig. 4), with clay content varying from 12 to 55 %, and sand from 21 to 70 %. In contrast, sand content is less than 3 % and clay is more than 55 % at HTF-RJ, with a clayey texture in all horizons. High base cation content and low values of H^{+}+Al^{3+} lead to base saturation above 70% in most of the soil horizons. Overall, the soils display high sodium saturation (ESP), with mean values of 11 % (P1CE), 32 % (P2CE), 46 % (P1RJ), and 31 % (P2RJ).

pH values are higher in the surface horizons and decrease with increasing depth (Fig. 5). pH values range from 7.7 to 8.3 in the HTF-CE soils, and 6.8 to 7.1 in the HTF-RJ soils. TPA values less than 2.5 (Fig. 5) indicate presence of sulfidic materials in the C3 and C4 horizons of P2CE, C3 horizon of P1RJ, and C3 horizon of P2RJ (IUSS Working Group WRB, 2006). Based on Eh values (Fig. 5), C4 horizon of P1CE, C3 and C4 horizons of P2CE, C3 horizons of P1RJ, and C3 of P2RJ are under suboxic conditions (approximately 100 to 400 mV), while the other horizons are under oxic condition (> 400 mV). Soil profiles display low TOC content in the uppermost horizons (less than 1.0 %), increasing with depth to up 4.4 % (Fig. 6) due to the presence of buried mangrove soils (Albuquerque et al., 2014b; Ucha et al., 2008). Formation of calcium carbonate is more extensive at HTF-CE, with concentrations of approximately 109 g kg^{-1} in the surface horizons, decreasing to less than 30 g kg^{-1} in the deeper horizons. The C horizon of P1CE profile displays high CCE likely due to the presence of broken and shattered shell fragments in this soil horizon. At HTF-RJ, CCE values are approximately 27 g kg^{-1} in the surface horizons (Table 2). All soil profiles have high electrical conductivity in all horizons, with a mean for all horizons higher than 100 dS m^{-1}, which is greater than the EC of seawater (≈ 50 dS m^{-1}).

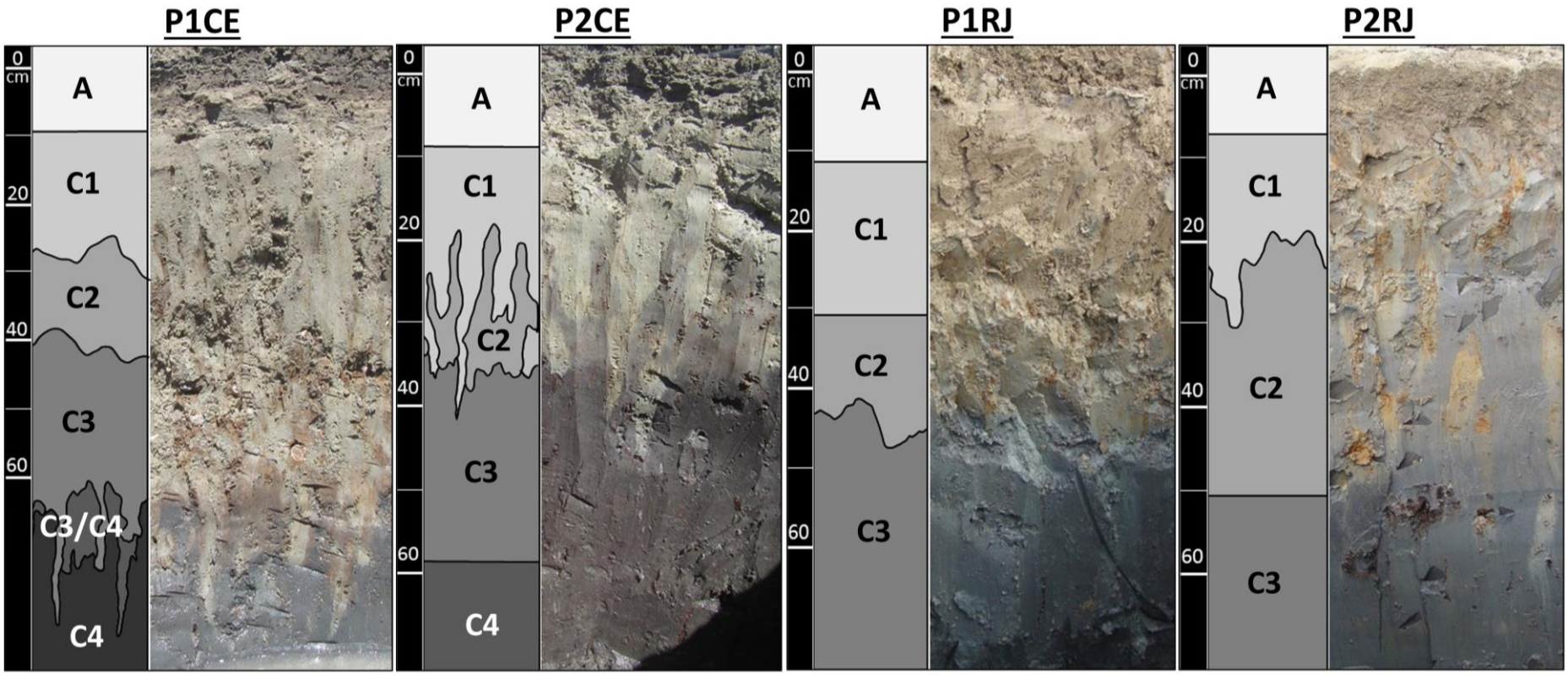

Fig. 3. Morphology of the soil profiles

Table 1. Morphological attributes of the soil profiles. Quantity/contrast: common (c), many (m), prominent (p). Structure: granular (gr), massive (m), platy (pl). Boundary: gradual (g), clear (c), diffuse (d), abrupt (a), smooth (s), wavy (w), irregular (i), broken (b). Shiny peds: present (+), absent (-)

Horizon/Depth (cm)	Matrix colour	Redox concentration/mottles		Structure	Boundary	Shiny peds
		Colour	Quantity/Contrast			
P1CE - Tidalic Episalic Endogleyic Fluvisol (Thapto-Thionic, Sodic)						
A (0-10)	5Y 5/2	-	-	gr, m	g,s	-
C1 (10-29)	5Y 6/2	-	-	m	g,w	-
C2 (29-51)	5Y 6/2	5YR 3/4, 10YR 6/8	c/p	m	g,w	-
C3 (51-71)	5Y 6/4, 5Y6/2	5YR 3/4	m/p	m	c,i	-
C3/C4 (71-85)	5Y 6/4, 10YR 4/4, 2.5Y 5/4, 5B 4/1	-	-	m	c,b	-
C4 (85-104+)	5B 4/1	-	-	m	-	-
P2CE - Tidalic Episalic Endogleyic Fluvisol (Thapto-Thionic, Sodic)						
A (0-9)	10YR 4/1		-	gr, m	g,s	-
C1 (9-26)	5Y 6/2	10YR 4/6	c/p	m	c,i	-
C2 (26-38)	10G 4/1	5YR 3/4, 7.5 YR 4/6	c/p	m	c,b	-
C3 (38-66)	10B 3/1	-	-	m	d,s	-
C4 (66-90+)	10B 3/1	-	-	m	-	-
P1RJ - Tidalic Episalic Endogleyic Fluvisol (Thapto-Thionic, Sodic, Epiclayic)						
A (0-13)	10YR 3/2	-	-	gr, pl	g,s	+
C1 (13-30)	2.5Y 6/2	7.5YR 3/3	m/p	m	g,s	-
C2 (30-56)	5Y 6/2	2.5YR 3/2, 7.5YR 4/6	m/p	m	a,w	-
C3 (56-120+)	5B 3/1	-	-	m	-	-
P2RJ - Tidalic Episalic Endogleyic Fluvisol (Thapto-Thionic, Sodic, Epiclayic)						
A (0-11)	10YR 4/2	2.5YR 3/4, 7.5YR 4/6	c/p	gr,pl	g,s	+
C1 (11-30)	2.5Y 5/1, 10BG 4/1	2.5YR 3/4, 7.5YR 4/6	m/p	m	g,i	-
C2 (30-51)	5GB 4/1	7.5YR 5/6, 2.5Y 5/1	m/p	m	d,s	-
C3 (51-105+)	10GB 3/1	-	-	m	-	-

Table 2. Chemical attributes of the soil profiles

Horizon/depth	Na^+	K^+	Mg^{2+}	Ca^{2+}	H^+Al^{3+}	CEC	Base sat.	ESP	CCE	EC
	---------- $mmol_c\ kg^{-1}$ ----------						-------- % ---------		$g\ kg^{-1}$	$dS\ m^{-1}$
P1CE - Tidalic Episalic Endogleyic Fluvisol (Thapto-Thionic, Sodic)										
A (0-10)	2.9	2.0	6.2	23.1	0.0	34.1	100.0	8.4	107.5	105.3
C1 (10-29)	2.9	2.5	4.7	21.5	1.6	33.2	95.2	8.7	77.5	102.3
C2 (29-51)	6.2	7.9	7.6	29.9	5.0	56.6	91.2	11.0	40.4	104.6
C3 (51-71)	3.3	5.9	5.2	25.6	3.6	43.7	91.8	7.7	35.2	111.1
C3/C4 (71-85)	7.2	9.6	9.0	35.8	9.2	70.8	87.0	10.1	27.3	134.4
C4 (85-104+)	29.7	16.6	18.1	72.3	9.0	145.7	93.8	20.4	107.5	126.5
P2CE - Tidalic Episalic Endogleyic Fluvisol (Thapto-Thionic, Sodic)										
A (0-9)	23.9	8.4	13.2	23.1	0.0	68.6	100.0	34.9	110.5	84.2
C1 (9-26)	11.5	7.6	8.1	25.5	1.4	54.1	97.4	21.2	72.4	95.0
C2 (26-38)	108.6	26.4	21.7	29.4	13.0	199.2	93.5	54.5	22.9	134.7
C3 (38-66)	62.7	19.7	23.2	29.5	48.4	183.5	73.6	34.2	8.2	157.3
C4 (66-90+)	23.4	10.1	12.9	23.2	75.0	144.6	48.1	16.2	5.7	156.3
P1RJ - Tidalic Episalic Endogleyic Fluvisol (Thapto-Thionic, Sodic, Epiclayic)										
A (0-13)	63.9	74.9	21.4	9.2	10.0	179.4	94.4	35.7	30.9	106.4
C1 (13-30)	78.6	57.5	22.8	9.2	23.4	191.5	87.8	41.0	20.0	74.6
C2 (30-56)	157.1	46.6	26.1	11.8	22.2	263.8	91.6	59.6	22.3	89.0
C3 (56-120+)	107.8	51.2	33.3	14.6	18.6	225.4	91.8	47.8	20.6	118.5
P2RJ - Tidalic Episalic Endogleyic Fluvisol (Thapto-Thionic, Sodic, Epiclayic)										
A (0-11)	31.1	64.9	17.0	7.1	9.0	129.1	93.0	24.1	23.1	102.6
C1 (11-30)	53.0	33.8	19.4	7.8	40.6	154.6	73.7	34.3	17.3	95.5
C2 (30-51)	68.5	33.8	23.2	10.0	54.2	189.7	71.4	36.1	21.7	130.5
C3 (51-105+)	68.5	49.3	31.9	23.3	55.8	228.8	75.6	30.0	3.8	135.0

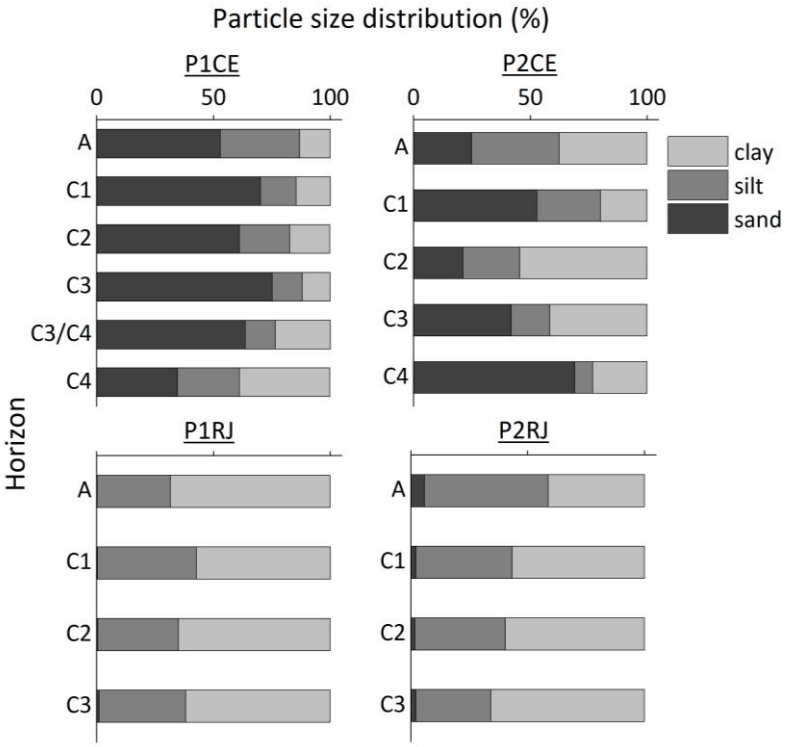

Fig. 4. Particle size distribution of the soil profiles

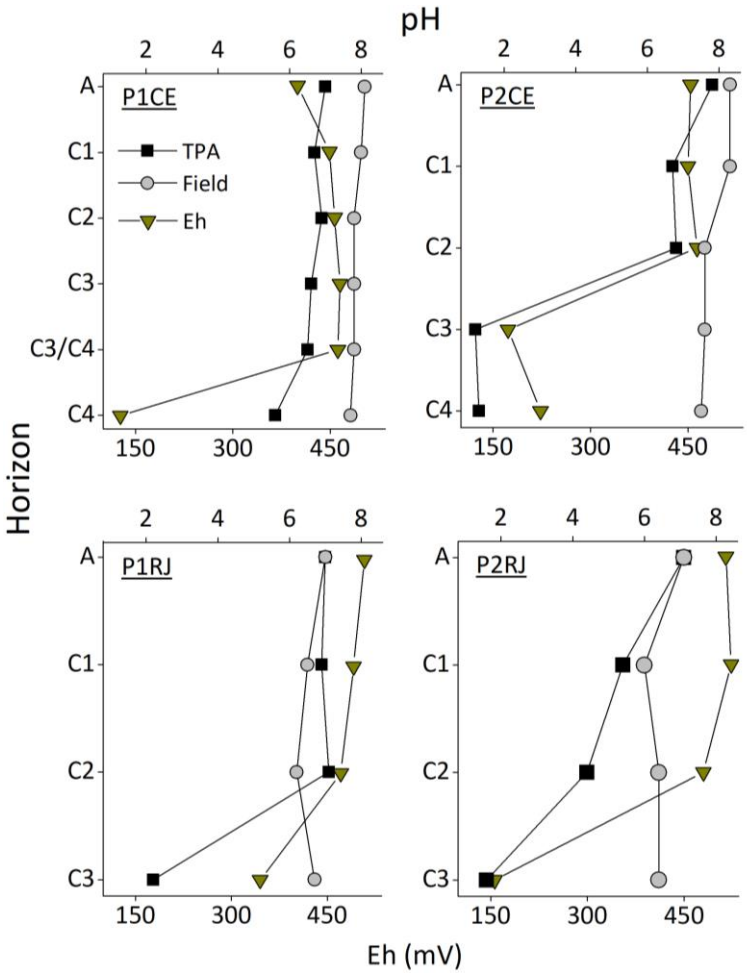

Fig. 5. pH values measured in the field (field), total potential acidity (TPA), and redox potential (Eh) of the soil profiles

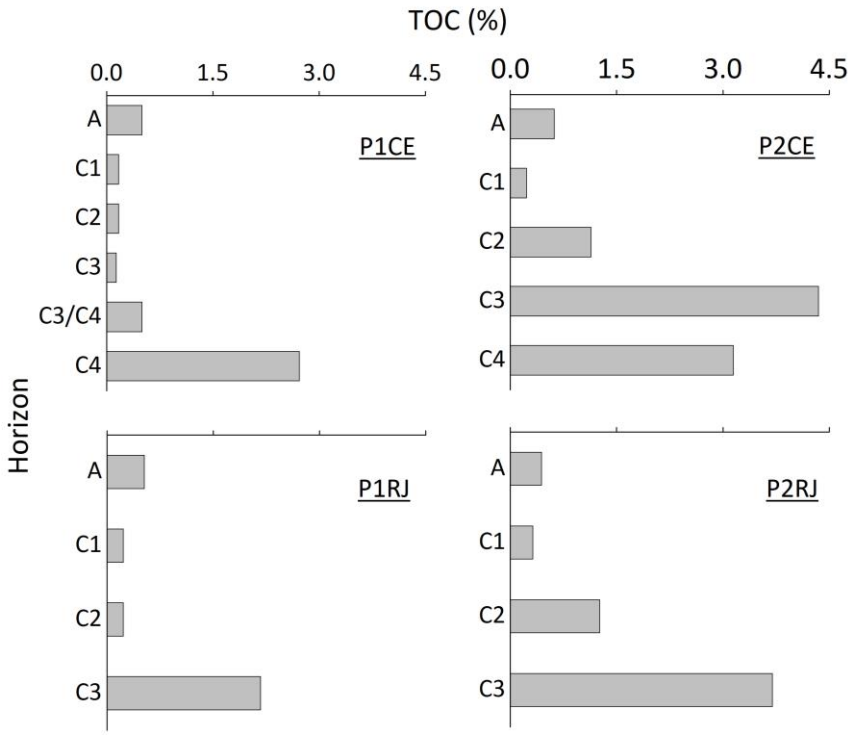

Fig. 6. Total organic carbon (TOC) of the soil profiles

2.4.2. Solid-phase distribution of Fe

Iron concentrations of exchangeable and carbonate fractions are very low in all soil horizons (mean values of all horizons: 1.0 ± 0.2 mmol kg^{-1} for exchangeable Fe and 0.5 ± 0.2 mmol kg^{-1} for Fe-carbonate), generally representing less than 3 % of the extractions (Fig. 7). Mean concentrations of lepidocrocite for all horizons of each site are 31.7 ± 10.9 mmol kg^{-1} at HTF-CE and 34.9 ± 15.4 mmol kg^{-1} at HTF-RJ, comprising more than 50% of all extractions. In general, lepidocrocite concentration increases with depth and decreases again in the buried mangrove soils. Highest concentrations of lepidocrocite occur in the C3/C4 (P1CE), C2 (P2CE), C2 (P1RJ), and C2 (P2RJ) horizons, where the redoximorphic features are more evident. Higher pyrite concentrations are found in the deeper horizons (buried mangrove soils), as supported by the higher values of the degree of pyritization (DOP). These values range from less than 2 % in the uppermost horizons to approximately 57% in P1CE and P2CE, 30% in P1RJ, and 73% in P2RJ. Concentrations of ferrihydrite are highest in the uppermost horizons, with mean concentrations for the surface horizons of 21.1 ± 3.8 mmol kg^{-1} (HTF-CE) and 7.5 ± 0.3 mmol kg^{-1} (HTF-RJ). Concentrations of Fe-crystalline display a more homogenous distribution throughout the profiles and vary from approximately 3.0 to 9.0 mmol kg^{-1} in the P1CE, P2CE and P1RJ soil profiles. The C1 horizon of the P2RJ profile has an anomalous Fe-crystalline concentration of 138.0 mmol kg^{-1}. This horizon has a higher number of nodules, which likely

explains the high concentration of crystalline Fe oxyhydroxides. The other horizons of the P2RJ profile have concentrations of Fe-crystalline between 6.0 and 12.0 mmol kg^{-1}.

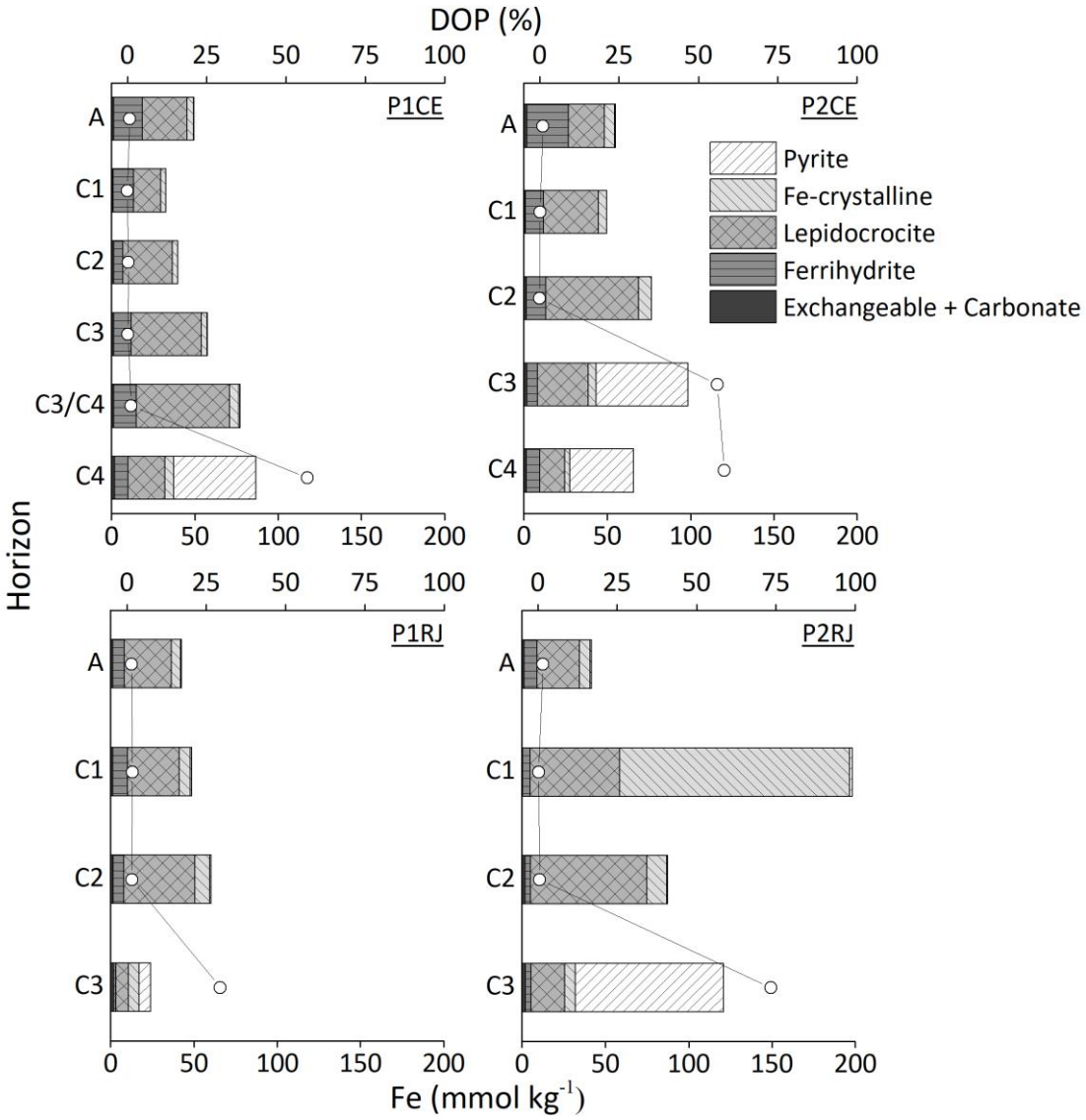

Fig. 7. Fe sequential extractions and degree of pyritization (DOP) of the soil profiles

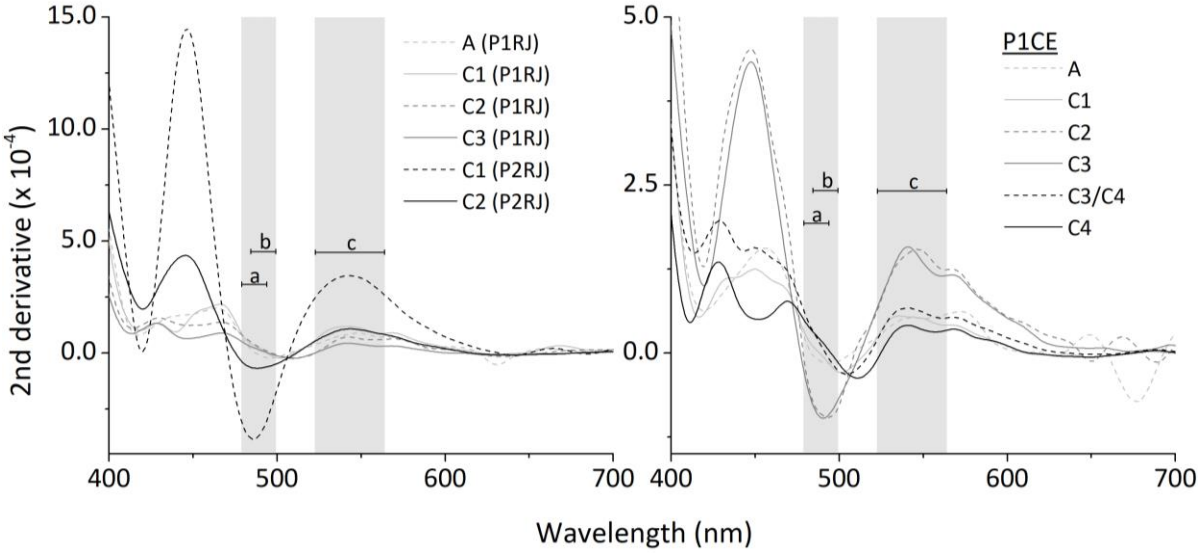

Fig. 8. Second-derivative spectra of the redox concentrations sampled from the profiles P1CE (right), P1RJ and P2RJ (left). Range of crystal field band positions (ETP) for lepidocrocite and goethite (a), ferrihydrite (b), and hematite (c) (Scheinost et al. 1998)

The DRS data corroborate the Fe sequential extraction data (Fig. 8). The most intense absorption bands (electronic transition of pair - ETP band) are associated with the presence of lepidocrocite in the samples. This band for lepidocrocite is between 485 and 490 nm (Scheinost et al., 1998), the same range detected for the A, C1, C2 and C3 horizons (P1CE). Although these bands do not allow a precise distinction between goethite and lepidocrocite, the sequential extractions indicate the presence of lepidocrocite in the samples. Goethite is likely the dominant crystalline Fe mineral in these soils (Schwertmann and Taylor, 1989), which contributes to the absorption band shown in the DRS spectra (around 488 nm, Fig. 8). Furthermore, the absorption band indicative of hematite was not evident in either spectra. Samples from P1RJ and P2RJ profiles also have absorption bands (ETP) indicative of lepidocrocite.

2.4.3. Solid-phase distribution of Mn

Results of Mn sequential extractions are shown in Fig. 9. Unlike the Fe pool, highest concentrations of Mn were in the exchangeable fraction in all horizons at HTF-CE (2.5 ± 0.8 mmol kg^{-1}). In general, this fraction increases with depth and comprises 63 % of the extracted Mn. Concentration of Mn-F3 (0.6 ± 0.5 mmol kg^{-1}) and Mn-F4 (0.4 ± 0.3 mmol kg^{-1}) are much smaller when compared to exchangeable Mn. By contrast, exchangeable Mn is not the main fraction at HTF-RJ. Mn-F3 (5.7 ± 5.1 mmol kg^{-1}) and Mn-F4 (5.8 ± 4.3 mmol kg^{-1}) make up more than 90 % of total Mn extracted in the HTF-RJ soils. These fractions are present in

higher concentrations in the uppermost horizons and decrease substantially with depth. For example, concentration of Mn-F3 drops from 18.9 mmol kg^{-1} in the C1 horizon to less than 0.1 mmol kg^{-1} in C3 (P1RJ), and 9.0 mmol kg^{-1} in A to less than 0.1 mmol kg^{-1} in C3 (P2RJ). The amount of Mn associated with pyrite is negligible in all soil profiles, even in the buried mangrove soils, with a mean value of 0.07 ± 0.1 mmol kg^{-1}. This value comprises less than 1.0 % of all extractions.

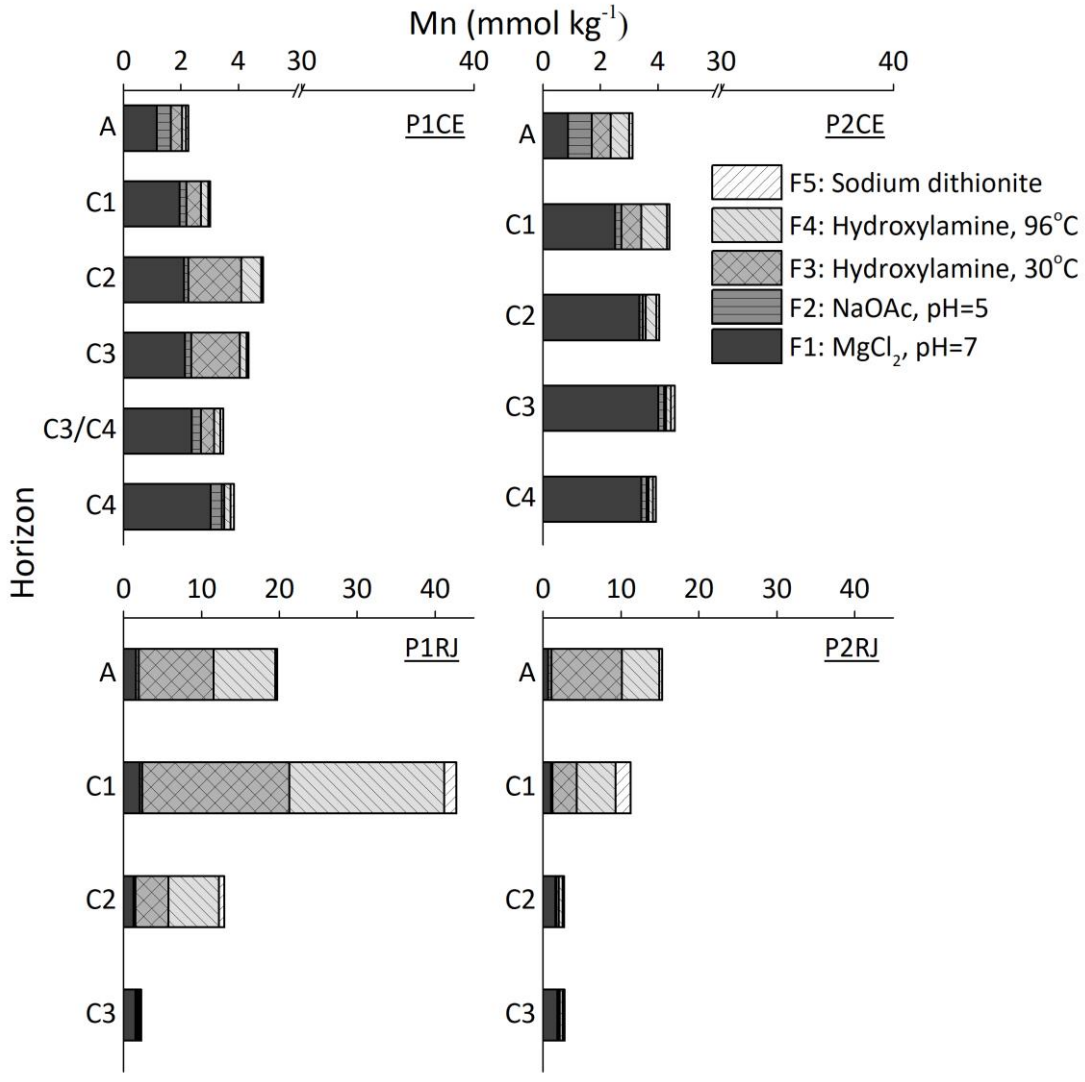

Fig. 9. Mn sequential extractions of the soil profiles

2.5. Discussion

2.5.1. Pedogenic processes

Traditionally, soils from saline and arid sites are classified as saline (EC>4 dS m^{-1}, ESP<15 %), saline-sodic (EC>4 dS m^{-1}, ESP>15 %, pH<8.5), or alkaline soils (EC<4 dS m^{-1}, ESP>15 %, pH>8.5) (Richards, 1954). According to this classification, HTF soils correspond to saline

(P1CE) and saline-sodic soils (P2CE, P1RJ, and P2RJ). P1CE profile showed ESP values lower than 15 % in most of the profile and was therefore classified as saline. This profile is positioned at a higher elevation, in a convex portion of the microrelief, and has a higher sand content when compared to P2CE. Water is more rapidly drained from the soil surface and likely transported laterally away from the profile. Since Na^{+} is more susceptible to leaching (more soluble) and the exchangeable divalent cations (Mg^{2+} and Ca^{2+}) have more binding affinity to clays (Rytwo et al., 1996), it appears that Na^{+} has been leached and replaced by Ca^{2+} and Mg^{2+} on the particle surfaces in the P1CE profile. As can be seen in Table 2, exchangeable Mg^{2+} and Ca^{2+} occupy more than 70 % of the CEC throughout the P1CE profile.

Salinization is easily recognizable by EC values in all horizons and accumulation of salts on the soil surface (van Breemen and Buurman, 2002). In general, the diagnostic criterion to define a salic horizon by Soil Taxonomy (Soil Survey Staff, 2014) and hypersalic horizon by World Reference Base for Soil Resources (IUSS Working Group WRB, 2006) is a horizon that has an EC of 30 dS m^{-1} or higher. HTF soils display EC values between 75 and 157 dS m^{-1}, which imply that HTF soils are strongly affected by salinization. This is explained by the flat relief, higher soil elevation in the estuarine plain when compared to mangroves, constant input of seawater, and high evapotranspiration rates associated with low soil permeability. These conditions enable seawater to remains in the soil profiles and on the soil surface after tide recedes, which favor concentration of soluble salts in the interstitial water by evapotranspiration.

High Na^{+} concentrations on cation exchange sites in the P2CE, P1RJ, and P1RJ soil profiles indicate that solonization process is taking place in these soils. Although this process often leads to an increase in pH values over 8.5 and has been reported by Albuquerque et al. (2014b) in these ecosystems, no pH values higher than 8.3 were measured in this study. It seems that the formation of sodium carbonate, which leads an increase in pH over 8.5 (van Breemen and Buurman, 2002), does not play a significant role in the HTF soils due to the constant supply of exchangeable cations other than Na^{+} to the soil profiles.

There is a strong correlation between the clay content and CEC in both sites ($r=0.82$, $n=19$, $p<0.05$), and no such correlation exists between TOC and CEC, which means that the clay fraction in these soils exerts a strong control on the cation exchange in these soils. A high correlation between ESP and clay content ($r=0.83$, $n=19$, $p<0.01$) demonstrates that higher clay content and seawater-clay mineral exchange equilibria reactions lead to a higher

proportion of Na^+ on the exchange sites in HTF soils (Sayles and Mangelsdorf, 1977), which likely explains the high ESP values in the HTF-RJ soils (clay content of approximately 60 %). Farrell and Brooks (1971) showed that increase in water salinity favors adsorption of Na^+ on exchangeable sites of clays at expense of divalent cations (mainly Mg^{2+}). Harron et al. (1983) also showed Na^+ is adsorbed more strongly relative to Ca^{2+} in presence of higher clay content in sodic soils (e.g. P2CE profile).

Accumulation of secondary calcium carbonate (calcification process) is an active process at HTFs. Evaporative concentration of interstitial water leads to carbonate precipitation, which is evidenced by CCE values. This pedogenic process is likely an important factor controlling the geochemistry of Mn in HTF soils, mainly in surface horizons at HTF-CE (more than 20 % of Mn extracted is associated with carbonates). Previous studies have shown that relatively high concentrations of Mn associated with carbonates control the solubility of Mn^{2+} in environments driven by either $CaCO_3$ adsorption or coprecipitation (Böttcher, 1998; Mucci, 1988; Otero et al., 2003).

Low TPA and high DOP values indicate presence of sulfidic material in the deeper horizons. In general, pyrite formation is favored in environments under anaerobic conditions where metasulfides are produced by bacteria using organic compounds as reducing agents and energy sources (Berner, 1984). This implies that organic matter can be a limiting factor for pyrite precipitation. Strong correlations between TPA and TOC, TPA and Eh, Eh and TOC, and DOP and TOC (Fig. 10) indicate that sulfidic material is mostly present deeper in the soil profiles, where the buried mangrove soils are present (TOC contents are higher and Eh values are lower). Nevertheless, pyrite formation is not favorable under present soil conditions (high Eh and pH values). Plotting soil Eh and pH values in the stability diagram for Fe-S-O-H system shows that pyrite is likely undergoing oxidation in HTF soils (Fig. 11). Therefore, our data suggest that pyrite is inherited from the buried mangrove soils and its occurrence deeper in the soil profiles is a consequence of a “paleo-sulfidization process”. Thus, pyrite formation is not an active process in HTF soils. The morphology of pyrite has been studied by Albuquerque et al. (2014b) in the same estuary (HTF-CE). They suggest that pyrite has undergone some morphological alteration due to more oxidizing conditions when compared to mangrove soils, which corresponds with our findings. Therefore, the oxidation of sulfide-bearing minerals seems to be an active process in HTF soils, and Fe released gradually to the soil solution may be precipitating as Fe oxyhydroxides in more oxidized zones of the soil profiles (Fitzpatrick et

al., 1996) and on the surfaces of pre-existing solids as coatings (Bonnissel-Gissinger et al., 1998). The latter is expected to slow down oxidation of pyrite in the deeper horizons, since Fe oxyhydroxides coatings can block oxidant transport from the solution to the pyrite surface, reducing the rate of pyrite oxidation (Huminicki and Rimstidt, 2009). This process helps to explain the presence of sulfidic material in HTF soils (Albuquerque et al., 2014b).

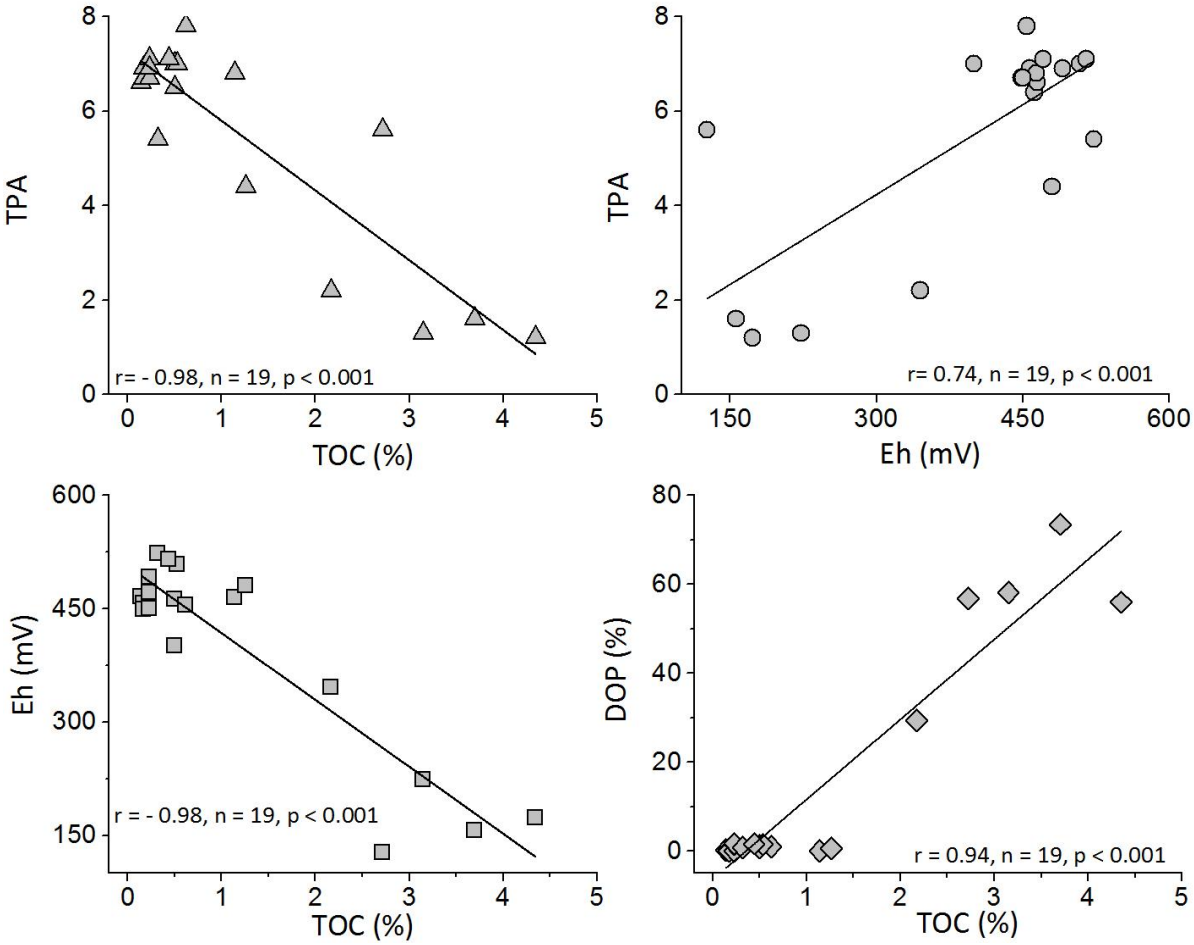

Fig. 10. Correlation between TOC and TPA, Eh and TPA, TOC and EH, and TOC and DOP

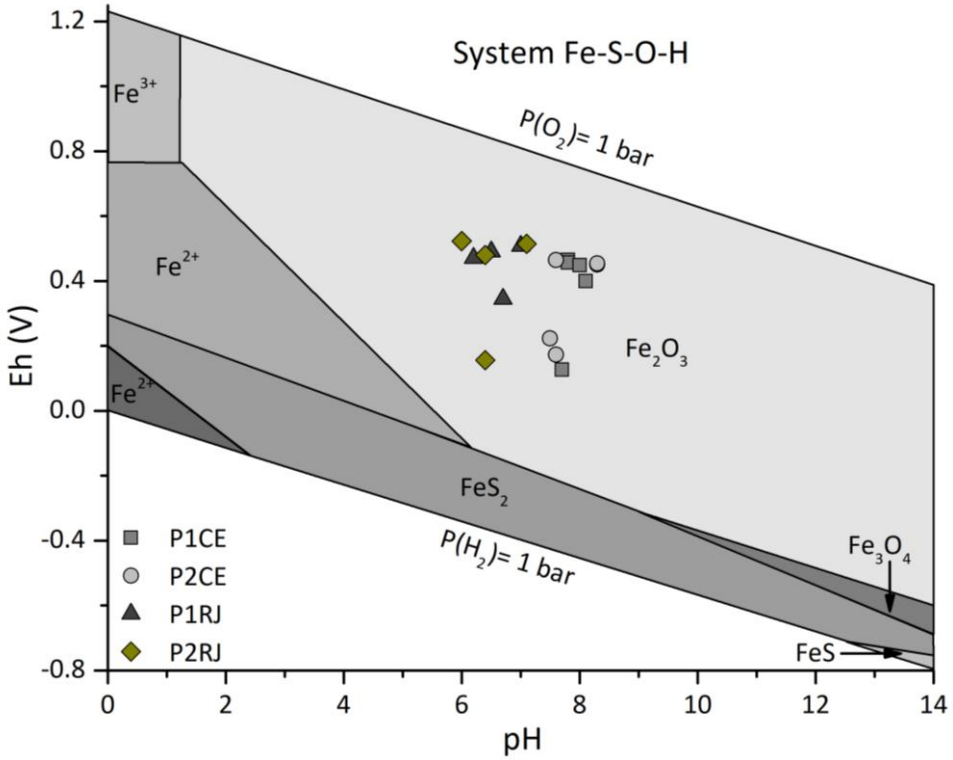

Fig. 11. Eh-pH diagram for the system Fe-S-O-H (adapted from Brookins, 1987a)

2.5.2. Transformation of subsurface horizons

Morphological and chemical data presented in this study suggest that subsurface horizons of both HTF soils are undergoing transformations driven mainly by redox processes. Predominance of redox concentrations and variegated color in the intermediate portion of the profiles is due to oxidation-reduction cycles caused by oscillation of the water table in these soil sections. It was noticed during fieldwork that the deeper horizons are continually saturated by water even during dry season and low tides, a condition that does not favor the occurrence of redoximorphic features (Schwertmann and Fanning, 1976). Transformations can be better understood when a comparison is made between the deeper horizons (buried mangrove soils) and the overlying horizons at each site. These can be seen in P1CE and P2RJ profiles (Fig. 12). Fig. 12a (arrows) shows the occurrence of Fe concentrations following the boundary of the tongues in the C3 and C3/C4 horizons, indicating Fe is precipitating in some preferential sites. Reduction of ferric iron to iron is favored in deeper horizons (buried soils) where TOC is higher and Eh is lower, which enable Fe^{2+} to move through the soil and precipitate in more oxidized sites of the soil profiles. Similar redox concentrations occur in the P2RJ profile (Fig. 12b and c). It can be seen that Mn ferrous and/or Fe concentrations occur as pore linings and nodules in the reduced matrix of the C2 horizon, which indicates an

accumulation of Fe and Mn along root channels likely left by dead roots from previous mangrove trees (more oxidized zones). Tubular and vertical shapes of Fe and Mn concentration (Fig. 12b, c and d) also suggest formation of pedofeatures influenced by roots (Sundby et al., 1998). Iron and Mn tubular concretions in salt marshes originate from oxidation of metals at the root surface, increasing radially outward from the root channel as Fe precipitates (Sundby et al., 1998). This process likely has taken place in the P2RJ soil profile.

Formation of redox concentrations at the boundary of the tongues in the C3 and C3/C4 horizons (P1CE) and formation of nodules and pore linings in the C2 horizon (P2RJ) are favored by soil endosaturation and water table oscillation throughout the soil profiles. These processes allow Fe^{2+} to diffuse through and within the soil solution. As water table goes down, pore channels are aerated and the higher redox conditions lead to the precipitation of Fe oxyhydroxides in preferential sites (e.g. tongues and root channels), resulting in redox concentrations. More oxidizing conditions in the tongues are confirmed by measured Eh values (> 400 mV). Furthermore, the soil matrix displaying chroma of 2 or less and values of 4 or more, and presence of redox concentrations with a diffuse boundary indicate that redox features are still forming in the soils (Vepraskas, 2001). These observations support our interpretation that the water table oscillates and, consequently, allows the Fe^{2+} to move through the profile followed by precipitation as Fe oxyhydroxides in preferential sites along the root channels and on the tongues boundaries. These processes are supported by Fe and Mn extractions and are discussed in more details throughout the text below.

Other observations are pertinent to the transformation of HTF soils. Some portions of the C3/C4 horizon (P1CE) display a color of 5B 4/1, which is the same reduced color of the C4 horizon. Increase in TOC values with depth (0.1, 0.5, and 2.7% throughout C3→C3/C4→C4, respectively) indicates that the C3/C4 horizon still preserves characteristics of the previous mangrove soil. On the other hand, the oxic conditions in C3/C4 (462 mV) and predominance of the lepidocrocite and ferrihydrite in the Fe pool (90 % of the Fe extraction) indicate periods of recent oxidation in the deeper horizons.

The P2CE profile also shows evidence of transformations in the intermediate portion of the soil profile, especially in the C2 horizon. As in P1CE, there is a depth-dependent increase in TOC (0.2, 1.1 and 4.3 % througout C1→C2→C3, respectively) and presence of irregular and broken boundaries (tongues) througout the soil profile. In addition, C2 horizon maintains a

reduced color (10G 4/1) due to gleization processes, with predominance of yellowish and orange mottles due to a higher lepidocrocite concentration when compared to other horizons. These features indicate C2 horizon still maintains characteristics of the buried mangrove soil. On the other hand, Eh and TPA values and presence of yellowish redox concentrations indicate that oxidation and transformation of the C2 horizon is similar to that of C3/C4 (P1CE).

In P1RJ, the C1 and C2 horizons have many redox concentrations and nodules, the latter occupying approximately 1-2 % of the horizon. Nodules (2-5 cm) in these horizons are possibly related to precipitation of Fe and Mn in air-filled pores or channels due to oscillation of the water table in this section of the profile (D'Amore et al., 2004). Although there is just subtle morphological evidence of oxidation in the C3 horizon, the presence of redox concentration in the C2 horizon, wavy boundaries (C2→C3), and high Eh values in C3 (345 mV), suggest that some transformations can be occurring deeper in the soil profile.

Based on the sequential extractions, lepidocrocite is the predominant Fe mineral in the soil profiles. This supports seasonal alternation of reducing and oxidizing conditions in both sites. These conditions favor formation of Fe^{2+}, which moves into oxygenated zones within the soil and precipitates as lepidocrocite (Cornell and Schwertmann, 2003). Horizons with the highest concentrations of lepidocrocite are C3/C4 (P1CE), C2 (P2CE), C2 (P1RJ), and C2 (P2RJ). These horizons, situated right above the buried mangrove soils, display evidence of transformation driven by redox processes. This result supports the idea that dissolved Mn and Fe are migrating out the reduced matrixes and precipitating as oxyhydroxides in more oxidized sites in the uppermost horizons. This tendency is also visualized in Fig. 13. Considering the sum of the fractions strongly affected by redox processes (F3+F4+F5), higher concentrations of these fractions (F3+F4+F5) are present in the intermediary horizons of the soil profiles (where the water table oscillates), and lower concentrations are found in the deeper horizons (buried mangroves soils). This distribution of extracted Fe and Mn (F3+F4+F5) can be explained by the movement of Fe and Mn through the soil profiles, which supports the discussion previously reported.

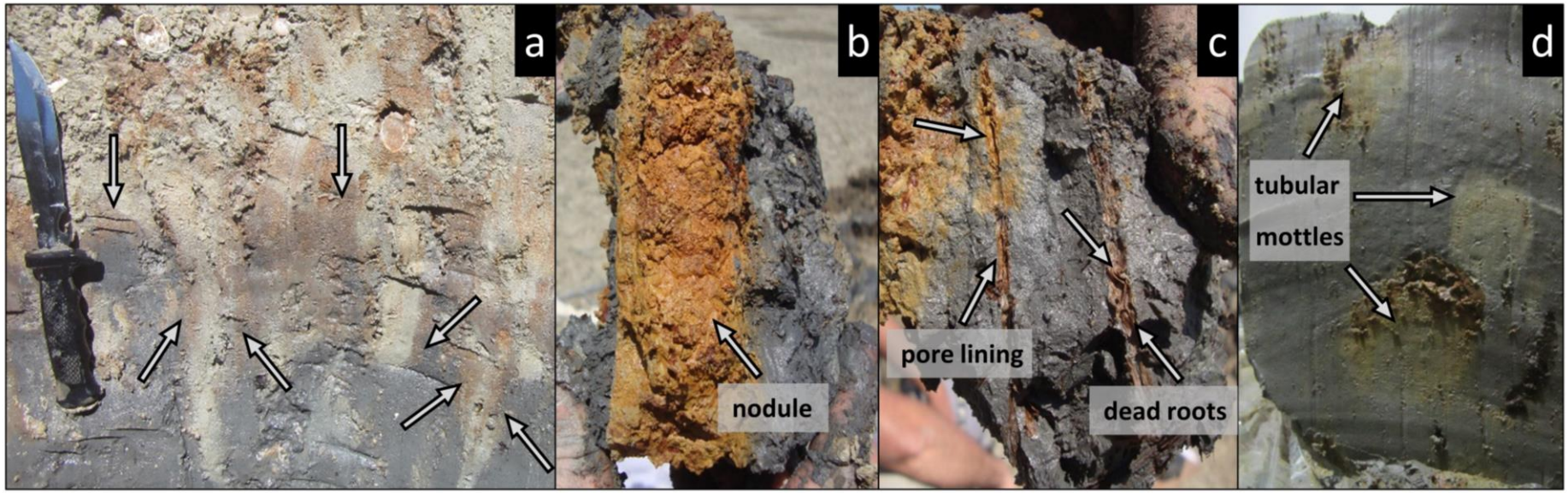

Fig. 12. Redoximorphic features in the P1CE and P2RJ profiles. a) Fe concentration along tongues boundaries in C3/C4 horizon boundaries (arrows), b) nodule surrounded by a reduced matrix in C2 horizon (P2RJ), c) Fe and Mn pore linings in root channels in the C2 horizon (P2RJ), and d) transversal section showing the tubular mottles in the C2 horizon (P2RJ)

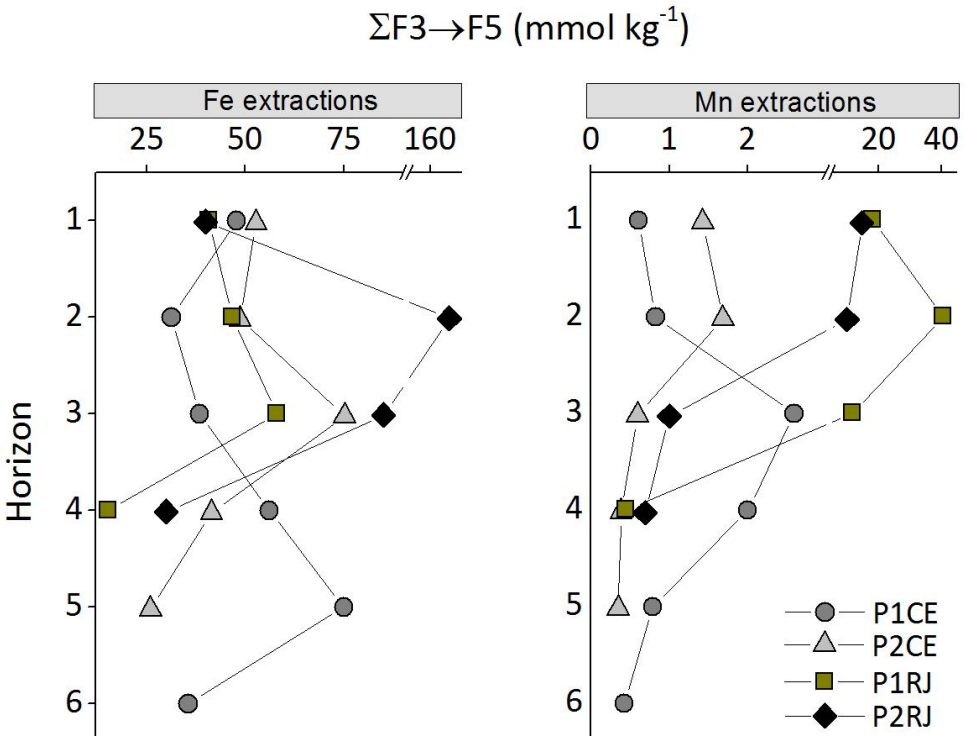

Fig. 13. Concentration of F3+F4+F5 throughout the soil profiles. Horizon numbers on the y axis refer to the order of horizons with depth for each profile (see Table 1 or 2); e.g., for P1CE profile: 1=A horizon, 2=C1 horizon, 3=C2 horizon, etc.

Participation of Mn in the redox processes seems to have greater influence at HTF-RJ since it has a similar trend to that of Fe. Low concentrations of exchangeable Mn and the F3+F4+F5 fraction (Fig. 13) in the deeper horizons, and higher concentrations in the uppermost horizons suggest that Mn is moving upward in the profile and precipitating. We hypothesize that Mn^{2+} produced from reductive processes in the deeper horizons precipitates as Mn oxyhydroxides in the uppermost horizons where the Eh values are higher, especially in the upper fringe where the water table oscillates (Smeck et al., 2002). Furthermore, Mn^{2+} has a relatively low oxidation kinetics, which favors Mn^{2+} to move through the soil profiles even in more oxidizing condition (Otero et al., 2003; Stumm and Morgan, 1981). Fig. 14 shows that part of Mn is precipitating along with ferrihydrite during the formation of Fe oxyhydroxides at HTF-RJ, where the nodules have strong effervescence when treated with H_2O_2. Nucleation and growth of Fe and Mn nodules is favored in soils with presence of ferrihydrite, leading to an expressive association between Fe and Mn in the nodules (McKenzie, 1989).

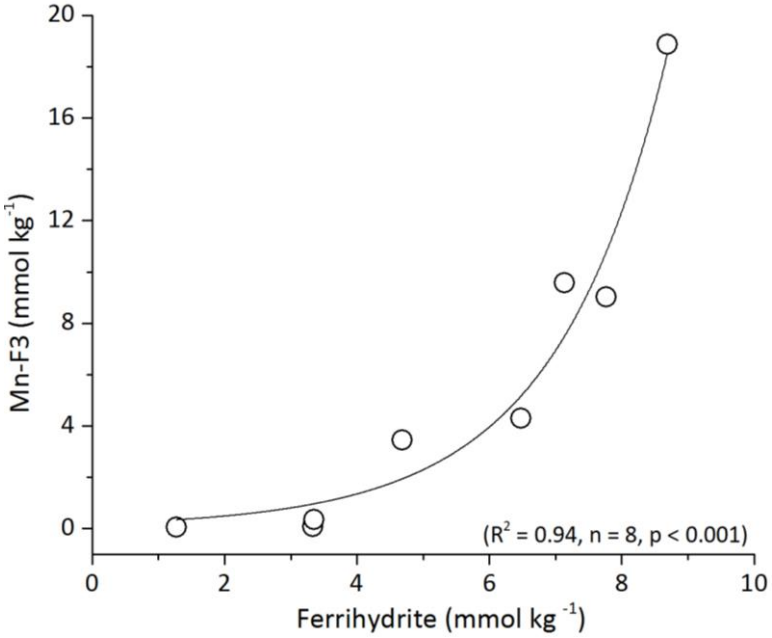

Fig. 14. Regression between ferrihydrite and Mn-F3 extraction

The same does not occur at HTF-CE, which present exchangeable Mn as the most abundant fraction. McKenzie (1975, 1989) pointed out that accumulation of Mn tends to occur in soils where both Mn and Fe oxyhydroxides are present. A lower concentration of the F3+F4+F5 fraction for Mn extractions (Fig. 13) and absent of nodules in the HTF-CE soils suggest that Mn precipitation is less favorable in the HTF-CE soils, which likely explains the maintenance of Mn in the exchangeable form at HTF-CE. Considering the horizons above the buried soils, these values (F3+F4+F5) fall between 9.5 and 40.4 mmol kg^{-1} for HTF-RJ soils, and 0.6 and 2.6 mmol kg^{-1} for HTF-CE soils. Therefore, the presence of nodules and a higher concentration of the F3+F4+F5 fraction in the HTF-RJ soils indicate a soil environment more propitious for Mn precipitation, and Mn withdrawal from the soil solution is caused by occlusion and sorption by iron precipitates (Collins and Buol, 1970). In addition, the composite Eh-pH stability diagram for Mn shows that Mn tends to occur as Mn^{2+} exactly in the deeper horizons (buried mangrove soils), which is mobilized through the soil profiles and then precipitates in the uppermost horizon where the Eh values are higher (Fig. 15).

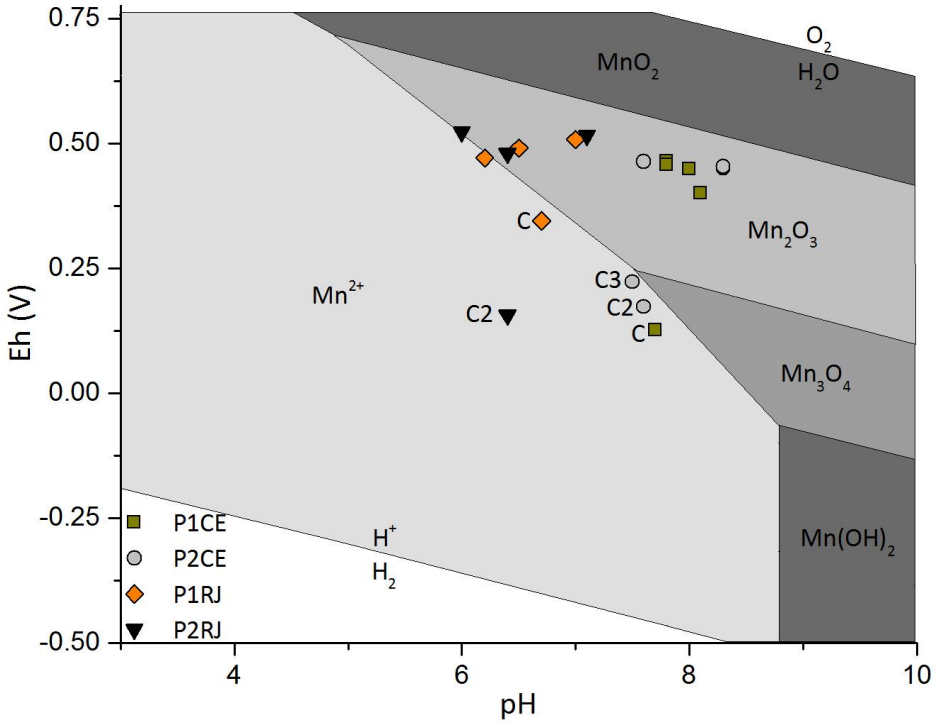

Fig. 15. Eh-pH diagram for Mn (adapted from Collins and Buol, 1970)

2.6. Conclusion

The present investigation of soil morphology and Fe and Mn geochemistry highlights the importance of redox reaction in controlling the pedogenesis of HTF soils. Even though some physical and chemical parameters differ greatly between the studied HTF soils (e.g. pH, particle size distribution, cation proportions, and Mn concentration), pedogenesis on both HTFs shows similar trends. Salinization, solonization, and redox reactions are the main pedogenetic processes taking place in HTF soils. Buried mangrove soils make up the deeper part of the soil profiles, and redox reactions have been transforming these buried soils due to more oxidizing conditions within the soil profiles. Overall, flooding events by tides and water table oscillation lead to mobilization of Fe^{2+} and Mn^{2+} upwards in the soils profiles, followed by oxidation and precipitation as oxyhydroxides. In addition, these reactions are leading to pyrite oxidation, formation of mottles, nodules, lining pores, and also formation of irregular and broken topographies of the horizon boundaries throughout the soil profiles. Participation of Mn on redox concentrations is more expressive in HTF-RJ soils, which precipitates with Fe during formation of redox concentrations. Although lepidocrocite comprises more than 50 % of total Fe extractions, co-precipitation of Mn and Fe seems to be related to ferrihydrite formation.

References

Albuquerque, A.G.B.M., Ferreira, T.O., Cabral, R.L., Nóbrega, G.N., Romero, R.E., Meireles, A.J.A., Otero, X.L., 2014a. Hypersaline tidal flats (*apicum* ecosystems): the weak link in the tropical wetlands chain. Environ. Rev. 22, 1-11.

Albuquerque, A.G.B.M., Ferreira, T.O., Nóbrega, G.N., Romero, R.E., Souza Júnior, V.S., Meireles, A.J.A., Otero, X.L., 2014b. Soil genesis on hypersaline tidal flats (HTF ecosystem) in a tropical semi-arid estuary (Ceará, Brazil). Soil Res. 52, 140-154.

AOAC, 1970. Official methods of the Association of Agricultural Chemists, eleventh ed., Washington D.C.

Berner, R.A., 1970. Sedimentary pyrite formation. Am. J. Sci. 268, 1-23.

Berner, R.A., 1984. Sedimentary pyrite formation: an update. Geochim. Cosmochim. Ac. 48, 605-615.

Bezerra, F.H.R., Amaro, V.E., Vita-Finzi, C., Saadi, A., 2001. Pliocene-Quaternary fault control of sedimentation and coastal plain morphology in NE Brazil. J. South Amer. Earth Sci. 14, 61-75.

Borges, H.V., Nittrouer, C.A., 2015. The paleo-environmental setting of Sepetiba Bay, Rio de Janeiro, Brazil, in the late Pleistocene: interpretations from high-resolution seismic stratigraphy. Rev. Bras. Geof. 33(3).

Bonnissel-Gissinger, P., Alnot, M., Ehrhardt, J.J., Behra, P., 1998. Surface oxidation of pyrite as a function of pH. Environ. Sci. Technol. 32, 2839-2845.

Böttcher, M.E., 1998. Manganese(II) partitioning during experimental precipitation of rhodochrosite-calcite solid solutions from aqueous solutions. Mar. Chem. 62, 287-297.

Brookins, D., G., 1988. Eh-pH diagrams for geochemistry, Springler-Velag, Berlin.

Collins, J.F., Buol, S.W., 1970. Effects of fluctuations in the Eh-pH environment on iron and/or manganese equilibria. Soil Sci. 110, 111-118.

Cornell, R.M., Schwertmann, U., 2003. The Iron Oxides, second ed. Wiley-VCH Verlag GmbH and Co. KGaA, Weinheim.

D'Amore, D.V., Stewart, S.R., Huddleston, J.H., 2004. Saturation, Reduction, and the formation of iron-manganese concretions in the Jackson-Frazier wetland, Oregon. Soil Sci. Soc. Am. J. 68, 1012-1022.

Embrapa, 2013. Sistema Brasileiro de classificação de solos, third ed. Brasília, DF.

Farrell, Jr., R.E., Brooks, R.A., 1971. The selective adsorption of sodium by clay minerals in lakes Pontchartrain and Maurepas, Louisiana. Clay. Clay Miner. 19, 75-81.

Ferreira, T.O., Otero, X.L., Souza Junior, V.S., Vidal-Torrado, P., Macías, F., Firme, L.P., 2010. Spatial patterns of soil attributes and components in a mangrove system in Southeast Brazil (São Paulo). J. Soils Sediment. 10, 995-1006.

Fitzpatrick, R.W., Fritsch, E., Self, P.G., 1996. Interpretation of soil features produced by ancient and modern processes in degraded landscapes. V. Development of saline sulfidic features in non-tidal seepage areas. Geoderma 69, 1-29.

Fortin, D., Leppard, G.G., Tessier, A., 1993. Characteristics of lacustrine diagenetic iron oxyhydroxides. Geochim. Cosmochim. Acta 57, 4391-4404.

Frings, P.J., Clymans, W., Fontorbe, G., De La Rocha, C.L., Conley, D.J., 2016. The continental Si cycle and its impact on the ocean Si isotope budget. Chem. Geol. 425, 12-36.

Furquim, S.A.C., Santos, M.A., Vidoca, T.T., Balbino, M.A., Cardoso, E.L., 2017. Salt-affected soils evolution and fluvial dynamics in the Pantanal wetland, Brazil. Geoderma 286, 139-152.

Gee, G.W., Or, D., 2002. Particle-size analysis, in: Dane, J.H., Topp, G.C. (Eds.), Methods of Soil analysis. Soil Science Society of America, Madison, Wisconsin, USA, p. 255-293

Hadlich, G.M., Ucha, J.M., 2009. Apicuns: aspectos gerais, evolução recente e mudanças climáticas globais. Rev. Bras. Geomorf. 10(2), 13-20.

Harron, W.R.A., Webster, G.R., Cairns, R.R., 1983. Relationship between exchangeable sodium and sodium adsorption ratio in a Solonetzic. Soil Association. Can. J. Soil Sci. 63, 461-467.

Hesp, P.A., Maia, L.P., Claudino-Sales, V., 2009. The Holocene Barriers of Maranhão, Piauí and Ceará States, Northeastern Brazil, in: Dillenburg, S., Hesp, P. (Eds.), Geology and geomorphology of Holocene coastal barriers of Brazil. Springer-Verlag, Berlin, Heidelberg, p. 325-343.

Huerta-Díaz, M.A., Morse, J.W., 1990. A quantitative method for determination of trace-metal concentrations in sedimentary pyrite. Mar. Chem. 29, 119-144.

Huminicki, D.M.C., Rimstidt, J.D., 2009. Iron oxyhydroxide coating of pyrite for acid mine drainage control. Appl. Geochem. 24, 1626-1634.

IUSS Working Group WRB, 2006. World reference base for soil resources. World Soil Resources Reports No. 103, FAO, Rome.

Kolditz, K., Dellwig, O., Barkowski, J., Bahlo, R., Leipe, T., Freund, H., Brumsack, H.J., 2012. Geochemistry of Holocene salt marsh and tidal flat sediments on a barrier island in the southern North Sea (Langeoog, North-west Germany). Sedimentology 59, 337-355.

Konsten, C.J.M., Adriesse, W., Brinkman, R., 1988. A field laboratory method to determine total potential and actual acidity in acid sulphate soils, in: Selected papers of the Dakar symposium on acid sulphate soils. International Institute for Land Reclamation and Improvement, Wageningen, The Netherlands, p. 106-134.

Lindbo, D.L., Stolt, M.H., Vepraskas, M.J., 2010. Redoximorphic features, in: Stoops, G., Marcelino, V., Mees, F. (Eds.), Interpretation of micromorphological features of soils and regoliths. Elsevier, Amsterdam, The Netherlands, p. 129-148.

Malengreau, N., Bedidi, A., Müller, J.P., Herbillon, A.J., 1996. Spectroscopic control of iron oxide dissolution in two ferralitic soils. Eur. J. Soil Sci. 47, 13-20.

McKenzie, R.M., 1975. An electron microprobe study of the relationships between heavy metals and manganese and iron in soils and ocean floor nodules. Aust. J. Soil Res. 13, 177-188.

McKenzie, R.M., 1989. Manganese oxides and hydroxides, in: Dixon, J.B., Weed, S.B. (Eds.), Minerals in Soil Environments. SSSA Book Series, No. 1, Soil Science Society of America, Madison, Wisconsin, p. 439-465.

Mucci, A., 1988. Manganese uptake during calcite precipitation from seawater: conditions leading to the formation of a pseudokutnahorite. Geochim. Cosmochim. Acta 52, 1859-1868.

Muehe, D., Lima, C.F., Lins-de-Barros, F.M., 2006. Rio de Janeiro, in: Muehe, D. (Ed.), Erosão e progradação no litoral brasileiro. MMA, Brasília, p. 265-296.

Nóbrega, G.N., Ferreira, T.O., Siqueira Neto, M., Queiroz, H.M., Artur, A.G., Mendonça, E.S., Silva, E.O., Otero, X.L., 2016 Edaphic factors controlling summer (rainy season) greenhouse gas emissions (CO_2 and CH_4) from semiarid mangrove soils (NE-Brazil). Sci. Total Environ. 542, 685-693.

Otero, X.L., Ferreira, T.O., Huerta-Díaz, M.A., Partiti, C.S.M., Souza, Jr. V., Vidal-Torrado, P., Macías, F., 2009. Geochemistry of iron and manganese in soil and sediments of a mangrove system, Island Pai Matos (Cananeia – SP, Brazil). Geoderma 148, 318-335.

Otero, X.L., Huerta-Diaz, M.A., Macias, F., 2003. Influence of a turbidite deposit on the extent of pyritization of iron, manganese and trace metals in sediments from the Guaymas Basin, Gulf of California (Mexico). Applied Geochem. 18, 1149-1163.

Reddy, K.R., DeLaune, R.D., 2008. Biogeochemistry of wetlands, Taylor & Francis Group, Boca Raton, FL.

Richards, L.A., 1954. Diagnosis and improvement of saline and alkali soil. United States Salinity Laboratory Staff, USDA, Washington, D.C.

Ridd, P.V., Stieglitz, T., 2002. Dry Season Salinity Changes in Arid Estuaries Fringed by Mangroves and Saltflats. Estuar. Coastal Shelf Sci. 54, 1039-1049.

Rytwo, G., Banin, A., Nir, S., 1996. Exchangeable reactions in the Ca-Mg-Na-montmorillonite system. Clay. Clay Miner. 44(2), 276-285.

Santos, J.C.B., Le Pera, E., Souza Júnior, V.S., Corrêa, M.M., Azevedo, A.C., 2017. Gneiss saprolite weathering and soil genesis along an east-west regolith sequence (NE Brazil). Catena 150, 279-290.

Sayles, F.L., Mangelsdorf Jr., P.C., 1977. The equilibration of clay mineral with seawater: exchange reaction. Geochim. Cosmochim. Acta 41, 951-960.

Scheinost, A.C., Chavernas, A., Barrón, V., Torrent, J., 1998. Use and limitations of second-derivative diffuse reflectance spectroscopy in the visible to near-infrared range to identify and quantify Fe oxide minerals in soils. Clay. Clay Miner. 46(5), 528-536.

Schoeneberger, P.J., Wysocki, D.A., Benham, E.C., Broderson, W.D., 2002. Field Book for Describing and sampling soils, version 2.0. Natural Resources Conservation Service, National Soil Survey Center, Lincoln, NE.

Schwertmann, U., Fanning, D.S., 1976. Iron and manganese concretions in hydrosequences of soils in loess in Bavaria. Soil Sci. Soc. Am. J. 40, 731-738.

Schwertmann, U., Taylor, R.M., 1989. Iron oxides, in: Dixon, J.B., Weed, S.B. (Eds.), Minerals in Soil Environments. SSSA Book Series, No. 1, Soil Science Society of America, Madison, Wisconsin, p. 379-438.

Smeck, N.E., Bigham, J.M., Guertal, W.F., Hall, G.F., 2002. Spatial distribution of lepidocrocite in a soil hydrosequence. Clay Miner. 37, 687-697.

Soil Survey Staff, 2014. Keys to Soil Taxonomy. 12th ed. USDA-Natural Resources Conservation Service, Washington, DC.

Sperlich, P., Schaefer, H., Fletcher, S.E.M., Guillevic, M., Lassey, K., Sapart, C.J., Röckmann, T., Blunier, T., 2015. Carbon isotope ratios suggest no additional methane from boreal wetlands during the rapid Greenland Interstadial 21.2. Global Biogeochem. Cy. 29, 1962-1976.

Stumm, W., Morgan, J.J., 1981. Aquatic chemistry. John Wiley and Sons, New York.

Sundby, B., Vale, C., Caçador, I., Catarino, F., Madureira, M.J., Caetano, M., 1998. Metal-rich concretions on the roots of salt marsh plants: mechanism and rate of formation. Limnol. Oceanogr. 43(2), 245-252.

Tessier, A., Campbell, P.G.C., Bisson, M., 1979. Sequential extraction procedure for the speciation of particulate trace metals. Anal. Chem. 51, 844-851.

Ucha, J.M., Hadlich, G.M., Celino, J.J., 2008. Apicum: Transição entre solos de encostas e de manguezais. Revista E.T.C. 5, 58-63.

USDA, 2014. Soil Survey Field and Laboratory Methods Manual. United States Department of Agriculture Natural Resources, Conservation Services (NRCS), Soil Survey Investigations Report No. 51, Version 2.

Vepraskas, M.J., 2001. Morphological features of seasonally reduced soils, in: Richardson, J.L., Vepraskas, M.J. (Eds.), Wetland soils. Boca Raton, Florida, p. 163-182.

Vepraskas, M.J., 2004. Redoximorphic features for identifying aquic conditions. Technical Bulletin 301, North Carolina Agricultural Research Service, Raleigh, North Caroline.

van Breemen, N., Buurman, P., 2003. Soil Formation, second ed. Kluwer Academic Publ, New York.

Walkley, A., Black, I.A., Armstrong, I., 1934. An examination of the Degtjareff method for determining soil organic matter, and a proposed modification of the chromic acid titration method. Soil Sci. 37, 29-38.

3. ARE HYPERSALINE TIDAL FLAT SOILS A POTENTIAL SILICON SINK IN COASTAL WETLANDS?

Abstract

Hypersaline tidal flats (HTF) are transitional ecosystems which play an important role over Si biogeochemistry in wetlands. Source-sink dynamics of Si in these ecosystems are directly dependent on pedogenesis and are strongly influenced by the readily soluble Si components, such as dissolved Si, adsorbed Si, and amorphous silicates. The aim of this study was to identify and assess the distribution of readily soluble Si pool in two HTFs on the Brazilian coast. We based our studies on Si and Fe sequential extractions, modeling of the soil saturated paste, and X-ray diffraction of the fine clay fraction. Our results show that mobile Si and adsorbed Si are present at very low levels in HTF soils, comprising less than 3 % of the readily soluble Si pool. Si associated with Fe oxyhydroxides is the second largest component of the readily soluble Si pool, making up 8.7 - 40.8 % of the Si extractions. The correlation between ferrihydrite and Si associated with Fe oxyhydroxides indicates a large control of Si by ferrihydrite. Amorphous Si makes up the dominant fraction, comprising 59 – 90 % of the Si extractions. SEM images show the presence diatoms, sponges, and phytoliths in the soils. Precipitation of pedogenic opal seems to occur in the soils due to a dry season at both sites. The clay assemblages are composed of the mixed-layered kaolinite-smectite (K-S), kaolinite-illite (K-I), and illite-smectite (I-S), and lesser amounts of kaolinite (K) and smectite (S) end-members. The presence of these clays indicates that HTF soils are conducive to the formation of mixed-layered minerals, which partially control Si dynamics. Our data indicate that HTF soils tend to accumulate Si by adsorption, (co)precipitation, and reactions involving clay minerals.

Keywords: Silicon; Amorphous silica; Pedogenic processes; Redox reactions; Iron oxyhydroxides; Biogenic opal

3.1. Introduction

Silicon (Si) is the second most abundant element in the Earth crust and an essential nutrient for most living organisms in marine and terrestrial ecosystems (Conley, 2002; Sommer et al., 2006). This element is ubiquitous in soils and a basic constituent of soil liquid, adsorbed, and solid phases (Sauer et al., 2006). Even though most soils contain Si, the distribution of the different Si components within the Si pool varies widely depending on a broad array of factors, such as the influence of pedogenetic processes, parent material, soil chemical and physical properties (e.g. pH, redox potential, temperature, particle size distribution), intensity of leaching, biological cycling, and mineral formation and alteration (Monger and Kelly 2002; Cornelis et al., 2014).

Regardless of which factors are involved, it is well known that the pedosphere plays a major role in controlling Si dynamics in environments (Derry et al., 2005; Sommer et al., 2006;

Cornelis et al., 2011). About 80 % of dissolved Si input to the ocean is transported by rivers (Tréguer et al., 1995), and Si export to rivers is largely dependent on the soil formation processes (Conley, 2002; Borreli et al., 2010; Struyf and Conley, 2012). Therefore, soils can promote the release of Si to marine and terrestrial ecosystems (Sommer et al., 2006; Struyf and Conley, 2009), or even retard Si output to rivers and oceans (Meunier et al., 1999).

The interplay of some specific soil conditions is essential to understand the Si dynamics in terrestrial and aquatic ecosystems (Cornelis et al., 2014; Georgiadis et al., 2017), such as ion activities, pH, and salinity (Drees et al., 1989). In general, the solubility of silica increases in soils affected by salts and under high pH values (Loucaides et al., 2008). pH values between 2.5 and 8.5 do not favor the release of Si from the soil solid phase. This process is enhanced in higher pH values due to the dissociation of monomeric silicic acid (H_4SiO_4) to deprotonated forms (e.g. $H_3SiO_4^-$ and $H_2SiO_4^{2-}$). Nevertheless, the dissolution of silica in near-neutral pH can also take place due to the nucleophilic reaction of water at the solid-solution interface (Dove and Crerar, 1990). Dissolved silicon availability is also favored in high saline systems because of the higher catalytic effect of salt solutions (e.g. seawater, Loucaides et al., 2008). These conditions are commonly found in evaporative environments (Albuquerque et al., 2014a; Furquim et al., 2010b). In these ecosystems, the evaporative concentration of waters can cause an increase in soil salinity and pH values.

Hypersaline tidal flat soils are evaporative environments distributed worldwide and commonly found on the Brazilian coastline. These soils have very high salinities and commonly pH values above 8 (Albuquerque et al., 2014b) and therefore may be of high importance for the biogeochemical cycling of nutrient silicon across the land to ocean transition. Thus, research is needed to provide insights into the role of these soils in controlling the Si dynamics in coastal ecosystems. This study aims to 1) identify the main Si pools in HTF soils and estimate the distribution of its components, and 2) define the processes involved in source-sink Si dynamics in HTF soils. To address these objectives, two HTFs were studied based on specific Si and Fe extractions, modeling of the soil aqueous phase, and X-ray diffraction of the fine clay fraction.

3.2. Materials and methods

Three soil profiles were sampled at each site during low tide (Fig. 1). Soil profiles were labeled as P1CE, P2CE, and P3CE (HTF on the NE coast, HTF-CE), and P1RJ, P2RJ, and P3RJ

(HTF on the SE coast, HTF-RJ). Detailed soil morphological descriptions were made of each soil profile at both sites before sampling the selected soil horizons. pH and Eh values were determined in the field using a glass electrode and an oxidation-reduction potential Pt electrode, respectively. Eh final readings were corrected by adding the potential of a calomel reference approximately (244 mV).

Three soil horizons of each soil profile were chosen for the specific Fe and Si extractions: i) surface horizons (A horizons of P1CE, P2CE, P3CE, P1RJ, P2RJ, and P3RJ), ii) intermediary horizons (C3 of P1CE, C2 of P2CE, C1 of P3CE, C2 of P1RJ, C1 of P2RJ, and C1 of P3RJ), and iii) deeper horizons (C4 of P1CE, C3 of P2CE, C2 of P3CE, C3 of P1RJ, C3 of P2RJ, and C3 of P3RJ). Collected samples were maintained at 4 ^{o}C during transportation to the laboratory. A portion of the samples was air dried in preparation for specific Si extractions and saturation extracts, and another portion was stored at low temperature (-5^{o}C) to avoid Fe oxidation.

The Si sequential extraction methodology consisted of a combination of the method developed by Georgiadis et al. (2013) and the scheme used by Cornelis et al. (2011). Briefly, the Si fractions include: 1) mobile Si (Si_{mob}), extracted with 0.01 mol L^{-1} $CaCl_2$; 2) adsorbed Si (Si_{ad}), extracted with 0.01 mol L^{-1} acetic acid solution; 3) Si bound to poorly ordered oxyhydroxides (Si_{ox}), extracted with 0.20 mol L^{-1} ammonium oxalate-oxalic acid at pH 3; 4) amorphous Si (Si_{alk}), extracted with 0.02 mol L^{-1} NaOH; and 5) total Si (Si_t), obtained by X-ray fluorescence. Soil samples were rinsed with distilled water between each extraction. Si extracts were filtered and analyzed by ICP-OES (*Horiba* Ultima 2).

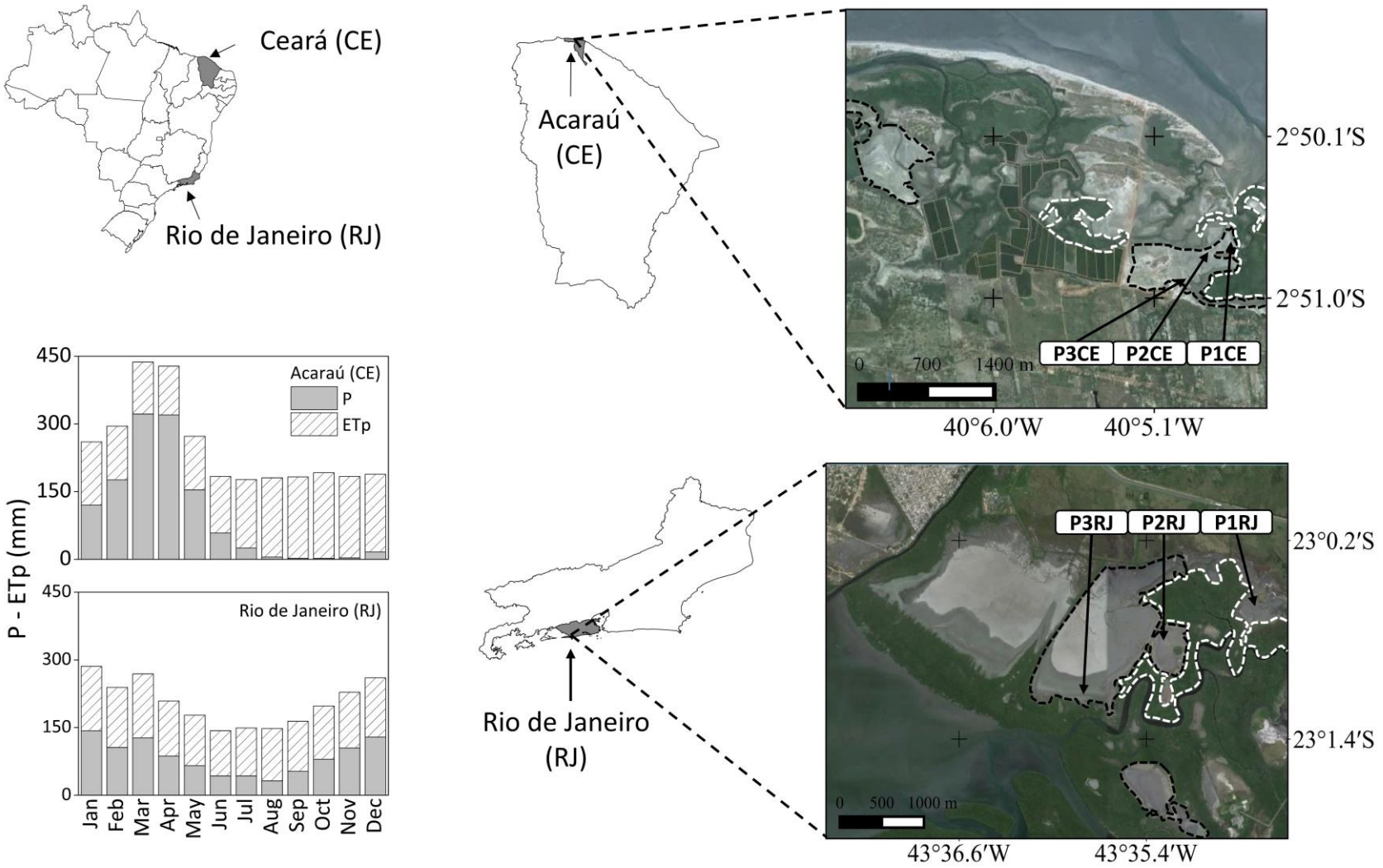

Fig. 1. Location of the study sites and soil profiles. The white and black dashed lines delineate the mangrove forests and HTFs, respectively. Images source: Google™ Earth (2015)

Samples for XRF analysis were prepared by the loose-powder method and were analyzed using a ED-XRF (SPECTRO XEPOS HE). Between 2.0 and 5.0 g of ground sediment was placed in a plastic cup fitted with a thin layer of polypropylene Prolene film (Chemplex). X-rays were generated with a 50-watt X-ray tube. Measurements were performed in a He atmosphere to minimize X-ray attenuation. Bulk elemental abundance was calculated based on the intensity of the characteristic fluorescent X- rays of each element (Schaefer et al., 2017). The percentage of the readily soluble Si pool (Si_{mob} + Si_{ad} + Si_{ox} + Si_{alk}) in the total Si pool (Si_t) was plotted: 100*(Si_{mob} + Si_{ad} + Si_{ox} + Si_{alk})/Si_t.

Fe extractions were performed on wet samples to avoid Fe oxidation using a sequential extraction procedure derived from a combination of methods proposed by Tessier et al. (1979), Huerta-Díaz and Morse (1990), and Fortin et al. (1993). This methodology has been used widely for wetland soils (for more details see Otero et al., 2009; Ferreira et al., 2015), and allows differentiation of five operationally-defined fractions: exchangeable Fe (Fe_{ex}); Fe associated with carbonates (Fe_{ca}); ferrihydrite; lepidocrocite; and crystalline Fe oxyhydroxides (Fe_{cry}). Soil samples were rinsed with distilled water between each extraction. Aqueous extracts were analyzed by atomic absorption spectroscopy *(Perkin Elmer 1100B).*

Biogenic opal was obtained from the P1CE and P1RJ soil profiles by densimetric separation. Organic matter was removed using H_2O_2 30% v/v, and Fe oxyhydroxides were removed by dithionite-citrate-bicarbonate method (Mehra and Jackson, 1960). The clay fraction was removed by centrifugation (Jackson 1979). Biogenic opal was concentrated by heavy liquid separation with sodium polytungstate ($[Na_6(H_2W_{12}O_{40})H_2O]$, d = 2.3 g cm^{-3}, Madella et al., 1998). SEM backscattered electron images of biogenic opals were obtained with a high-resolution scanning electron microscope (*FEI NNS450*).

Soil extracts were prepared using the two uppermost horizons of each soil profile (USDA, 2014). Soil extracts were collected by centrifugation at 5,000 rpm for 20 min, and the solutions were filtered through 0.45 µm Millipore filter. Exchangeable Na^+ and K^+ were determined by flame photometry, and Ca^{2+} and Mg^{2+} by atomic absorption spectroscopy. Silicon, Al, Fe, P, and S were determined by ICP-OES (*Thermo Scientific iCAP 6000 series*). Ion Cl^- was measured using a specific electrode (Mettler Toledo PerfectIon Combination Chloride Electrode). Alkalinity was determined by titration with H_2SO_4. Electrical conductivity (EC) was measured using a benchtop conductivity meter.

Geochemical modeling to estimate H_4SiO_4 activity was performed using the program PHREEQC (Parkhurst, 1995), which applies ion-pair model based on the extended Debye-Hückel equation. We estimated the activities of H_4SiO_4 in two different ways: 1) modeling the soil solution using concentration of cations and anions measured in the saturation extracts, and 2) simulating a soil environment where 95 % of soil porewater was removed by evaporation (Parkhurst et al., 1996). The latter allows calculation of variations in H_4SiO_4 activity caused by the drying process in HTF soils, which is a real condition since we found soil moisture values of less than 10 % during the dry season at both sites.

The fine clay fraction (< 0.2 µm) of C3 (P1CE) and C2 (P1RJ) horizons was investigated by X-ray diffraction (XRD). Organic matter was removed by oxidation using H_2O_2 30% v/v, and pedogenic Fe oxyhydroxides were removed by dithionite-citrate-bicarbonate method (Mehra and Jackson, 1960). The sand fraction was separated by wet sieving after dispersion of the suspension with 0.01 mg L^{-1} Na_2CO_3. Silt and clay fractions were separated by sedimentation. Fine clay was obtained by successive centrifugations (4,100 rpm for 20 min). Oriented mounts were prepared on glass slides, with the following treatments: i) saturation with $MgCl_2$ at room temperature, ii) ethylene glycol solvation by exposing them to the reagent at 60 ^oC for 20 h, and iii) thermal treatment at 550 ^oC. Samples were scanned from 3 to 30 $^o2\theta$, with 0.02 $^o2\theta$ step size and count time of 3 s/step, using a *Rigaku Miniflex II* (CuKα radiation). Identification and quantification of the clay phases were performed using the software Newmod 3.2.1 (Reynolds and Reynolds, 1996). The input variables for the modeling include all the important structural data and settings that describe the optical configuration of the diffractometer used (Reynolds and Reynolds, 1996).

3.3. Results

3.3.1. Solid-phase distribution of Si

Concentration of the different Si components obtained by specific Si extractions varies greatly with depth and between the soil profiles (Fig. 2). HTF soils display very low concentrations of mobile Si (Si_{mob}) and exchangeable Si (Si_{ad}) when compared to Si associated with Fe oxyhydroxides (Si_{ox}) and amorphous Si (Si_{alk}), comprising less than 3 % of the total extractions. Mean values in mg L^{-1} for all soil horizons are 0.06 ± 0.03 (Si_{mob}), 0.19 ±0.20 (Si_{ad}), 3.56 ± 3.21 (Si_{ox}), and 11.79 ± 11.36 (Si_{alk}).

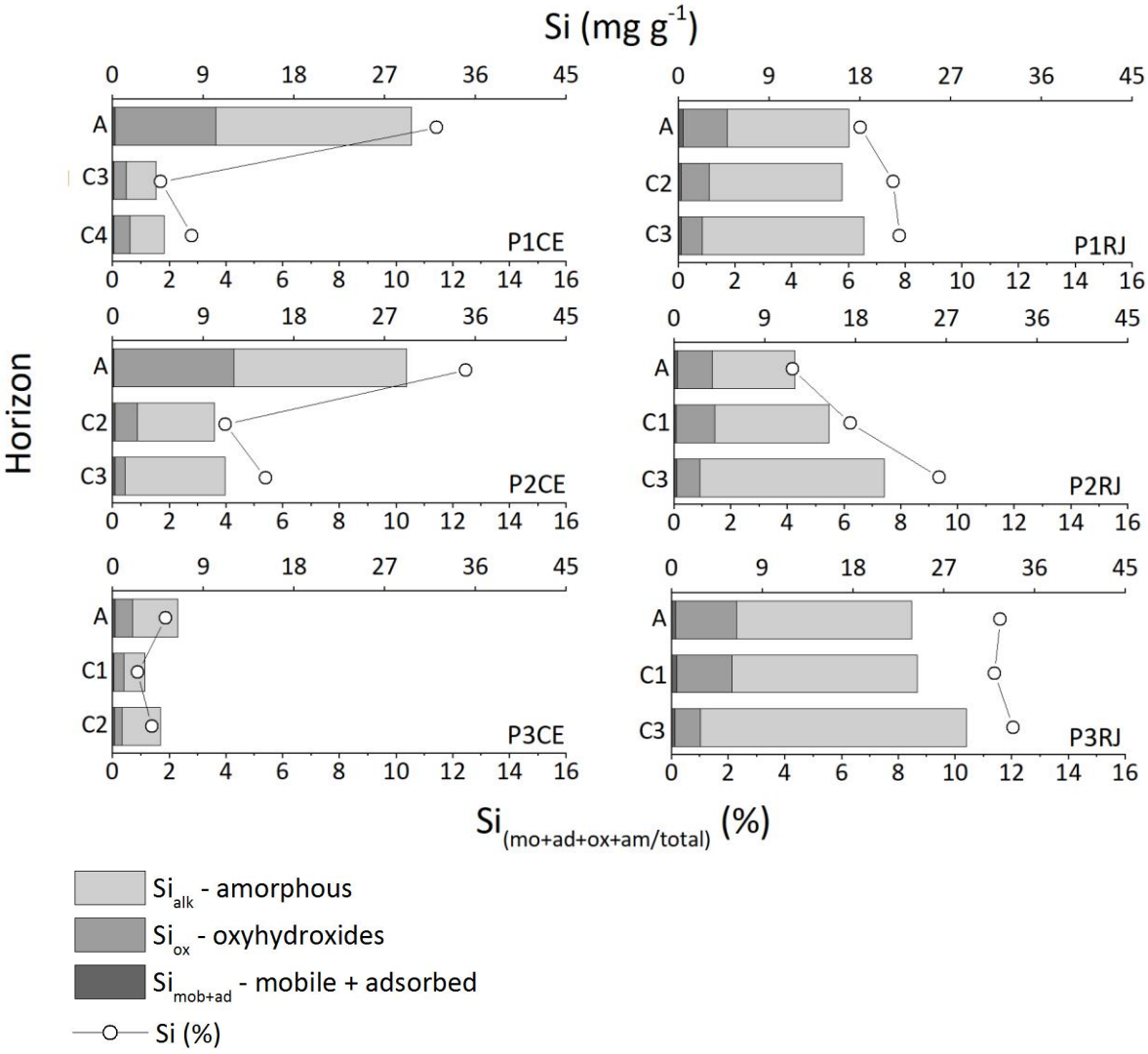

Fig. 2. Si sequential extractions of the soil profiles

In general, Si_{ox} concentrations are higher in the uppermost horizons and tend to decrease with depth in both study sites (Fig. 2). This fraction comprises 8.7 to 40.8 % of the readily soluble Si pool and ranges from 0.7 to 11.9 mg g^{-1}. The uppermost horizons of the P1CE and P2CE soil profiles have the highest Si_{ox} concentrations (10.0 and 11.9 mg g^{-1}, respectively), which decrease to less than 2.3 mg g^{-1} in the subjacent ones. By contrast, Si_{ox} concentrations fall between 0.7 and 1.7 mg g^{-1} in P3CE. HTF-RJ soils display more homogeneous distributions of Si_{ox} as a function of depth, varying from 2.1 to 6.0 mg g^{-1}.

Amorphous Si (Si_{alk}) is the dominant Si fraction in all soil horizons, comprising 59 to 90 % of the readily soluble Si pool. The P1CE soil profile has a Si_{alk} concentration of 19.4 mg g^{-1} in the uppermost horizon and approximately 3.0 mg g^{-1} in the subjacent ones. P2CE shows a similar decrease in Si_{alk} as a function of depth, with 17.1 mg g^{-1} in the A horizon and

decreasing to 7.6 mg g^{-1} in C2 and 10.0 mg g^{-1} in C3. The P3CE profile exhibited Si_{alk} content varying from 2.1 to 4.5 mg g^{-1} throughout the soil profile, with the highest value in the topsoil. By contrast, opposite trend occurs in HTF-RJ soils, where the Si_{alk} concentration is higher in the deepest horizons. The Si_{alk} varies from approximately 13.0 mg g^{-1} (A and C2 horizons) to 16 mg g^{-1} (C3 horizon) in P1RJ, 10.0 mg g^{-1} (A and C1 horizons) to 18.3 mg g^{-1} (C3 horizon) in P2RJ, and 18.0 mg g^{-1} (A and C1 horizons) to 26.4 mg g^{-1} (C3 horizon) in P3RJ.

Even though Si_{alk} and Si_{ox} represent together the dominant fraction in the readily soluble Si pool, the contribution of these fractions to the total Si pool (Si_t) varies from 1 to 11 % (HTF-CE) and 0.2 to 5.1 % (HTF-RJ), respectively. The contribution of Si_{mob} and Si_{ad} fractions to Si_t is less than 0.2 %. Overall, the contribution of the readily soluble Si pool is most strongly expressed in the surface horizons at HTF-CE and in the deeper horizons at HTF-RJ.

3.3.2. Solid-phase distribution of Fe

Exchangeable Fe (Fe_{ex}) and Fe associated with carbonates (Fe_{ca}) show very low values, comprising 5.5 % (1.4 µmol kg^{-1}) of the Fe extractions (Fig. 3). Ferrihydrite and lepidocrocite make up approximately 76 % of the total extractions. Lepidocrocite is the dominant fraction in both sites and contributes 59 % (30 µmol kg^{-1}) at HTF-CE and 57 % (25.7 µmol kg^{-1}) at HTF-RJ, whereas for ferrihydrite the proportion is 23 % (10.5 µmol kg^{-1}) at HTF-CE and 13 % (5.2 µmol kg^{-1}) at HTF-RJ. The highest lepidocrocite concentrations are found in the intermediary horizons in the HTF-CE soils, with 73 % in P1CE and P2CE, and 93 % in the P3CE, decreasing to less than 55 % in the underlying horizons. Ferrihydrite is most abundant in the topsoil. For most soil profiles, the proportion of crystalline Fe oxides (Fe_{cry}) varies from 3 to 36 % (1.2 - 7.8 µmol kg^{-1}). The intermediary horizon of the P2RJ profile has an atypical Fe_{cry} concentration (137.9 µmol kg^{-1}), which is likely due to the greater number of nodules in this section of the soil profile.

3.3.3. XRD study

X-ray diffraction showed the fine clay contains kaolinite (peaks at 0.72 and 0.36 nm), smectite (peaks at 1.75-1.80 nm, after glycol solvation), and illite (peaks at 1.0 and 0.34 nm) in both sites (Fig. 4 and Table 1). Peaks related to kaolinite disappeared after thermal treatment at 550 °C (not shown). The smectite peak shifted to 1.70-1.80 nm after glycol solvation and to 1.0 after thermal treatment. The illite peaks were not affected by either

treatment. P1RJ displays a more intense peak for smectite and a lower peak intensity for illite when compared to P1CE.

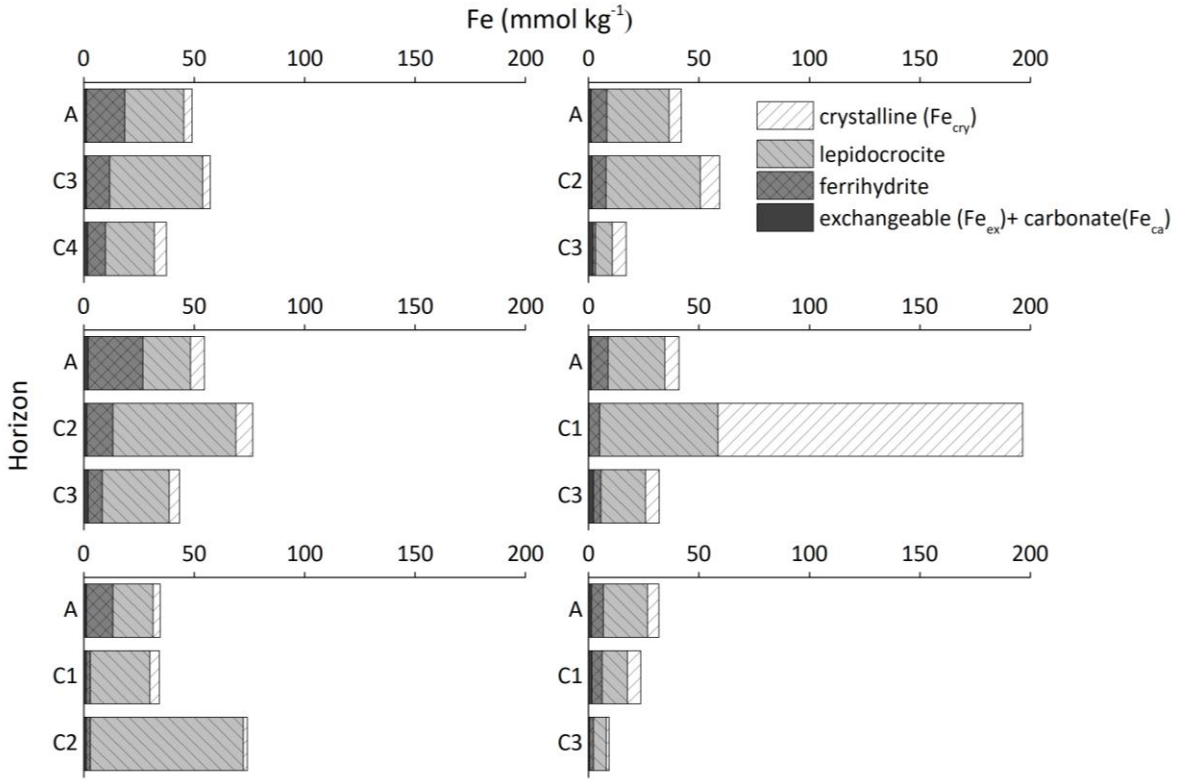

Fig. 3. Fe sequential extractions of the soil profiles

Although kaolinite and smectite end-members are present, XRD modeling results indicate a predominance of R0 mixed-layered minerals in HTF soils (Table 1). In addition to kaolinite and smectite end-members, kaolinite-smectite (K-S), kaolinite-illite (K-I), and illite-smectite (I-S) mixed-layered minerals were introduced to achieve a better fitting between the experimental and calculated patterns. K-S is the most abundant phase in both samples and occurs in a range of kaolinite layers (96 %, 95 %, 88 %, 21 %, 16 %, and 10 %). XRD data indicate the presence of a kaolinite end-member mineral with larger coherently diffracting domain sizes (N_{max} and N_{med}) than the other minerals. On the other hand, K-S phases and smectite end-member have low coherently diffracting domain sizes. Considering the total layer proportion of each clay mineral, kaolinite is the predominant clay mineral in HTF soils.

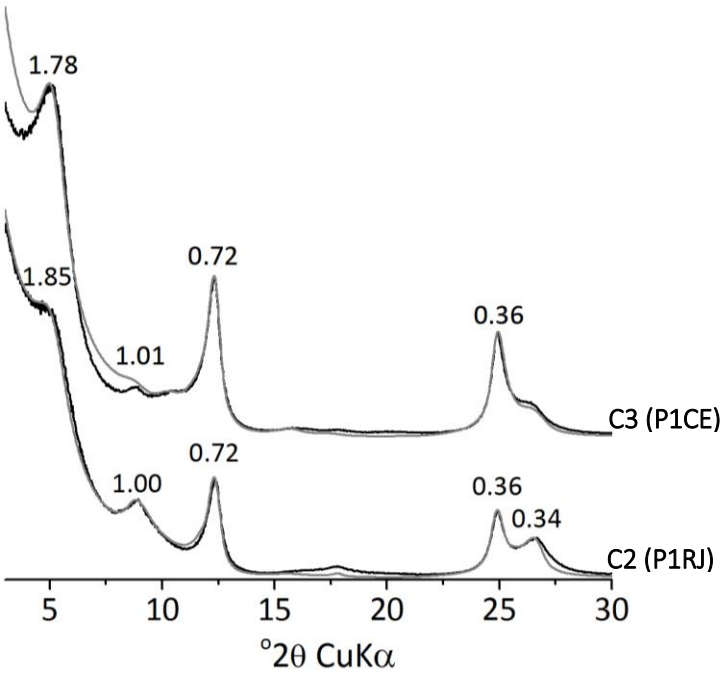

Fig. 4. XRD modeling of fine clay samples. Gray line: calculated patterns, black line: experimental pattern

Table 1. Parameters from modeling of glycolated clay samples

Horizon	Components	% layers	Fe kao	Fe sm	Fe il	K il	Nmax	Nmed	% phase
				P1CE					
	K	100	0.42		-	-	30	19	13.9
	K-S	95-5	0.34	0.64	-	-	23	14.8	16.4
	K-S	88-12	0.20	0.76	-	-	18	3.1	17.1
C3	K-S	16-84	1.15	0.69	-	-	9	1.8	13.8
(P1CE)	I-S	91-9	-	0.50	0.46	0.80	11	4.9	10.4
	K-I	79-21	0.10	-	0.40	0.80	14	7	9.9
	I-S	5-95	-	0.70	0.53	0.75	7	1.2	14.1
	S	100	-	0.87	-	-	6	1.2	5.4
				P1RJ					
	K	100	0.16	-	-	-	29	14.9	14.4
	K-S	96-4	0.12	0.86	-	-	14	9.2	13.1
	I-S	89-11	-	0.90	0.41	0.71	23	12.8	12.0
C2	K-S	21-79	0.44	1.34	-	-	8	1.0	14.1
(P1RJ)	K-S	10-90	0.27	1.12	-	-	8	1.4	18.2
	I-S	50-50	0	0	0.62	0.70	15	6.0	4.8
	K-I	20-80	0.34	-	1.01	0.7	13	6.0	7.8
	K-I	63-37	0	-	0.37	0.77	19	4.7	15.6

3.3.4. SEM study

SEM analysis revealed the presence of different types of biogenic opal in the soils. Diatoms, sponge spicules, and phytoliths are present in most of the horizons. The main phytolith types include block, bulliform, globular echinate, and parallelepipedal. Biogenic opal distribution through the soil profiles is heterogeneous and not found in all soil horizons of both sites. SEM images indicate that diatoms and sponge spicules are more abundant than

phytoliths in the deepest horizons (Fig. 5c, d, and h). In contrast, the uppermost horizons seem to have higher proportions of phytoliths.

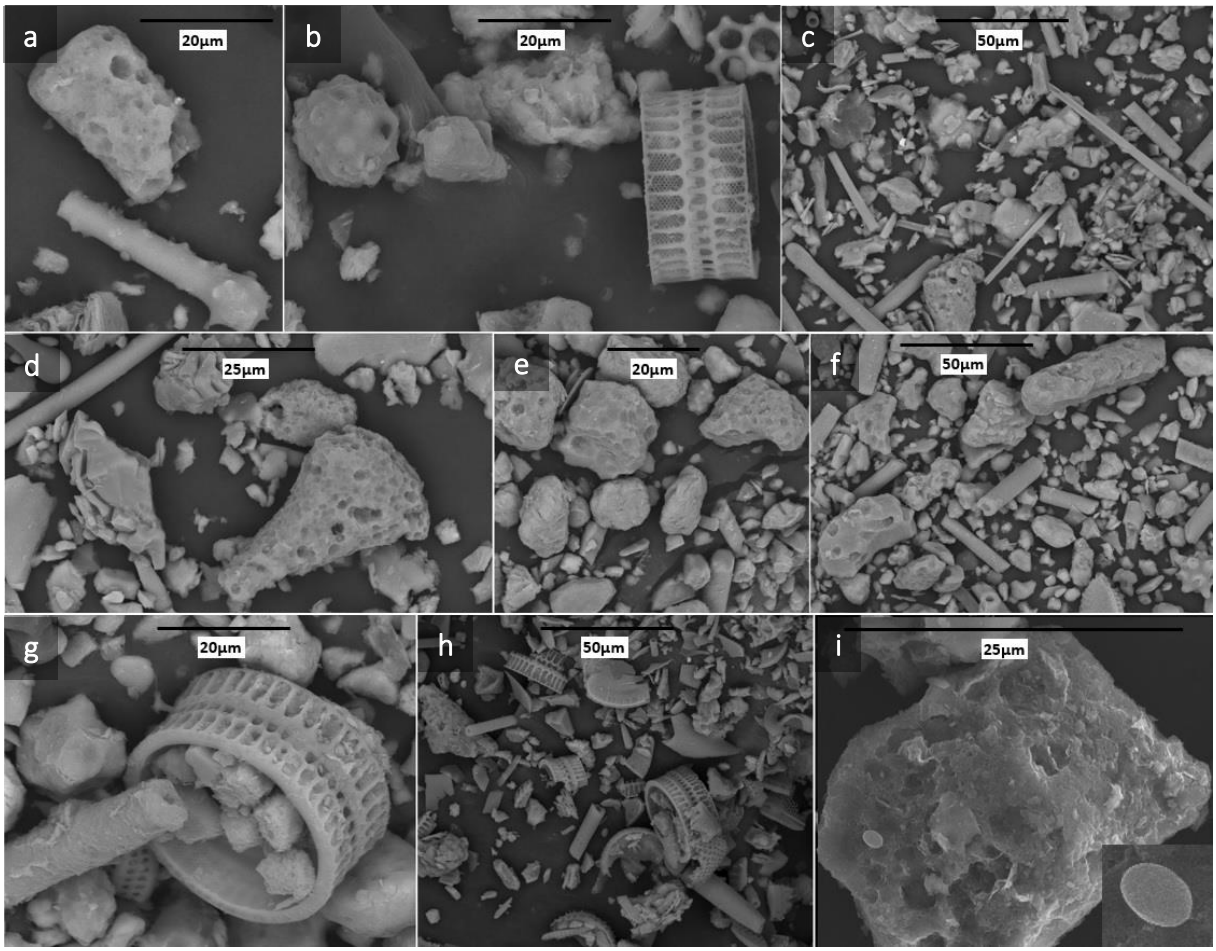

Fig. 5. Examples of SEM images of biogenic opal. a and b) C3 horizon (P1CE); c and d) C4 horizon (P1CE); e, f, and g) A horizon (P1RJ), h) C3 horizon (P1RJ); i) opaline spheres in the C3 horizon (P1CE)

3.4. Discussion

Silica dynamics in HTF soils on the Brazilian coastline are unknown. Here we provide important results regarding the distribution and identification of the Si pool in these soils using a combination of geochemical, XRD, XRF, and electron microscopy analysis. Silicon dynamics show similar trends in both sites. Adsorption and mineral authigenesis (e.g. formation of ferrihydrite) seems to be the most important reactions controlling Si dynamics in HTF soils.

3.4.1. Influence of Fe oxyhydroxides on Si dynamics

The $CaCl_2$ extraction (Si_{mob}) is assumed to extract water-soluble Si, and the acetic acid (Si_{ad}) extraction is used to assess soluble Si and some of the exchangeable Si from soils (Sauer

et al., 2006). These fractions, together defined as easy-mobilize Si of the readily soluble Si pool (Georgiadis et al., 2014), display very low concentrations in the soil profiles (Fig. 2). It seems that Si reacts preferentially with the Fe oxyhydroxides and/or precipitates as amorphous Si or opal coatings on pedogenic phases in the soils.

HTF soils experience periodic flooding events and water table oscillation, leading to a strong expression of redox processes. These conditions favor the formation of very reactive Fe oxyhydroxides with a high capacity to withdraw silicic acid from soil solution by mineral adsorption and co-precipitation reactions (Carlson and Schwertmann, 1981; Gehlen and Raaphorst, 2002; Delstanche et al., 2009). Such silica-iron associations can be very stable due to aqueous Fe-Si complexation during the Fe(III) hydrolysis to form Fe oxyhydroxides (Pokrovski et al., 2003). Fig. 6a shows the regression between the concentrations of ferrihydrite and Si_{ox} ($r=0.62$, $n=18$, $p<0.001$). Higher concentrations of Si_{ox} and ferrihydrite were found in the uppermost horizons (Fig. 2 and Fig. 3). Ferrihydrite is a poorly ordered mineral and is characterized by its high specific surface area and proportion of reactive sites, which can catalyze monomeric or oligomeric silica deposition on its surface (Williams and Crerar, 1985). The interaction between silicic acid and ferrihydrite involves both adsorption and polymerization, and also has a significant effect on the adsorption of anionic species (Swedlund and Webster, 1999). This mineral can contain high amounts of Si (up to 9 %), which can also be incorporated in the mineral structure (Carlson and Schwertmann, 1981; Childs, 1992). Gehlen and Raaphorst (2002) reported amorphous Fe oxyhydroxides as the main sorbing phase on continental shelf sediments.

These observations indicate that ferrihydrite is an important soil constituent controlling the availability of Si in HTF soils. Silicic acid adsorption by goethite and lepidocrocite may also occur in the soils (Schwertmann and Taylor, 1972; Delstanche et al., 2009), but likely to a lesser extent than ferrihydrite due to their greater crystallinity and particle size (Cornell and Schwertmann, 2003). Interaction between Si and goethite and lepidocrocite in soils is poorly understood and needs further investigation. Based on soil morphological attributes, formation of redox concentrations is an active process in HTF soils (Vepraskas, 2001), which indicates that Fe oxyhydroxides are an important component controlling Si dynamics at HTFs. Thus, the periodical oxidation-reduction reactions within the soils lead to a rapid cycling of Fe through oxidized and reduces phases (Canfield et al., 1993), which likely control the Si adsorption-desorption and co-precipitation reactions in HTF soils.

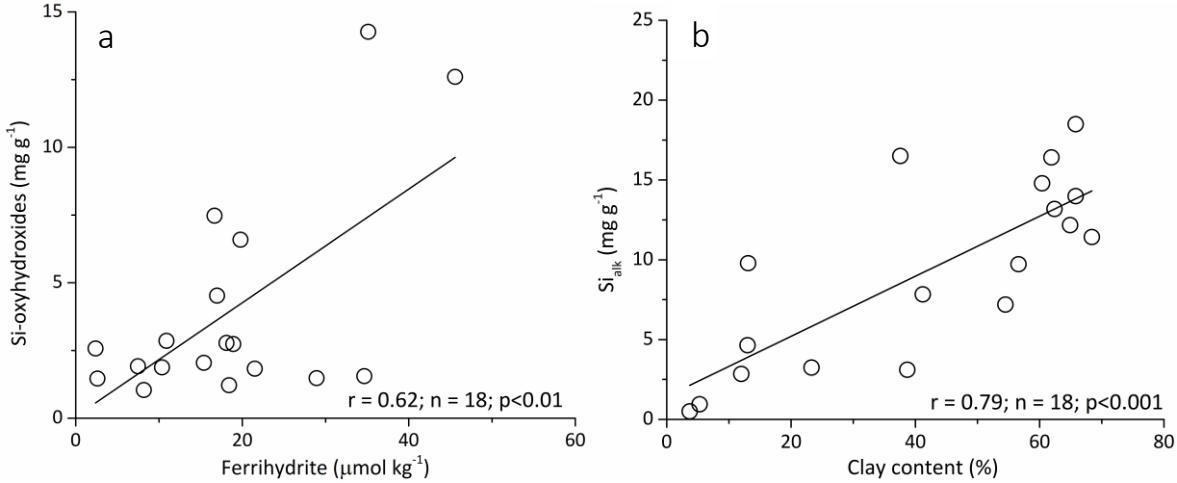

Fig. 6. Correlation between concentration of Si_{ox} and ferrihydrite (a) and clay content and Si_{alk} (b)

3.4.2. Origin and precipitation of amorphous Si

Si extracted by the alkaline extraction (NaOH, Si_{alk}) is the dominant Si fraction at both study sites (Fig. 2). This fraction consists of amorphous Si from biogenic and mineralogic sources, including biogenic opal (phytoliths, diatoms, radiolarians, and sponges) and pedogenic opal (e.g. opaline spheres and coatings; McKeague and Cline, 1963; Drees et al., 1989; Cornelis et al., 2011). Since HTF soils are formed under sedimentation processes (Albuquerque et al., 2014a), the contribution of different biogenic sources to Si_{alk} pool is expected. SEM images show diatoms, sponge spicules, and phytoliths in both soils (Fig. 5), which are largely produced in wetland soils (Clarke, 2003).

The absence or minimal amount of biogenic opal in the A (P1CE) and C2 (P1RJ) horizons, along with high Si_{alk} concentrations in all soil horizons, suggests that other mechanisms are involved in the formation of amorphous Si. Pedological opal can precipitate when soil conditions favor the increase of soluble Si levels (Drees et al., 1989; Saccone et al., 2007). Precipitation of amorphous Si in HTF soils is likely an active process driven by high effective evaporation rates at both sites during the dry season, which favor precipitation of pedogenic opal. To investigate this hypothesis, we modeled the soil extracts at two different soil depths of each soil profile (Table 2). Since soil pH values fall between 5.8 and 8.3, the main Si species in solution is H_4SiO_4. Activity of H_4SiO_4 (log a) is higher in HTF-RJ soils (approximately -2.9) than in HTF-CE soils (approximately -4.5), increasing to approximately -1.5 (HTF-RJ) and -3.2 (HTF-CE) after concentrating the soil solution twenty times. At HTF-RJ, H_4SiO_4 activity exceeds the solubility product for amorphous Si (log K = -2.74, Lindsay, 1979) after concentrating the solution, which indicates a pedological environment favorable for pedogenic opal

precipitation. The same does not occur for HTF-CE soils. Nevertheless, the increase of H_4SiO_4 activity in the concentrated solution and the high Si_{alk} concentration suggest that pedogenic opal may precipitate in HTF-CE soils, mainly in the surface horizons where the evapotranspiration is more effective (P1CE and P2CE horizons). A positive correlation between clay content and Si_{alk} ($r=0.79$, $n=18$, $p<0.01$, Fig. 6b) support this idea, indicating that amorphous Si is accumulating in the clay fraction (Georgiadis et al., 2014, 2017). This process is favored in soils under constant flooding events due to constant hydration of colloidal amorphous particles, which inhibits the formation of larger particles (Huang and Vogler, 1972) and favors Si concentration in microsites (Drees et al., 1989; Singh and Gilkes, 1993). In addition, spherical grains were found in the HTF-CE soils (Fig. 5i) and have been interpreted as being opaline sphere in other studies (Drees et al., 1989; Cornelis et al. 2011). Furthermore, pH values less than 9, high soil ionic strength, and available surface area within the soil fabric are factors that favor precipitation of amorphous Si in soils (Williams and Crerar, 1985; Drees et al., 1989).

Table 2. H_4SiO_4 activities in the soil extracts

Horizon	Modeling 1*	Modeling 2**
	Log *a*	
P1CE		
A	-4.8	-3.5
C3	-4.7	-3.4
P2CE		
A	-5.0	-3.7
C2	-4.3	-3.0
P3CE		
A	-4.9	-3.6
C1	-4.7	-3.4
P1RJ		
A	-3.1	-1.8
C2	-2.8	-1.5
P2RJ		
A	-3.3	-2.0
C1	-3.0	-1.6
P3RJ		
A	-3.1	-1.8
C1	-2.8	-1.5

*Values modeled using the saturated paste

** Values modeled after concentrating the saturated paste 20 times.

We believe that the predominance of mixed-layered minerals of low crystallinity (Table 1) also accounts for the high Si_{alk} concentration in the soils. HTF soils consist predominantly of mixed-layered minerals containing smectite layers (Table 1), indicating presence of clays with

disorder in the mixed-layered structure (Meunier, 2006). These minerals frequently exhibit crystal defects, which prevent their growth and favor formation of smaller crystals (Meunier, 2006). This disorder is shown by the low number of layers in the coherent scattering domain of the minerals (low N_{med} and N_{max} values), mainly for those with higher smectite layer proportion (K-S) and smectite end-member (S). Taking this into account, along with that alkaline extraction removes Si from silica minerals (Sauer et al., 2006), our data suggest that the Si_{alk} fraction comes partially from the soil clay fraction and not only from pedogenic opal. Furthermore, clay mineral alteration/formation also controls Si distribution in HTF soils due to the incorporation of Si from the soil solution during mineral neoformation and transformation processes (Sommer et al., 2006; Cornelis et al., 2014; Andrade et al. 2018). Since HTF soils have conditions that favor the formation of 2:1 minerals, uptake of Si during mineral reactions is highly expected in these soils (Humphries et al., 2011; Andrade et al., 2018), which explains in part the low H_4SiO_4 activity in these soils. Thus, reactions involving the clay fraction may impart a great control on Si dynamics in HTF soils as well.

3.4.3. Si dynamics in HTF soils

Our data indicate that Si_{ox}, $Si_{alk,}$ and clay minerals are three important factors controlling the distribution of Si in HTF soils; however, detailed reactions and interactions involving release, adsorption, precipitation and occlusion of Si mediated by these three soil components are complex and are not well understood. Soil environmental conditions are very dynamic in HTFs, changing the soil physicochemical parameters periodically throughout the month depending on tidal and weather conditions. As a result, these conditions increase the complexity and difficulty in understanding chemical reactions involving Si in these ecosystems. For example, periodic flooding and alternating redox conditions lead to formation of redox concentrations, which favor adsorption and co-precipitation of Si with Fe oxyhydroxides under oxic conditions (Georgiadis et al., 2017). On the other hand, the release of Si during dissolution of Fe oxyhydroxides when soils are sub-oxic can promote precipitation of Si_{alk} due to an increase of H_4SiO_4 concentration in the soil solution (Saccone et al., 2007). Furthermore, amorphous Si can also act as a source of Si for the formation of clay minerals in HTF soils, given that Si_{alk} is the predominant fraction of the readily soluble Si pool. Neoformation of 2:1 clay minerals can be mediated by Si-rich amorphous material in saline environments, even under relatively low Si concentration (Furquim et al., 2010a). Biogenic

opal also plays a direct role in the authigenesis of smectites due to clay neoformation at the expanse of the opaline material (Badaut and Risacher, 1983). In HTF soils, cycling and uptake of Si by plants is likely negligible due to the lack of vegetation, and therefore the control of Si by the soil components previously discussed outweigh those expected from plants. In sum, our set of observations and findings indicate Si tends to accumulate in HTF soils, and these ecosystems can represent an important sink of Si in coastal wetlands.

3.5. Conclusion

Different Si fractions in two hypersaline tidal flat soils on the Brazilian coast were investigated for the first time. The data show that Si associated with Fe oxyhydroxides and amorphous silicates are the main components of the readily soluble Si pool in these ecosystems. Pedogenic processes, tidal dynamics, and evaporative concentration of the waters create soil conditions that promote the control of Si in HTF soils. Formation of redox concentrations leads to Si adsorption and co-precipitation of with Fe oxyhydroxides. Ferrihydrite is likely the most reactive soil component contributing to the removal of Si from soil solution. Our findings also show that the amorphous silicate fraction is the dominant fraction at both study sites. This fraction consists mainly of phytoliths, diatoms, sponge spicules, and pedogenic opal. Precipitation of pedogenic opal is more prevalent in the uppermost horizons due to higher evaporation rates. The hypersaline environment and redox processes lead to the formation of mixed-layered minerals, which can partially control Si dynamics by adsorption processes or incorporation into clay structures during mineral neoformation and transformation. Our findings show that the source-sink of Si in HTF soils is controlled by multiple reactions involving release, adsorption, and co-precipitation of Si by different soils components.

References

Albuquerque, A.G.B.M., Ferreira, T.O., Cabral, R.L., Nóbrega, G.N., Romero, R.E., Meireles, A.J.A., Otero, X.L., 2014a. Hypersaline tidal flats (*apicum* ecosystems): the weak link in the tropical wetlands chain. Environ. Rev. 22, 1-11.

Albuquerque, A.G.B.M., Ferreira, T.O., Nóbrega, G.N., Romero, R.E., Souza Júnior, V.S., Meireles, A.J.A., Otero, X.L., 2014b. Soil genesis on hypersaline tidal flats (*HTF* ecosystem) in a tropical semi-arid estuary (Ceará, Brazil). Soil Res. 52, 140-154.

Andrade, G.R.P., Azevedo, A.C., Cuadros, J., Souza, Jr., V.S., Furquim, S.A.C., Kiyohara, P.K., Vidal-Torrado, P., 2014. Transformation of kaolinite into smectite and iron-illite in Brazilian mangrove soils. Soil Sci. Soc. Am. J. 78, 655-672.

Badaut, D., Risacher, F., 1983. Authigenic smectite on diatom frustules in Bolivian saline lakes. Geochim. Cosmochim. Ac. 47, 363-375

Borreli, N., Alvarez, M.F., Osterrieth, M.L., Marcovecchio, J.E., 2010. Silica content in soil solution and its relation with phytolith weathering and silica biogeochemical cycle in Typical Argiudolls of the Pampean Plain, Argentina - a preliminary study. J. Soils Sediments 10, 983-994

Canfield, D.E., Thamdrup, B., Hansen, J.W., 1993. The anaerobic degradation of organic matter in Danish coastal sediments: iron reduction, manganese reduction, and sulfate reduction. Geochim. Cosmochim. Ac. 57, 3867-3883.

Carlson, L., Schwertmann, U., 1981. Natural ferrihydrites in surface deposits from Finland and their association with silica. Geochim Cosmochim Ac. 45, 421-429.

Childs, C.W., 1992. Ferrihydrite: A review of structure, properties and occurrence in relation to soils. Z. Pflanzenernahr. Bodenk. 155, 441-448.

Clarke, J, 2003. The occurrence and significance of biogenic opal in the regolith. Earth-Sci. Reviews 60, 175-194.

Conley, D.J., 2002. Terrestrial ecosystems and the global biogeochemical silica cycle. Global Biogeochem. Cy. 16, 1121-1129.

Cornelis, J.T., Dumon, M., Tolossa, A.R., Delvaux, B., Deckers, J., Van Ranst, E., 2014. The effect of pedological conditions on the sources and sinks of silicon in the Vertic Planosols in south-western Ethiopia. Catena 112, 131-138.

Cornelis, J.T., Titeux, H., Ranger, J., Delvaux, B., 2011. Identification and distribution of the readily soluble silicon pool in a temperate forest soil below three distinct tree species. Plant Soil 342, 369-378.
Cornell, R.M., Schwertmann, U., 2003. The Iron Oxides second ed. Wiley-VCH Verlag GmbH and Co. KGaA, Weinheim.

Delstanche, S., Opfergelt, S., Cardinal, D., Elsass, F., André, L., Delvaux, B., 2009. Silicon isotopic fractionation during adsorption of aqueous monosilicic acid onto iron oxide. Geochim. Cosmochim. Ac. 73, 923-934.

Derry, L.A., Kurtz, A.C., Ziegler, K., Chadwick, O.A., 2005. Biological control of terrestrial silica cycling and export fluxes to watersheds. Nature 433, 728-731.

Dove, P.M., Crerar, D.,A., 1990. Kinetics of quartz dissolution in electrolyte solutions using a hydrothermal mixed flow reactor. Geochim. Cosmochim. Ac. 54, 955-969.

Drees, L.R., Wilding, L.P., Smeck, N.E., Sankayi, A.L., 1989. Silica in soils: quartz and disordered silica polymorphs, in: Dixon, J.B., Weed, S.B., (eds), Minerals in soil environments. Soil Science Society of America Book Series No. 1, Madison, p. 913-974.

Ferreira, T.O., Nóbrega, G.N., Albuquerque, A.G.B.M., Sartor, L.R., Gomes, I.S., Artur, A.G., Otero, X.L., 2015. Pyrite as a proxy for the identification of former coastal lagoons in semiarid NE Brazil. Geo-Mar. Lett. 35, 355-366.

Fortin, D., Leppard, G.G., Tessier, A., 1993. Characteristics of lacustrine diagenetic iron oxyhydroxides. Geochim. Cosmochim. Ac. 57, 4391-4404.

Furquim, S.A.C., Barbiéro, L., Graham, R.C., Queiroz-neto, J.P., Ferreira, R.P.D., Furian, S., 2010a. Neoformation of micas in soils surrounding an alkaline-saline lake of Pantanal wetland, Brazil. Geoderma 158, 331-342.

Furquim, S.A.C., Graham, R.C., Barbiéro, L., Queiroz-neto, J.P., Vidal-Torrado, P., 2010b. Soil mineral genesis and distribution in a saline lake landscape of the Pantanal Wetland, Brazil. Geoderma 154, 518-528.

Gehlen, M., Van Raaphorst, W., 2002. The role of adsorption - desorption surface reactions in controlling $Si(OH)_4$ concentrations and enhancing $Si(OH)_4$ turn-over in shallow shelf seas. Cont. Shelf Res. 22, 1529-1547.

Georgiadis, A., Rinklebe, J., Straubinger, M., Rennert, T., 2017. Silicon fractionation in Mollic Fluvisols along the Central Elbe River, Germany. Catena 153, 100-105.

Georgiadis, A., Sauer, D., Herrmann, L., Breuer, J., Zarei, M., Stahr, K., 2013. Development of a method for sequential Si extraction from soils. Geoderma 209-210, 251-261.

Huang, W.H., Vogler., D.L., 1972. Dissolution of opal in water and its water contents. Nature 235, 157-158.

Huerta-Díaz, M.A., Morse, J.W., 1990. A quantitative method for determination of trace-metal concentrations in sedimentary pyrite. Mar. Chem. 29, 119-144.
Humphries, M.S., Kindness, A., Ellery, W.N., Hughes, J.C., 2011. Water chemistry and effect of evapotranspiration on chemical sedimentation on the Mkuze River floodplain, South Africa. J. Arid Environ. 75, 555-565.

Iler, R.K., 1979. The chemistry of silica. Wiley, New York.
Jackson, M.L., 1979. Soil chemical analysis: advanced course. Madison: By author.

Lindsay, W., L., 1979. Chemical Equilibria in Soils. Wiley Interscience, New York.

Loucaides, S., van Cappellen, P., Behrends, T., 2008. Dissolution of biogenic silica from land to ocean: Role of salinity and pH. Limnol. Oceanogr. 53, 1614-1621.

Madella, M., Power-Jones, A.H., Jones, M.K., 1998. A simple method of extraction of opal phytoliths from sediments using a non-toxic heavy liquid. J. Archaeol. Sci. 25, 801-803.

McKeague, J.A., Cline, M.G., 1963. Silica in soil solutions. I. The form and concentration of dissolved silica in aqueous extracts of some soils. Adv. Agronomy 15, 339-396.

Mehra, O.P., Jackson, M.L., 1960. Iron oxide removal from soils and clay by dithionite-citrate system buffered with soil bicarbonate. Clay Clay Miner. 7, 317-327.

Meunier, A., 2006. Why are clay minerals small? Clay Miner. 41, 551-566.

Meunier, J.D., Colin, F., Alarcon, C., 1999. Biogenic silica storage in soils. Geology 27, 835-838.

Monger, H.C., Kelly, E.F., 2002. Silica Minerals, in: Dixon, J.B., Schulze, D.G., Soil mineralogy with environmental applications. SSSA Book Series 7, Madison, p. 611-632.

Otero, X.L., Ferreira, T.O., Huerta-Díaz, M.A., Partiti, C.S.M., Souza Jr., V., Vidal-Torrado, P., Macías, F., 2009. Geochemistry of iron and manganese in soil and sediments of a mangrove system, Island Pai Matos (Cananeia – SP, Brazil). Geoderma 148, 318-335.

Otero, X.L., Macías, F., 2002. Variation with depth and season in metal sulfides in salt marsh soils. Biogeochemistry 61, 247-268.

Parkhurst, D.L., 1995. Users guide to PHREEQC. A computer program for speciation, reaction-path, advective transport, and inverse geochemical calculations. US Geological Survey Water-Resources Investigations Reports, 95-4227.

Parkhurst, D., Christenson, S., Breit, G.N., 1996. Ground-Water-Quality Assessment of the Central Oklahoma Aquifer, Oklahoma Geochemical and Geohydrologic Investigations. U.S. Geological Survey water supply paper; 2357-C. United States government printing office, Washington.

Pokrovski, G.S., Schott, J., Farges, F., Hazemann, J.L., 2003. Iron (III)-silica interactions in aqueous solution: Insights from X-ray absorption fine structure spectroscopy. Geochim. Cosmochim. Ac. 67, 3559-3573.
Reynolds Jr., R.C., Reynolds III., R.C., 1996. NEWMOD for Windows. The Calculation of One-Dimensional X-ray Diffraction Patterns of Mixed-layered Clay Minerals, Hanover, New Hampshire.

Saccone, L., Conley, D. J., Koning, E., Sauer, D., Sommer, M., Daczorek, D., Blecker, S. W., Kelly, E.F., 2007. Assessing the extraction and quantification of amorphous silica in soils of forest and grassland ecosystems. Eur. J. Soil Sci., 58, 1446–1459.

Sauer, D., Saccone, L., Conley, D.J., 2006. Review of methodologies for extracting plant-available and amorphous Si from soils and aquatic sediments. Biogeochemistry 80, 89-108.

Schaefer, M.V., Guo, X., Gan, Y., Benner, S.G., Griffin, A.M., Gorski, C.A., Wang, Y., Fendorf, S., 2017. Redox controls on arsenic enrichment and release from aquifer sediments in central Yangtze River Basin. Geochim. Cosmochim. Ac. 204, 104-119.

Schwertmann, U., Taylor, R.M., 1972. The influence of silicate on the transformation of lepidocrocite to goethite. Clay Clay Miner., 20, 159-164.

Sommer, M., Kaczorek, D., Kuzyakov, Y., Breuer, J., 2006. Silicon pools and fluxes in soils and landscapes – a review. J. Plant Nutr. Soil Sci. 169, 310-329.

Struyf, E., Conley, D.J., 2009. Silica: an essential nutrient in wetland biogeochemistry. Front. Ecol. Environ. 7, 88-94.

Struyf, E., Conley, D.J., 2012. Emerging understanding of the ecosystem silica filter. Biogeochemistry 107, 9-18.

Swedlund, P.J., Webster, J.G., 1999. Adsorption and polymerization of silicic acid on ferrihydrite, and its effect on arsenic adsorption. Wat. Res. 33, 3413-1422.

Tessier, A., Campbell, P.G.C., Bisson, M., 1979. Sequential extraction procedure for the speciation of particulate trace metals. Anal. Chem. 51, 844-851.

Tréguer, P., Nelson, D.M., van Bennekom, A.J., De Master, D.J., Leynaert, A., Quéguiner, B., 1995. The silica balance in the world ocean: a reestimate. Science 268, 375-379.

Vepraskas, M.J., 2001. Morphological features of seasonally reduced soils, in: Richardson, J.L., Vepraskas, M.J. (Eds.), Wetland soils. Boca Raton, Florida, p. 163-182.

Williams, L.A., Crerar, A.D., 1985. Silica diagenesis, II. General mechanisms. J. Sediment. Petrol. 55, 312-321.

4. AUTHIGENESIS AND CHARACTERIZATION OF CLAY MINERALS IN HYPERSALINE TIDAL FLAT SOILS

Abstract

Tidal dynamics and evaporative concentration of the waters make the hypersaline tidal flat (HTF) soils a peculiar environment for multiple clay reactions and formation of a complex clay assemblage. Our data indicate that the soils have a geochemical environment conducive to mineral reactions and therefore clay mineral alterations. The crystal-chemical characteristics of clay minerals from two HTFs were studied here to give insights into the clay origin and formation in HTF soils. The fine (< 0.2 μm) and coarse (2-0.2 μm) clay fractions were investigated by XRD modeling, XRF, FTIR, and TEM-EDS analysis. The results indicate the presence of endmembers and R0 mixed-layered minerals, such as kaolinite, smectite, illite, kaolinite-smectite (K-S), kaolinite-illite (K-I), illite-smectite (I-S), illite-vermiculite (I-V), and smectite-vermiculite (S-V). In general, K-S is the dominant mineral in the samples and occur in a range of kaolinite layers, mainly in the finer fraction. A transformation of detrital kaolinite into Mg-rich trioctahedral smectite seems to be taking place via mixed-layering in the soils. There is an enrichment in Mg at the expanse of Al in the samples and bio-opal seems to be the source of Si for the transformation process. Although HTF soils have propitious conditions for kaolinite illitization, we cannot determine if the Fe-illite in these soils are inherited from the previous mangrove soils or is a product of the kaolinite illitization. Clay authigenesis is an important factor controlling Si dynamics in HTF soil, acting as a sink of Si as the formation of new clay phases proceeds in the soil.

Keywords: Mixed-layered minerals; Transformation; Interstratified minerals; Clay alteration; Kaolinite-smectite; Biogenic opal

4.1. Introduction

Hypersaline tidal flat (HTF) soils are very dynamic systems of coastal wetlands, positioned at the continental-marine interface and formed primarily by sedimentary processes (Albuquerque et al., 2014a). They are distributed on the north, northeast, and southeast coasts of Brazil and are also widely represented on a global scale (Albuquerque et al., 2014a).

Tidal hydrodynamics, redox processes, and evaporative concentration of waters are major factors controlling pedogenesis in HTF soils (Albuquerque et al., 2014a, 2014b). These ecosystems are flooded many days throughout the month, and the soils undergo periodic wetting-drying cycles. The pedogenic processes governing these soils are similar to those commonly found in soils of poorly drained and evaporative environments, such as redoximorphism, (hyper)salinization, and solodization. The interplay of these processes may

promote multiple mineral reactions and the formation of clay minerals with high chemical and structural variability (Hover et al. 1999; Furquim et al., 2010; Andrade et al., 2014). Therefore, authigenesis of clay minerals by neoformation and transformation are expected to take place in these environments (Darragi and Trady, 1987; Mayayo et al., 2000; Cuevas et al., 2003; Furquim et al., 2008).

HTF soils have pH values between 6 and 8, salt concentration up to five times the normal sea water, and solute concentration controlled primarily by seawater evaporation. The latter gives rise to soil solutions highly concentrated in Mg^{2+}, Ca^{2+}, K^{+}, Na^{+}, SO_4^{2-}, and Cl^{-}. These factors govern clay formation in these evaporative environments (Gac et al., 1977; Bouza et al., 2007; Ryan and Huertas, 2013). Since HTFs have been formed by sedimentation processes, the detrital input and the nature of the sediments play an import role in the mineral reactions as well (Darragi and Tardy, 1897). The soil solid phase can provide elements to mineral reactions or act as a substrate for crystalline growth of clay minerals (Badaut and Risacher, 1983; Furquim et al., 2010; Barbiero et al., 2016).

Studies of clay authigenesis also have environmental implications and can be extended to understand oceanic and terrestrial biogeochemical cycles (Gac et al., 1977; Presti and Michalopoulos, 2008; Cuadros et al., 2017). Since HTFs are closely associated with stuaries, they may exert control on the biogeochemical cicles in coastal wetlands. Silicon, for example, is an essential nutrient for most living organisms in marine and estuarine ecosystems (Conley 2002; Sommer et al., 2006), and the sink and release of Si is strongly mediated by clay mineral reactions (Gac et al., 1977; Dixit et al., 2001; Presti and Michalopoulos, 2008). Studies concerning the characteristics, distribution, and geochemistry of clay minerals in wetland soils on the Brazilian coast have been well described for mangroves (Souza-Júnior et al., 2008; Andrade et al., 2014; Cuadros et al. 2017), but no detailed studies are available for HTF soils. This study aims to characterize the clay fraction of two HTF soils on the Brazilian coast and discusses possible mechanisms of clay formation and their effects on Si dynamics.

4.2. Materials and methods

Three soil profiles were sampled at each site during low tide. Soil profiles were labeled as P1CE and P2CE (HTF on the NE coast, HTF-CE), and P1RJ and P2RJ (HTF on the SE coast, HTF-RJ). Three soil horizons were sampled from two soil pits at each site: i) surface horizons (A horizons of P1CE, P2CE, P1RJ, and P2RJ), ii) intermediary horizons (C3 of P1CE, C2 of P2CE,

C2 of P1RJ, and C1 of P2RJ), and iii) deeper horizons (C4 of P1CE, C3 of P2CE, C3 of P1RJ, and C3 of P2RJ). The collected samples were maintained at 4° C during transportation to the laboratory and were air dried before the analysis.

For mineralogical analysis, organic matter was removed with 30 % (v/v) H_2O_2, and a dithionite-citrate-bicarbonate solution was used for removal of pedogenic Fe oxyhydroxides (Mehra and Jackson, 1960). The sand fraction was separated by wet sieving after dispersion of the suspension using 0.01 mg L^{-1} Na_2CO_3. The suspensions containing silt and clay were separated by sedimentation, and the clay fraction was collected. Fine (<0.2 µm) and coarse (2.0 - 0.2 µm) clay fractions were separated by centrifuging the samples several times at 4,100 rpm for 20 min. The samples were saturated with $MgCl_2$ 1 mol L^{-1}. The Mg-saturated samples were analyzed as air-dried specimens after i) ethylene glycol (EG) solvation, and ii) heating them at 550 C°. EG solvation was achieved by exposing the samples to the reagent at 60 °C for 20 h. Oriented aggregate specimens of fine and coarse clay were prepared on glass slides for X-ray diffraction (XRD) and were scanned from 3 to 30 °2θ, with 0.02 °2θ step size and count time of 3 s/step, using a *Rigaku Miniflex II* (CuKα radiation). Thermal treatment confirmed the absence of chlorite in the samples and the presence of gibbsite in the HTF-RJ soils (not shown). Identification and quantification of the clay phases were performed using the software Newmod 3.2.1 (Reynolds and Reynolds, 1996). The input variables for the modeling include all the important structural data and settings that describe the optical configuration of the diffractometer used. The main parameters are: amount of each clay phase (%), proportion of each component in the mixed-layered phase (% of kaolinite, smectite, illite, and vermiculite), octahedral Fe content (on the $O_{10}[OH_2]$ basis for 2:1 layers and $O_5[OH]_4$ basis for 1:1 layers), maximum (Nmax) and average (Nave) number of layers in the coherent scattering domain, amount of K in illite (on the $O_{10}[OH_2]$ basis), stacking ordering of layers (R parameter), and orientation factor (σ*, set as 12 for all samples, which means the most realistic particle orientation). The XRD patterns were calculated without a 2θ slit compensator and Mg^{2+} was assumed as the interlayer cation. For the 06,33 peaks, a slower scanning procedure was applied (59 to 64 °2θ, with 0.02 °2θ step size and count time of 35 s/step) in order to maximize the intensity:background ratios and achieve a better peak resolution.

Chemical elemental analysis of individual particles was performed by transmission electron microscopy using an *FEI Titan Themis 300* instrument equipped with a super-X

energy dispersive X-ray spectrometer system (TEM-EDS). The specimens were prepared by deposition of the clay suspension on 200 mesh Cu support grid covered with carbon support film. The chemical composition of one to four particles was determined to support the XRD modeling.

Major elements in the < 0.2 µm and 2.0 - 0.2 µm fractions were determined by X-ray fluorescence (XRF) using an ED-XRF (*Spectro Xepos HE).* Between 2.0 and 5.0 g of ground clay sample free from Fe oxyhydroxides and organic matter was placed in a plastic cup fitted with a thin layer of polypropylene film (Chemplex). The measurements were performed in a He atmosphere to minimize X-ray attenuation. Bulk elemental abundance was calculated based on the intensity of the characteristic fluorescent X- rays of each element. (Schaefer et al., 2017).

The < 0.2 µm and 2.0 - 0.2 µm fractions of the P1CE and P1RJ profiles were investigated by Fourier transform infrared spectroscopy (FTIR). The samples were scanned from 400 to 4,000 cm^{-1} and analyzed as KBr pellets (sample:KBr ratio of 0.5 mg/300 mg, pressed at 8 ton for 5 min), using a *Shimadzu IR Prestige-21.*

The saturation extracts were prepared from the fine earth using the two uppermost horizons of each soil profile (USDA, 2014). The soil extracts were obtained from the saturated paste by centrifugation at 5,000 rpm for 20 min and filtered through a 0.45 mm Millipore. The concentration of Si, Al, Fe, P, and S were determined by ICP-OES, using a *Thermo Scientific iCAP 6000 series* instrument. Sodium and K^+ were determined by flame photometry, and Ca and Mg by atomic absorption spectroscopy. The ion Cl^- was measured using a specific electrode (*Mettler Toledo PerfectIon Combination Chloride Electrode*). Alkalinity (HCO_3^-) was determined by titration with H_2SO_4. The pH and Eh values were measured in the field using a glass electrode and an oxidation-reduction potential Pt electrode, respectively. The Eh final readings were corrected by adding the potential of a calomel reference (244 mV).

4.3. Results

4.3.1. XRD study

XRD patterns indicate the existence of the phyllosilicates kaolinite, smectite, illite, vermiculite, and randomly mixed-layered minerals (R0 ordering) in all samples (Fig. 1 and Table 1). Kaolinite is the dominant mineral and was identified by the 0.72 and 0.36 nm peaks, which collapsed after heating the samples at 550 C^o. The diffraction peaks at approximately

1.0, 0.5, and 0.33 nm are related to illite, which were not affected by the thermal and EG solvation treatments. The 1.65-1.80 nm peak is due to the presence of smectite. Vermiculite and the mixed-layered phases were revealed after the XRD modeling.

The XRD modeling data revealed that the coarser fraction (2.0 - 0.2 μm) consists of mixed-layered kaolinite-smectite (K-S), kaolinite- illite (K-I), smectite-vermiculite (S-V), illite-smectite (I-S), and illite-vermiculite (I-V), and the end-members kaolinite, illite, and smectite. The end-members kaolinite and illite are present in all soil horizons. Kaolinite content varies from approximately 7 to 16 % and illite from 3 to 13 % at HTF-CE. At HTF-RJ, kaolinite content varies from approximately 17 to 21 % and illite from 11 to 17 %. These minerals have large coherently diffracting domain size (higher Nmax and Nave values, Table 1), being responsible for generating the more intense and sharper peaks in the XRD patterns.

In general, the samples contain two K-S minerals, with > 90% or 55 – 77 % of kaolinite layers (Table 1). Together, these two minerals comprise approximately 18 to 40 % of the minerals, with higher content in the surface horizons at HTF-CE. Although K-I is not commonly found in soils, a better fitting was achieved including one or two K-I phases during the XRD modeling. In general, the HTF-CE soils have one illite-rich K-I (more than 70 % of illite layers) and another kaolinite-rich K-I (between 50 and 65 % of kaolinite layers). On the other hand, only illite-rich K-I minerals were found in the HTF-RJ soils, with a minimum of 60 % of illite layers.

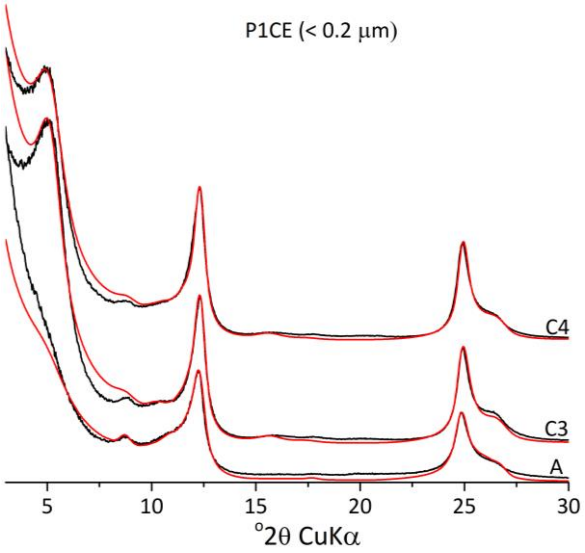
P1CE (< 0.2 μm)
C4
C3
A
5
10
15
20
25
30
°2θ CuKα

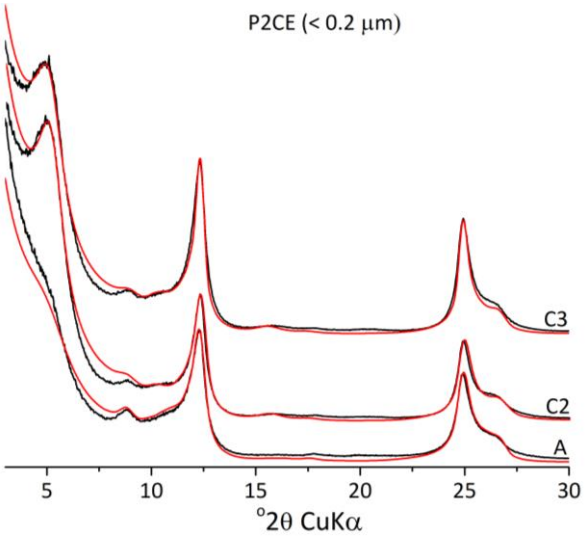
P2CE (< 0.2 μm)
C3
C2
A
5
10
15
20
25
30
°2θ CuKα

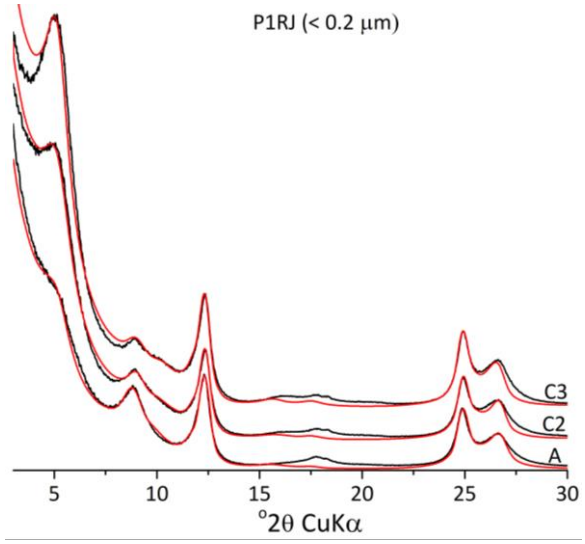
P1RJ (< 0.2 μm)
C3
C2
A
5
10
15
20
25
30
°2θ CuKα

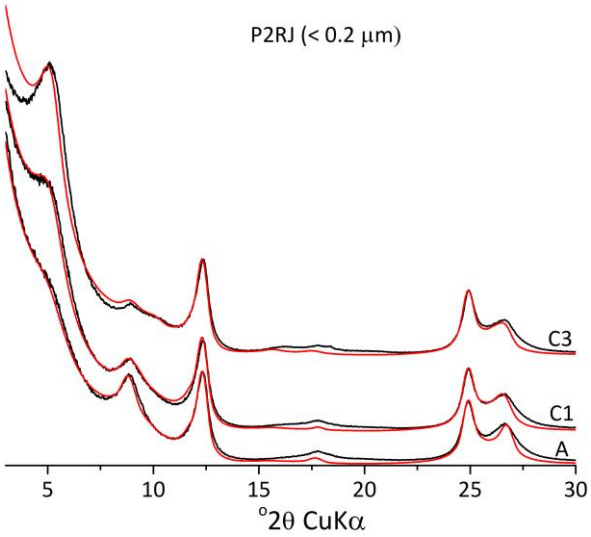
P2RJ (< 0.2 μm)
C3
C1
A
5
10
15
20
25
30
°2θ CuKα

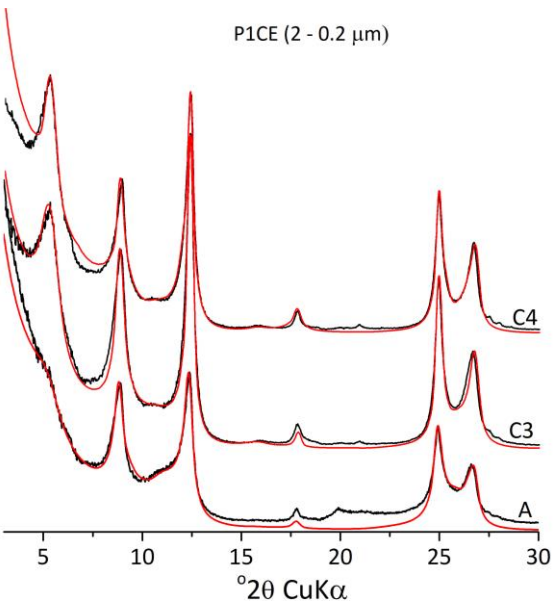
P1CE (2 - 0.2 μm)
C4
C3
A
5
10
15
20
25
30
°2θ CuKα

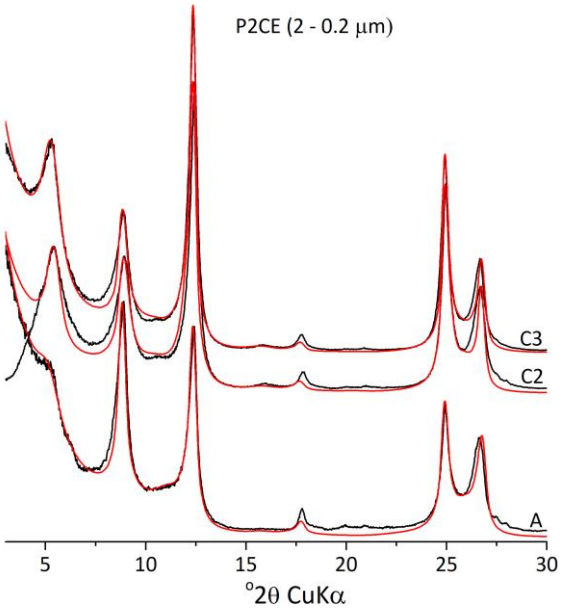
P2CE (2 - 0.2 μm)
C3
C2
A
5
10
15
20
25
30
°2θ CuKα

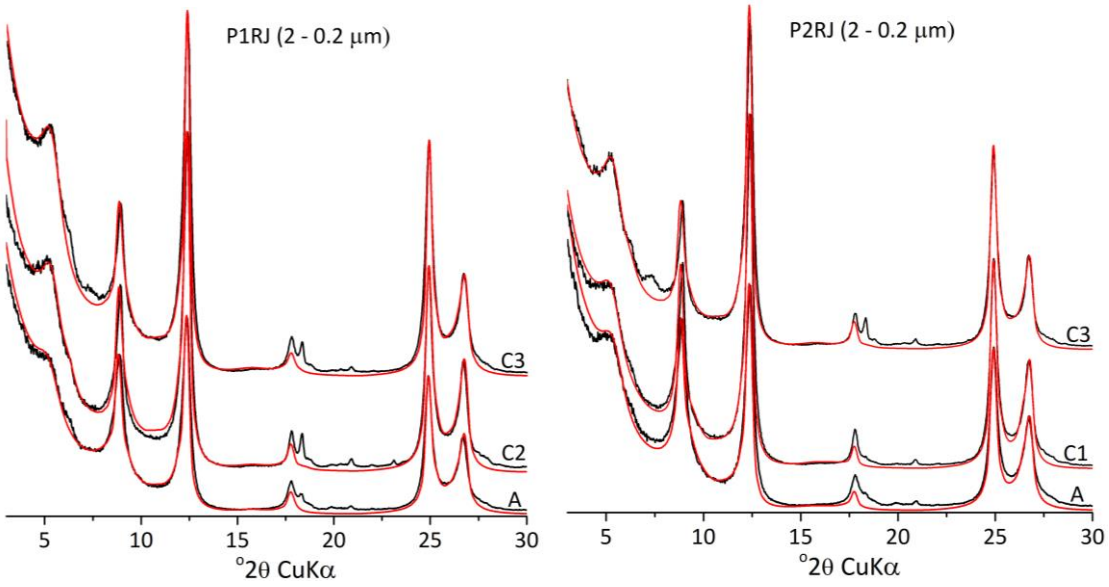

Fig. 1. Experimental (black line) and calculated (grey line) XRD patterns of oriented and glycolated samples

The < 0.2 μm fraction (fine clay) consists of the mixed-layered K-S, K-I, I-S, and I-V, and the end-members kaolinite, illite, and smectite. Even though the different clay fractions have similar composition, the proportion of each mineral differs substantially. In general, K-S is the dominant mixed-layered phase and is more abundant than in the coarser fraction. This mineral comprises approximately 47-86 % of the minerals in the HTF-CE soils, with higher contents in the surface horizons. By contrast, K-S makes up 37-54 % of the minerals at HTF-RJ, with higher values in the deeper horizons. The end-member kaolinite and the kaolinite-rich K-S (more than 85 % of kaolinite layers) are the dominant clay minerals in this fraction. Kaolinite end-member is present in all soil horizons at HTF-RJ, whereas it is present only in C3 of P1CE, and C2 and C4 of P2CE at HTF-CE. Smectite-rich K-S phases (63 – 90 % of smectite layers) and K-S phases containing 50-80 % of kaolinite layers are also present in the soils. These minerals have lower coherently diffracting domain sizes when compared to kaolinite and kaolinite-rich K-S.

The end-member illite is present in the surface horizon of the P1CE, P1RJ, and P2RJ profiles. At least one illite-rich I-S mineral (more than 70% of illite layers) is present in almost all soil horizons, with exception of the C1 horizon (P2RJ). Smectite-rich I-S minerals are also present in most samples at HTF-CE, with exception of the A horizon (P1CE). One K-I phase was detected in the HTF-CE soils, whereas two K-I phases were found at HTF-RJ. The end-member smectite is present in C3 and C4 (P1CE), C2 (P2CE), C3 (P2RJ), and C3 (P1RJ), with higher

content at HTF-RJ. This phase makes up approximately 5-14 % of the < 0.2 μm fraction at HTF-CE, and 15-18 % at HTF-RJ.

An interesting chemical characteristic is the Fe contents detected by XRD modeling, mainly in the < 0.2 mm fraction. The values for smectite and illite vary widely among the samples and even within each sample. In general, Fe contents vary from 0 to 1.0 for smectite and 0.6 to 0.8 for illite. HTF-CE and HTF-RJ soils show similar results, but the values are lower than those found in mangrove soils at the HTF-CE estuary (Andrade et al., 2018).

The analysis of 06,33 peaks reveals important information regarding the octahedral occupancy within the clay minerals (Fig. 2). Two peak maxima were detected in the XRD of the coarser clay fraction. The peak at 62.26 $^{o}2\theta$ corresponds to kaolinite, whereas the peak in between 60.46 and 60.02 $^{o}2\theta$ is related to a mixture of Fe^{2+}-rich trioctahedral sites of illite (Brindley and Brown, 1980). The distinct peak at 61.34 $^{o}2\theta$ for A and C2 horizons (HTF-RJ) is related to 2:1 dioctahedral sites. A broad region occurs around 60.90 $^{o}2\theta$ and can be attributed to diffraction of trioctahedral sites of smectite (Deocampo et al., 2009). The peak at 62.26 $^{o}2\theta$ in the finer clay fraction is due to kaolinite dioctahedral sites. The broad region at lower angles (around 61.80 $^{o}2\theta$) contains peaks related to dioctahedraland 2:1 and trioctahedral sites. The Fe^{2+} sites within illite structure are likely generating the peak at 1.53-1.54 nm for the A horizon (P1CE). These results are consistent with the chemical characterization presented below.

Table 1. Parameters from the XDR modeling of oriented and glycolated samples

phase	% layers	Fe kaol	Fe smec	Fe verm	Fe illite	K illite	Nmax/ Nave	% phase	phase	% phase	Fe kaol	Fe smec	Fe verm	Fe illite	K illite	Nmax/ Nave	% phase
				< 0.2 µm									2 – 0.2 µm				
P1CE																	
A horizon																	
K-S	99-1	<0.01	0.5	-	-	-	30/15	16.935	K	100	<0.01	-	-	-	-	44/30.8	7.04
K-S	95-5	<0.01	0.5	-	-	-	15/7	24.156	K-S	97-3	<0.01	1.5	-	-	-	35/6.8	21.616
K-S	80-20	<0.01	0.35	-	-	-	8/3.1	20.623	I-V	96-4	-	-	0.21	0.93	0.7	26/10.9	17.013
K-S	60-40	<0.01	0.35	-	-	-	8/3	17.091	K-I	24-76	<0.01	-	-	1.09	0.65	28/19.8	12.455
I-S	96-4	<0.01	0	-	0.5	0.75	16/10.9	6.39	I	100	-	-	-	1.19	0.75	25/20.8	3.61
K-I	44-56	<0.01	-	-	0.4	0.8	15/10	7.299	K-S	72-28	<0.01	0.46	-			10/3.2	18.547
I-S	70-30	-	0.21	-	0.1	0.8	15/7	3.87	K-I	60-40	<0.01	-	-	0	0.75	19/10	13.628
K-S	37-63	<0.00	0.32	-	-	-	7/3	3.636	S-V	89-11	-	0.62	0.25	-	-	7/1.2	6.092
C3 horizon																	
K	100	<0.01		-	-	-	30/19	12.86	K	100	<0.01	-	-	-	-	44/30.8	15.939
K-S	95-5	<0.01	0.64	-	-	-	23/14.8	16.422	K-S	96-4	<0.01	0.06	-	-	-	35/7.8	12.037
K-S	88-12	<0.01	0.76	-	-	-	18/3.1	17.09	I-V	94-6	-	-	0	0.9	0.7	36/24.8	18.289
K-S	16-84	0.04	0.69	-	-	-	9/1.8	13.843	K-I	22-78	0	-	-	0.82	0.7	27/17.9	12.059
I-S	91-9	-	0.5	-	0.46	0.8	11/4.9	10.354	I	100	-	-	-	1	0.7	25/20.8	8.668
K-I	79-21	<0.01	-	-	0.4	0.8	14/7	9.928	K-S	63-37	<0.01	0	-	-	-	9/4.5	8.557
I-S	5-95.	-	0.7	-	0.53	0.75	7/1.2	14.121	K-I	57-43	<0.01	-	-	0	0.75	16/8	10.109
S	100	-	0.87	-	-	-	6/1.2	5.381	S-V	84-16	-	0.52	0	-	-	8/1.9	14.343
C4 horizon																	
K-S	99-1	<0.01	0.5	-	-	-	35/20.2	12.628	K	100	<0.01	-	-	-	-	54/34	9.013
K-S	97-3	<0.01	0.64	-	-	-	26/14.8	15.184	K-S	95-5	<0.01	1.5	-	-	-	25/13.9	19.263
K-S	87-13	<0.01	0.76	-	-	-	13/3.5	15.045	I-V	84-16	-	-	0.4	0.67	0.8	14/9	8.332
K-S	30-70	<0.01	0.35	-	-	-	11/2.7	12.318	K-I	15-85	0	-	-	0.46	0.7	27/17.9	17.26
I-S	90-10	-	0.45	-	0.56	0.8	13/5.9	8.568	I	100		-	-	0.6	0.7	31/14.9	12.828
K-I	82-18	<0.01		-	0.4	0.75	16/6.8	13.356	K-S	51-49	<0.01	0	-	-	-	10/3.5	8.353
I-S	22-78	-	0.91	-	0.58	0.75	7/1.7	8.971	K-I	24-76	<0.01	-	-	0.25	0.75	18/10	10.569
S	100	-	0.71	-			5/1.1	13.929	S-V	84-16	-	0.86	0	-	-	10/6	14.383
P2CE																	
A horizon																	
K-S	99-1	<0.01	0.35	-	-	-	30/16	18.576	K	100	<0.01	-	-	-	-	44/30.8	11.446
K-S	93-7	<0.01	0.5	-	-	-	18/9.9	21.236	K-S	97-3	<0.01	0	-	-	-	35/6.8	16.299
K-S	86-14	<0.01	0.35	-	-	-	8/3.1	15.809	I-V	99-1	-	-	0	0.96	0.65	26/10.9	19.596
K-S	55-45	<0.01	0.35	-	-	-	8/3	17.01	K-I	20-80	<0.01	-	-	0.26	0.7	27/17.9	15.552
I-S	94-6	-	0.45	-	0.56	0.77	16/9.6	9.309	I	100	-	-	-	1.27	0.7	35/20.8	4.635
K-I	48-52	<0.01		-	0.4	0.8	17/12.9	9.588	K-S	67-33	<0.01	0	-	-	-	10/3.2	14.992
I-S	50-50	-	0.24	-	0.19	0.8	11/7	4.376	K-I	53-47	<0.01	-	-	0	0.7	19/10	11.198
K-S	50-50	<0.01	0.2				7/2.1	4.097	S-V	95-5	-	0.62	0	-	-	7/1.4	6.283
C2 horizon																	
K	100	<0.01	-	-	-	-	30/19	10.94	K	100	<0.01					50/41.6	13.39
K-S	95-5	<0.01	0.5	-	-	-	23/14.8	15.669	K-S	97-3	<0.01	0				43/16.8	9.005
K-S	78-22	<0.01	0.5	-	-	-	18/3.1	17.283	I-S	91-9		0		0.69	0.7	36/21.9	16.877

K-S	16-84	<0.01	0.69	-	-	-	9/1.8	13.999	K-I	20-80	<0.01			0.82	0.7	27/21.9	11.551
I-S	91-9	-	0.5	-	0.46	0.8	12/5.9	10.471	I	100				0.83	0.7	25/20.8	5.818
K-I	79-21	<0.01	-	-	0.4	0.8	14/7	10.039	K-S	94-6	<0.01	0			-	29/18.5	18.203
I-S	5.-95	-	0.7	-	0.53	0.75	7/1.2	14.28	K-I	58-42	<0.01			0.25	0.8	19/14	15.765
S	100	-	0.87	-	-	-	6/1.2	7.318	S-V	70-30	0		0			10/3.9	9.39
C3 horizon																	
K	100	<0.01		-	-	-	36/28.2	14.52	K	100	<0.01	-	-	-	-	50/41.6	15.731
K-S	94-6	<0.01	0.93	-	-	-	31/18.8	14.52	K-S	95-5	<0.01	0	-	-	-	43/16.8	15.101
K-S	90-10	<0.01	0.76	-	-	-	15/3.7	14.52	I-S	90-10	-	0	-	0.59	0.8	36/21.9	12.758
K-S	26-74	<0.01	0.35	-	-	-	9/1.8	11.21	K-I	24-76	<0.01	-	-	0.82	0.8	27/21.9	10.65
I-S	88-12	-	0.45	-	0.46	0.7	14/10.9	8.102	I	100	-	-	-	0.5	0.79	25/20.8	12.286
K-I	79-21	<0.01	-	-	0.4	0.6	14/7	14.52	K-S	92-8	<0.01	0	-	-	-	29/5.5	5.521
I-S	5.-95	-	0.6	-	0.53	0.7	7/1.2	13.242	K-I	65-35	<0.01	-	-	0.25	0.8	19/8	12.223
K-S	30-70	0	0.43	-			7/3.2	9.365	S-V	81-19	0	-	0	-	-	10/1.8	15.731
P2RJ																	
A horizon																	
K	100	<0.01	-	-	-	-	29/14.9	17.138	K	100	0	-	-	-	-	44/30.8	20.398
K-S	92-8	0	0	-	-	-	14/9.2	17.55	K-S	97-3	0	0		-	-	25/6.8	12.091
I	100	-	-	-	0.15	0.71	16/13.8	5.609	I-V	98-2	-	-	0	0.78	0.7	26/10.9	7.913
K-S	33-67	0	0.55	-	-	-	8/1.3	19.53	K-I	20-80	0	-	-	0.38	0.7	27/17.9	19.931
K-I	30-70	0	-	-	1.4	0.7	9/2.4	16.808	I	100	-	-	-	0.6	0.7	35/20.8	11.133
K-I	35-65	0	-	-	1.23	0.7	12/6	10.518	K-S	77-23	0	0	-	-	-	9/3.5	6.734
I-S	93-7	-	0.21	-	0.72	0.7	18/11	12.848	K-I	35-65	0	-	-	1.23	0.7	11/5.9	11.354
-	-	-	-	-	-	-	-	-	S-V	70-30	-	0.12	0	-	-	9/1.4	10.445
C1 horizon																	
K	100	<0.01	-	-	-	-	29/14.9	15.735	K	100	<0.01	-	-	-	-	47/30.8	20.101
K-S	96-4	<0.01	0.86	-	-	-	14/9.2	13.845	K-S	94-6	<0.01	0	-	-	-	25/13.9	15.939
I-V	94-6	-	-	0	0.55	0.71	23/13.8	6.093	I-V	98-2	-	-	0	1.01	0.7	26/11.9	9.697
K-S	26-74	<0.01	1.34	-	-	-	8/1.1	18.878	K-I	25-75	0	-	-	0.33	0.7	27/17.9	16
K-S	14-86	<0.01	1.05	-	-	-	8/1.4	11.627	I	100	-	-	-	0.35	0.7	31/20.8	13.03
K-I	29-71	<0.01	-	-	0.62	0.7	15/6	10.991	K-S	60-40	<0.01	0	-	-	-	8/3.5	7.434
K-I	21-79	<0.01	-	-	1.2	0.7	15/11	13.016	I-S	68-32	-	0	-	0.95	0.7	17/10	8.869
K-S	73-27	<0.01	0	-	-	0.77	19/4.7	9.815	S-V	82-18	-	0.19	0	-	-	10/.1.4	8.929
C3 horizon																	
K	100	<0.01		-	-	-	29/14.9	15.671	K	100	<0.01	-	-	-	-	47/30.8	19.366
K-S	98-2	<0.01	0.97	-	-	-	15/8.2	13.938	K-S	94-6	<0.01	0	-	-	-	25/13.9	15.356
S	100		0.94	-	-	-	9/1.4	18.054	I-V	12.-88	-	-	0.4	0.69	0.7	14/9	1.187
K-S	36-64	<0.01	1.26	-	-	-	8/1.1	18.054	K-I	15-85	0	-	-	0.33	0.82	27/17.9	19.463
K-I	36-64	<0.01		-	0.28	0.74	17/11.9	16.971	I	100	-	-	-	0.23	0.77	31/28.9	17.049
I-S	90-10	-	0	-	0.29	0.7	17/10.9	10.814	K-S	55-45	<0.01	0	-			8/5.5	7.162
K-S	72-28	0	0	-	-	-	15/8.9	6.499	K-I	40-60	0		-	0.35	0.77	11/7	10.237
-	-	-	-	-	-	-	-	-	S-V	75-25	-	0.19	0			11./1.7	10.179
P1RJ																	
A horizon																	
K	100	<0.01	-	-	-	-	26/14.9	18.404	K	100	0	-	-	-	-	47/30.8	17.624

K-S	93-7	<0.01	0	-	-	-	13/7.2	13.369	K-S	93-7	<0.01	0		-	-	25/13.9	13.9
I	100	-	-	-	1.31	0.7	11/7.1	6.418	I-V	81-19	-	-	0.25	0.88	0.7	24/11	9.275
K-S	7.-93	<0.01	0.55	-	-	-	8/1.1	19.747	K-I	18-82	0	-	-	0.33	0.7	27/17.9	15.482
K-I	45-55	<0.01	-	-	0.93	0.74	10/3.4	15.936	I	100	-	-	-	0.46	0.7	30/23.9	15.701
K-I	37-63	0	-	-	1.08	0.79	12/6	15.995	K-S	59-41	<0.01	0	-	-	-	8/4.5	8.958
I-S	91-9	<0.01	-	-	1.08	0.7	16/9.7	10.13	K-I	40-60	0	-	-	0.65	0.7	7/4	12.171
-	-	-	-	-	-	-	-	-	S-V	85-15	-	0.19	0	-	-	7/1.4	6.889
C2 horizon																	
K	100	<0.01		-	-	-	29/14.9	14.397	K	100	<0.01	-	-	-	-	47/30.8	20.742
K-S	96-4	<0.01	0.86	-	-	-	14/9.2	13.052	K-S	94-6	<0.01	0	-	-	-	25/13.9	16.448
I-S	89-11		0.9	-	0.41	0.71	23/12.8	12.016	I-V	12.-88	-	-	0.4	0.69	0.7	14/9	1.272
K-S	21-79	<0.01	1.34	-	-	-	8/1	14.125	K-I	15-85	0	-	-	0.33	0.82	27/17.9	20.846
K-S	10.-90	<0.01	1.12	-	-	-	8/1.4	18.179	I	100	-	-	-	0.38	0.77	31/28.9	14.509
I-S	50-50	-	0	-	0.62	0.7	15/6	4.781	K-S	55-45	<0.01	0	-			8/5.5	7.671
K-I	20-80	<0.01	-	-	1.01	0.7	13/6	7.817	K-I	40-60	0		-	0.35	0.77	11/7	10.965
K-I	63-37	0	-	-	0.37	0.77	19/4.7	15.634	S-V	75-25	-	0.19	0			11/1.7	7.546
C3 horizon																	
K	100	<0.01		-	-	-	29/14.9	13.589	K	100	<0.01	-	-	-	-	54/34	17.265
K-S	96-4	<0.01	0.97	-	-	-	15/8.2	15.477	K-S	95.5	0	0	-	-	-	25/13.9	17.599
S	100		0.94	-	-	-	9/1.4	15.477	I-V	84-16	-	-	0.4	0.67	0.7	14/9	6.177
K-S	31-69	<0.01	1.26	-	-	-	8/1.1	15.477	K-I	15-85	0	-	-	0.33	0.7	27/17.9	17.599
K-S	27-73	0	0.95				11/2	9.967	I	100	-	-	-	0.52	0.8	31/28.9	12.02
K-I	26-74	<0.01		-	0.28	0.74	17/11.9	15.168	K-S	55-45	<0.01	0	-	-	-	9/5.5	7.867
I-S	90-10	-	0	-	0.29	0.7	17/10.9	9.271	K-I	40-60	0	-	-	0.35	0.7	13/7	9.257
K-S	72-28	0	0	-	-	-	15/8.9	5.572	S-V	74-26	-	0.19	0	-	-	9/1.5	12.214

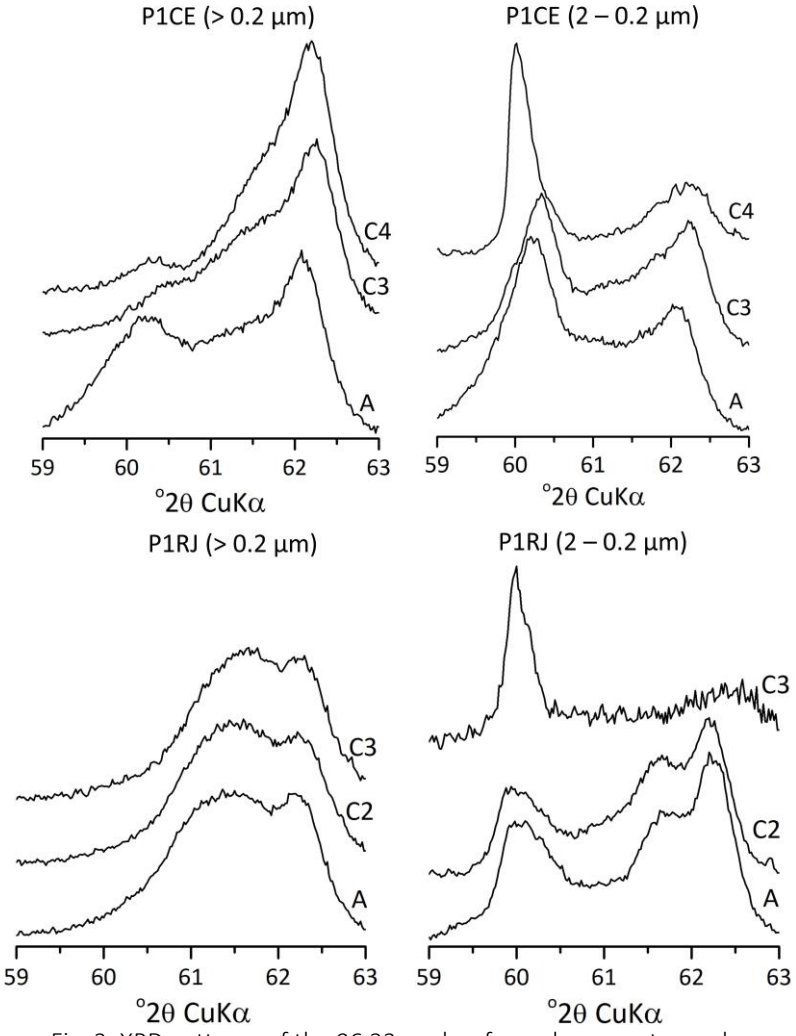

Fig. 2. XRD patterns of the 06,33 peaks of powder mount samples

4.3.2. Major chemical composition

XRF analysis of major elements for the > 0.2 µm and 2-0.2 µm clay fractions revealed the dominance of SiO_2 and MgO in the A horizon of the P1CE soil profile, and SiO_2 and Al_2O_3 in the other samples (Table 2). The amount of MgO in the surface horizons at HTF-RJ is slightly higher than in the deeper horizons, but its distribution is more homogeneous throughout the soil profiles when compared to those at HTF-CE. High amounts of Fe_2O_3 are present in both clay fractions. Since Fe oxyhydroxides were previously removed from the samples and any other accessory minerals were not detected, these data suggest that Al, Mg, and Fe are the main cations of the octahedral sites in the clay fractions. K_2O is higher in the 2-0.2 µm fraction due to the higher amounts of illite and illite-rich mixed-layered minerals in this clay fraction, supporting the XRD modeling.

Table 2. Major chemical composition of the clay fractions

Horizon	Na_2O	MgO	Al_2O_3	SiO_2	F_2O_3	P_2O_5	K_2O	CaO	TiO_2	MnO
	%									
< 0.2 µm										
P1CE										
A	< 0.01	19.47	12.59	41.47	8.12	0.14	0.43	0.04	0.51	0.15
C3	< 0.01	7.06	15.81	42.64	10.63	0.09	0.70	0.04	0.60	0.06
C4	< 0.01	4.43	19.01	43.64	7.63	0.11	0.63	0.03	0.63	0.04
P2CE										
A	< 0.01	12.70	14.93	40.80	9.80	0.29	0.60	0.05	0.64	0.08
C2	< 0.01	4.12	17.22	41.45	9.63	0.15	0.61	0.03	0.69	0.04
C3	< 0.01	3.53	19.35	43.47	7.61	0.15	0.63	0.02	0.69	0.03
P1RJ										
A	< 0.01	6.95	14.67	44.89	11.47	0.18	2.27	0.05	0.69	0.08
C2	< 0.01	6.07	13.15	41.87	11.94	0.19	1.70	0.04	0.66	0.07
C3	< 0.01	5.85	14.78	44.47	10.23	0.17	1.51	0.03	0.67	0.05
P2RJ										
A	< 0.01	6.26	14.12	44.05	11.93	0.20	2.28	0.04	0.66	0.07
C1	< 0.01	5.28	13.81	42.20	12.42	0.28	1.73	0.03	0.65	0.06
C3	< 0.01	5.83	14.42	42.62	10.41	0.23	1.37	0.03	0.71	0.06
0.2 – 2 µm										
P1CE										
A	< 0.01	21.91	10.68	38.74	8.06	0.10	1.44	0.09	0.95	0.09
C3	< 0.01	8.27	13.67	38.59	9.72	0.07	2.67	0.11	1.70	0.08
P2CE										
A	< 0.01	13.79	14.91	41.17	10.23	0.10	2.74	0.11	1.70	0.09
C2	0.09	4.07	16.12	50.42	7.58	0.06	3.51	0.45	1.48	0.05
C3	< 0.01	4.78	19.35	45.27	8.38	0.08	2.90	0.07	2.09	0.05
P1RJ										
C2	< 0.03	2.64	13.49	37.90	7.80	0.07	2.66	0.11	1.31	0.06
C3	< 0.01	3.34	18.49	47.20	6.97	0.08	2.67	0.11	1.48	0.05
P2RJ										
A	< 0.01	3.22	15.98	41.49	7.66	0.08	3.06	0.11	1.49	0.06
C1	< 0.01	2.83	15.57	37.93	7.72	0.07	2.43	0.06	1.08	0.04
C3	< 0.01	3.15	18.41	45.46	7.14	0.08	2.55	0.09	1.31	0.05

TEM-EDS analysis was performed to check the chemical composition of individual mineral grains in the soil clay fraction (Table 3). Kaolinite-rich and smectite-rich K-S grains were identified by comparing their composition to standard kaolinite and smectite minerals (Newman and Brown, 1987). Smectite-rich K-S have different Al_2O_3 and MgO contents, suggesting the coexistence of trioctahedral and dioctahedral smectites layers within the K-S minerals. The MgO content varies from 1.4 to 20.2 % in the < 0.2 µm fraction and 0.6 to 30.5 % in the 2 - 0.2 µm fraction, with the highest MgO values in the upper horizons. The high MgO contents detected for smectite-rich K-S grains support the XRF data and the interpretations made for the 06,33 peaks, confirming the presence of trioctahedral smectite layers in the samples. Crystals with different K_2O content were also detected (varying from 0.2 to 7.7 %) and are likely related to illite layer in the mixed-layered minerals. However, even the highest

K_2O contents are below the typical values reported for standard illite minerals (Newman and Brown, 1987). This can be interpreted as a chemical effect of the mixed-layering within the smectite minerals (Huggett and Cuadros, 2010; Andrade et al., 2018), supporting thr XRD modeling and XRF data (Table 3).

Table 3. Major chemical composition of the clay particles from TEM-EDS

Mineral	SiO_2	Al_2O_3	MgO	FeO	CaO	K_2O	Na_2O
	---------- % ----------						
0.2 – 2 µm							
A horizon – P1CE							
K-S	51.9	12.2	30.5	0.5	0.1	0.2	1.41
K-S	53.7	30.1	8.7	1.1	0.3	0.3	3.0
K-S	46.8	28.6	16.8	2.0	0.0	0.9	3.2
I-S	53.5	29.0	8.9	1.3	0.0	1.6	1.6
S-V	57.1	26.0	8.4	1.1	0.0	0.0	0.0
C3 horizon – P1CE							
K-S	55.4	37.9	2.0	0.7	0.1	0.0	1.8
K-S	60.7	34.2	0.6	0.7	0.0	0.3	0.3
I-S	51.3	30.9	6.8	1.4	0.1	1.4	5.8
I-S	54.8	28.9	0.4	3.3	0.9	0.7	1.0
K	52.0	43.9	0.0	3.1	0.4	0.1	0.1
A horizon – P1RJ							
K-S	50.4	25.1	16.3	1.5	0.0	1.2	3.2
K-S	56.7	32.1	1.7	0.8	0.1	0.2	2.8
I-S	47.3	23.5	0.6	3.0	0.0	7.7	1.4
S	60.3	30.2	0.2	5.4	1.4	0.0	0.0
< 0.2 µm							
A horizon – P1CE							
K-S	49.1	23.8	20.2	5.0	0.0	0.5	0.0
K-S	52.0	29.4	12.3	2.2	0.0	0.2	0.3
K-S	52.0	41.0	1.4	0.2	0.0	0.2	1.8
K-S	56.3	32.2	6.1	1.2	0.0	0.1	2.9
I-S	53.4	28.5	6.6	3.1	0.3	1.6	1.8
I-S	51.5	16.5	11.0	9.4	0.1	3.9	0.5
C3 horizon – P1CE							
K-S	54.9	33.1	2.5	1.9	0.0	0.4	0.8
K-S	59.1	33.7	3.3	1.6	0.1	0.1	0.2
K-S	64.4	27.7	1.6	2.7	0.0	0.0	0.2
I-S	51.9	31.7	2.5	2.8	0.0	4.6	2.4
I-S	59.2	22.9	2.5	0.9	0.0	1.9	3.9
A horizon – P1RJ							
K-S	49.5	22.9	18.4	1.9	0.1	0.3	5.8
K-S	53.6	34.8	2.2	1.1	0.0	0.1	4.3
I-S	53.5	37.3	1.7	0.6	0.9	2.7	1.2
K-S	54.0	27.6	0.7	2.9	0.0	0.4	1.2

4.3.3. FTIR study

Fig. 3 shows the FTIR spectra of the clay fractions for the P1CE and P1RJ soil profiles. The 3,600 cm^{-1} band arises from the internal OH groups, and the 3,697 cm^{-1} band is assigned to the internal surface OH groups of kaolinite. These bands appear in all spectra because of the high amount of kaolinite layers in the samples. The doublet near 3,652 and 3,659 cm^{-1} are also related to kaolinite, but their broadening or absence indicates the presence of disordered kaolinite and K-S mixed-layered minerals in the samples (Cuadros and Dudek, 2006). These bands are more pronounced for the coarser fraction of the deeper horizons (e.g. P1RJ) and are due to higher Nmax and Nmed values of the kaolinite end-member and kaolinite-rich K-S phases (Table 1).

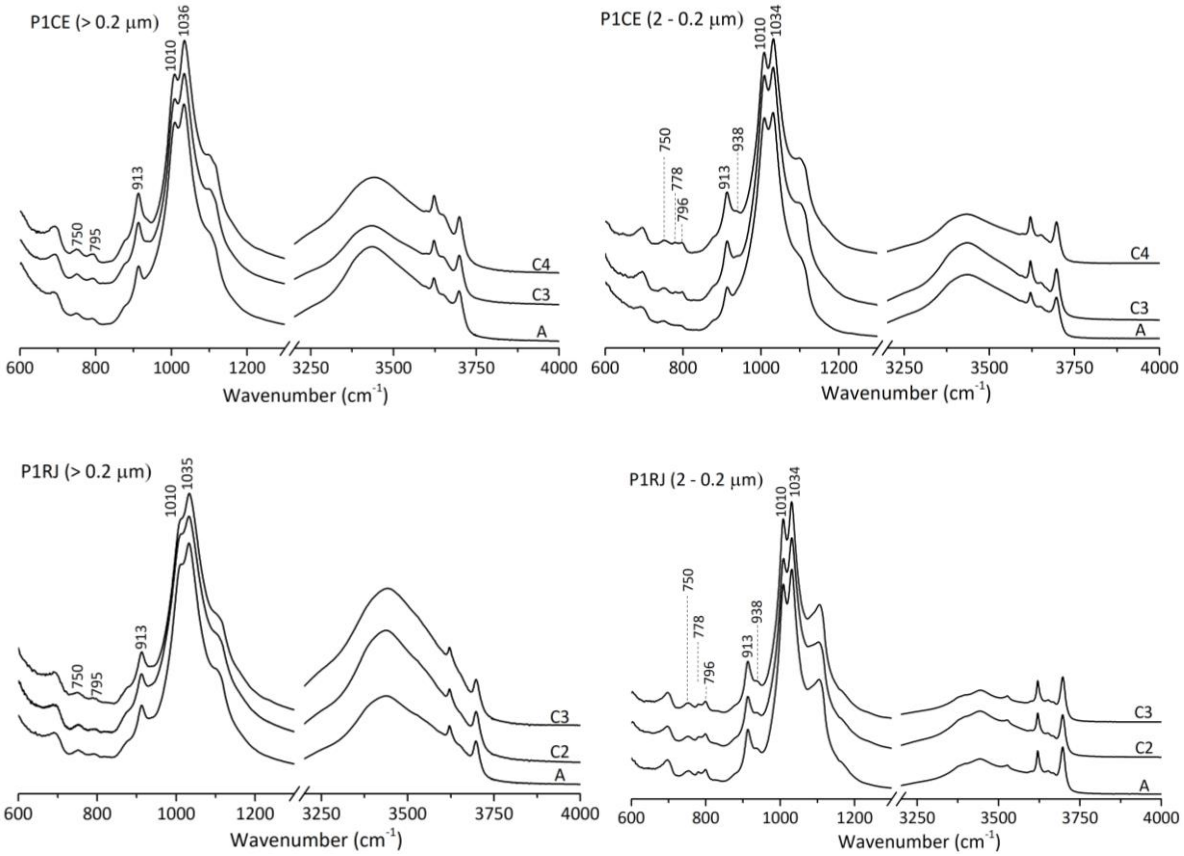

Fig. 3. FTIR spectra of the soil samples

Well resolved bands at near 1,034 and 1,010 cm^{-1} in the 2 – 0.2 µm fraction are likely because of the greater particle size and crystal order of kaolinite when compared to the < 0.2 µm fraction (Russel and Fraser, 1994). In addition, the 938 cm^{-1} band appears for the coarser clay fraction and, together with the 913 cm^{-1} band, is also caused by the presence of kaolinite in the samples. The absence of this band for the finer fraction is because of the higher

amounts of mixed-layered minerals (e.g. K-S) and greater disorder of these minerals. The 880 cm^{-1} band indicates substitution of Al by Fe^{3+} in the octahedra sheet of dioctahedral smectite and/or kaolinite (Russel and Fraser, 1994), which is more prevalent in the < 0.2 μm fraction. These results support the XRD modeling and the TEM-EDS data.

4.4. Discussion

4.4.1. Soil geochemical conditions for clay alteration

Our data show that HTF soils have a complex clay assemblage, containing different mixed-layered phases of detrital and *in situ* origin. The latter may involve the transformation of pre-existing detrital clays and have been reported for other soils formed under saline and/or alkaline conditions (Deconinck et al., 1988; Bouza et al., 2007; Deocampo et al., 2009; Andrade et al., 2018). Considering the total layer proportion of each clay mineral, kaolinite is the predominant mineral in all soils (Table 1). Precipitation of kaolinite from solution is very unlikely to occur since the soil conditions do not favor its formation and stability (Weaver et al., 1975; Dixon, 1989). Therefore, kaolinite reaching the HTFs is assumed to be the main clay mineral of detrital origin, being originated in the highly weathered soils that encompass the study sites.

The main source of detrital kaolinite to the HTF-CE soils are the weathered soils of the coastal Tablelands (Barreiras Group sediments), which are composed mainly of kaolinite (Corrêa et al., 2008). A detrital contribution of Al-rich 2:1 clay minerals is also expected, such as illite, vermiculite, and dioctahedral smectite. These detrital 2:1 minerals have been transported from the poorly-developed soils (Luvisols, Planosols, Leptosols, Cambisols, Calcisols, and Durisols) formed under semiarid conditions (Bétard et al., 2009; Bétard, 2012) and further deposited in the Acaraú River estuary (Diniz, 2010; Andrade et al., 2014, 2018). Predominance of kaolinite in the HTF-RJ soils is also related to sediment inputs from the inland soils (Ferralsols and Lixisols). These soils have been formed from the Serra do Mar regions and under an intense weathering and leaching, leading to the formation of soils rich in kaolinite and gibbsite (Furian et al., 2002; Mendonça-Santos et al., 2007). These sedimentary conditions explain the contribution of kaolinite to the HTF soils, but do not explain the range of mixed-layered minerals detected by XRD modeling and TEM-EDS analysis (Fig. 1 and Table 1).

We believe that four crucial geochemical factors governing the formation of new clay mineral phases other than kaolinite in HTF soils: i) availability of cations in the soil system (Gill and Yemane, 1999; Andrade et al., 2018), ii) high evaporation rates (Darragi and Tardy, 1987), iii) high H_4SiO_4 availability (Andrade et al., 2018), and iv) redox cycles (Huggett and Cuadros, 2005). The first factor is maintained by the constant input of seawater within the soil profiles (Albuquerque et al., 2014b), which explains the high EC values (84 to 130 dS m^{-1}) and soluble cation concentrations in the soils (Mg^{2+}, Ca^{2+}, K^+, and Na^+, Table 4). The second factor is essential to enhance mineral formation due to the increase in concentration of soil porewater and cation activities (Gac et al. 1977; Darragi and Tardy, 1987; Hover et al., 1999). The third factor is crucial for the formation of 2:1 structures within the clay minerals during the mineral alteration. The latter factor seems to be controlled by a combination of climatic local settings and the availability of biogenic Si forms. In the HTF-RJ soils, H_4SiO_4 concentrations (30.9 to 91.2 mg L^{-1}) are substantially higher than those of HTF-CE soils (0.6 to 2.9 mg L^{-1}). This difference is likely due to the lower weathering rates in soils of semiarid conditions (HTF-CE), which reduces the H_4SiO_4 release from minerals to the riverine that reaches the estuary. The forth factor favors fixation of K^+ by smectites and thus illitization.

Table 4. Characteristics of waters from the two uppermost soil horizons of each soil profile

Variable	Unit	P1CE		P2CE		P1RJ		P2RJ	
		A	C3	A	C2	A	C2	A	C1
pH	-	8.1	7.8	8.3	7.6	7.0	6.2	7.1	6.4
Eh	mV	400	465	454	464	508	471	515	480
EC	dS m^{-1}	105.3	111.1	84.2	134.7	106.4	89.0	102.6	130.5
H_4SiO_4	mg L^{-1}	0.8	1.0	0.6	2.9	45.7	91.2	30.9	61.1
Mg^{2+}		2660	1916	2213	2396	2664	2014	2262	2185
Ca^{2+}		557	366	330	533	672	261	391	326
Na^+		34450	17100	20600	26150	32200	16400	21000	21550
K^+		1250	540	650	900	1020	410	590	470
Cl^-		50300	29750	35150	46300	49300	32300	39900	41550
SO_4^{2-}		2543	1385	1846	2183	2719	1085	1553	1692
HCO_3^-		0.3	0.4	0.3	0.5	0.2	<0.1	0.1	<0.1

The very low H_4SiO_4 contents in soil porewater could be a restraint for the formation of 2:1 minerals in the HTF-CE soils. This can be dismissed if the soils contain other Si sources. Based on the Si sequential extraction, amorphous Si (Si_{alk}) phases are the dominant Si fraction of the readily soluble Si pool in HTF soils (59 to 90 % of the extractions). A matrix of amorphous silica-rich phases is likely providing Si for the mineral reactions (Furquim et al., 2010), which is supported by the positive correlation between the Si_{alk} concentration and the

total amount of K-S in the HTF-CE soils for both clay fractions (Fig. 4a). Furthermore, SEM analysis revealed the presence of different biogenic opals in both sites, such as diatoms, sponge spicules, and phytoliths. Biogenic opal can take a direct part in the formation of Mg-smectites and act as a source of H_4SiO_4 for mineral authigenesis as their dissolution proceeds. Apart from that, these amorphous structures can adsorb metals ions and act as a "substrate" for mineral genesis, leading to mineral growth at the expense of the biogenic structure (Hurd, 1973; Badaut and Risacher, 1983).

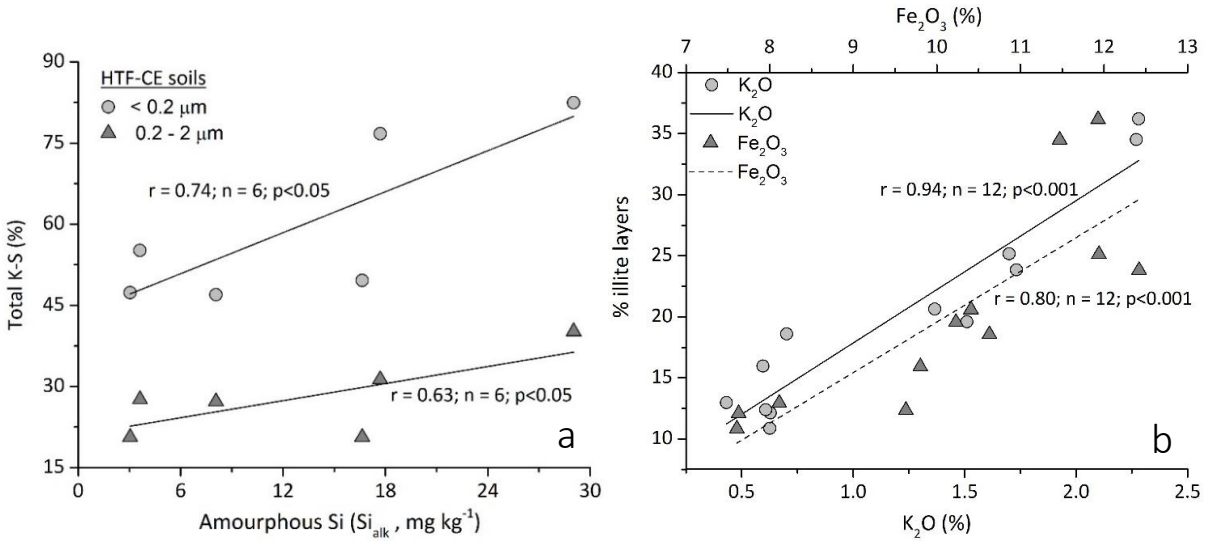

Fig. 4. Correlations between Si_{alk} and total K-S (%), K_2O (%) and % of illite layer, FeO (%) and % of illite layer (b). K_2O (%) and FeO (%) were measured by XRF

4.5.2 Clay alteration

The mechanism of kaolinite illitization through intermediary compositional mixed-layered minerals has been described for mangroves and other hypersaline environments (Huggett et al., 2016; Andrade et al., 2018). Soil conditions in HTFs are propitious for kaolinite illitization as in mangrove soils: i) reducing and oxidizing cycles and hypersaline conditions accelerate K^+ fixation by I-S or S minerals through Fe reduction in octahedral sites and therefore increase in layer charge within the mineral structure, and this step is considered essential for authigenic illitization (Eberl et al., 1986; Huggett and Cuadros, 2005; Koo et al., 2014; Huggett et al., 2016), and ii) K^+ availability in the soil porewater is very high (Table 4), being an essential cation for the illitization process. Fe_2O_3 and K_2O detected in bulk clay samples (Table 2) correlates positively with illite layer proportions in the samples (Fig. 4b), suggesting that the illite formation involves Fe uptake during clay genesis.

Although the soil environment at HTFs favors a reaction pathway similar to those described for mangroves, two important differences can be highlighted. The amounts of Fe-illite endmember phase in the 2-0.2 μm fraction of the HTF-CE soils is substantially lower than those reported for mangrove soils at the same estuary (Andrade et al., 2018); and Fe contents within the clay structure detected by XRD modeling, TEM-EDS, and XRF are lower for HTF soils when compared to Brazilian mangroves (Andrade et al., 2014, 2018). Since Fe is a crucial element for kaolinite illitization and this mineral has low Fe content, the intensity of this process seems to be diminished in HTF soils and clay alteration follows an additional pathway aside from illitization. We believe that Mg is an important element involved in the mineral transformation in HTF soils. Very high Mg values were detected by TEM-EDS for smectite and K-S minerals and also for bulk clay samples (XRF analysis). This is a strong evidence of occurrence of trioctahedral Mg-rich smectite in the soils and is in agreement with the interpretations made for the 06,33 peaks (Fig. 2).

Formation of Mg-rich trioctahedral clays at surface conditions is governed by evaporative concentration of waters, high soluble Mg^{2+} in soil porewater, and solutions undersaturated with H_4SiO_4 with respect to amorphous Si (Harder et al., 1972). All these conditions were found in HTF soils. In addition, the absence of significant HCO_3^- in the porewater (less than 0.5 mg L^{-1}) suppresses dolomite precipitation (Hover et al., 1999), leading to a major control of Mg^{2+} by mineral reactions in the soils. Formation of these Mg-rich clays is likely greater at HTF-CE due to the higher evaporation rates (semiarid climate). Table 2 shows the substantially higher Mg content in the A horizons at HTF-CE when compared to HTF-RJ.

The formation mechanism of smectite trioctahedral layers within the kaolinite and K-S mixed-layered phases is unknown and hard to assess due to the mixture of detrital and in situ transformed clays. We believe that the transformation from kaolinite to trioctahedral Mg-rich smectite is a separated process from kaolinite illitization. In the first case, detrital kaolinite particles are directly transformed to trioctahedral smectite via K-S minerals. Since high amounts of Fe within the mineral structure are essential for the illitization process, the formed Mg-rich smectites are not propitious for illitization. Fe sequential extractions show that most reactive Fe fraction in HTF sois is dominated by lepidocrocite and ferrihydrite (vide item 2.4.2), indicating that Fe precipitates as Fe oxyhidroxides and therefore participates in less extent in clay transformations.

This mechanism involves a progressive chemical reaction, with a transformation from dioctahedral to trioctahedral layers as Mg replaces Al and minor amounts of Fe^{3+} within the kaolinite and K-S structures. K-S minerals are intermediary phases as the reaction proceeds. The reaction is similar to that reported by Deocampo et al. (2009). In this process, the dioctahedral smectite was gradually transformed to trioctahedral smectite in a solid-state reaction without mineral dissolution-recrystallization. The main evidence for this alteration is the existence of di-trioctahedral sheets within the smectite or I-S minerals (Deocampo et al., 2009). In our samples, it was not possible to detect the existence of di-trioctahedral character of the K-S minerals. However, a series of overlapped peaks with di- and trioctahedral character (06,33 peaks, figure 2) and the intermediary chemical composition of the K-S minerals (TEM-EDS analysis, Table 3) are reasonable evidence. In addition, Al and Mg contents are negatively correlated taking into account the minerals kaolinite, smectite, and K-S (Fig. 5a), supporting the progressive transformation from dioctahedral kaolinite to trioctahedral smectite.

In contrast to the process described by Deocampo et al. (2009), the transformation from kaolinite to smectite in HTFs may involve Si uptake from soil solution or biogenic forms. Additional tetrahedral Si sheets have to be incorporated and rearranged into pre-existing kaolinite structure (Cuadros et al., 2017; Andrade et al., 2018). This reaction likely starts at specific points within the crystal structure where the partial dissolution is more feasible to occur, such as crystal defects at the basal surface or lateral edges. The progressive change may continue through internal crystal domains and gradually transform the 1:1 dioctahedral into 2:1 trioctahedral layer. Changes in crystal-ordering are also expected as the reaction proceeds (Andrade et al., 2018). As the number of smectite layer increases, the number of layers in the coherent scattering domain of K-S phases should decrease due to the greater crystal distortion within the clay mineral. This is an effect of the turbostratic disorder generated by the increase in the proportion of smectite layers (Moore and Reynolds, 1997). In fact, there is a negative correlation between the % of smectite layers within the K-S minerals and Nmed (Fig. 5b). Higher Nmed and Nmax values were found for kaolinite-rich K-S and kaolinite end-member minerals, which are likely related to the less altered kaolinite derived from the inland soils.

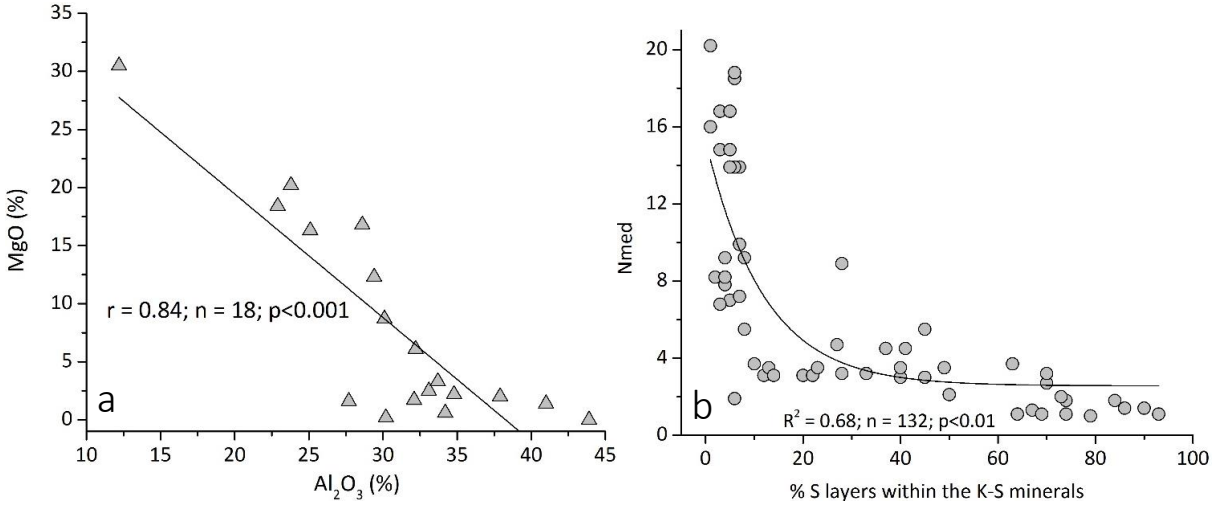

Fig. 5. a) Correlations between Al_2O_3 (%) and MgO (%), and b) % of S layers within the K-S minerals and Nmed. Al_2O_3 and MgO were measured by TEM-EDS. Total K-S (%)

4.5.3 Implications for Si dynamics

Reactions involving clay mineral authigenesis in coastal wetland soils can be relatively fast and impose great control on geochemical cycles of elements in the environment (Michalopoulos and Aller, 1995; Cuadros et al., 2017). These soils receive a constant supply of cations transported by tides, which maintain the system far from equilibrium and trigger multiple mineral reactions, such as clay neoformation and transformation (Andrade et al., 2014; Cuadros et al., 2017). Under the current pedological and climatic conditions, authigenesis of 2:1 and mixed-layered minerals is an active process in HTF soils. Our data show that the soils have a predominance of mixed-layered minerals and low kaolinite end-member contents, indicating that mineral authigenesis is an important reaction controlling Si dynamics in HTF soils. Authigenic mineral components can account for 40 % of the long-term reactive Si storage in some environments, acting as a sink of Si (Presti and Michalopoulos, 2008). We believe that the control over Si dynamics takes place by i) progressive incorporation of Si within mineral structures (Andrade et al., 2018) as a function of porewater concentration (Gac et al., 1977), and ii) opal conversion to various clay minerals through the interaction between clays and the siliceous structures (Badaut and Risacher, 1983; Michalopoulos et al., 2000). These processes likely explain why the concentration of readily available Si forms (e.g. adsorbed Si and soluble Si, vide item 3.4.1) are very low in HTF soils. Experiments carried out by Dixit et al. (2001) demonstrate that formation of clay minerals in detrital-rich sediments control silicic acid concentration in porewater and prevent porewater from reaching equilibrium with amorphous silica. In general, HTF soils have H_4SiO_4

concentrations below the solubility of amorphous Si, which supports our discussion. In view of this, clay authigenesis is an important soil component acting as a sink of Si in coastal wetland ecosystems.

4.6 Conclusion

Evidence of clay mineral transformation in HTF soils was reported in this study. High activity of cations in porewater and predominance of amorphous Si in the readily soluble Si pool create an environment favorable for clay alteration and formation of mixed-layered minerals. Kaolinite is the main detrital clay reaching the HTF soils, but a substantially distinct clay assemblage was detected. We believe that kaolinite is progressively altered to Mg-rich smectite by incorporating Mg and Si within the mineral structures. Biogenic opal seems to be the Si source for mineral alteration and the high Mg activities favor the participation of Mg in the mineral transformation. Soil conditions also favor kaolinite illitization and is likely a process that takes place aside from the transformation from kaolinite to Mg-rich smectite. Nevertheless, Fe participates in less extent in clay transformations due to its precipitation as Fe oxyhydroxides, diminishing the intensity of illitization process in HTF soils. Although our data indicate that detrital kaolinite is altering to other mineral phases through mixed-layering, details of the crystal-chemical reaction remain unknown. Nevertheless, it is clear that clay authigenesis is an important process in HTF soils and therefore imparts an important control on Si dynamics in estuarine environments, acting as a sink Si in coastal wetlands.

References

Albuquerque, A.G.B.M., Ferreira, T.O., Cabral, R.L., Nóbrega, G.N., Romero, R.E., Meireles, A.J.A., Otero, X.L., 2014a. Hypersaline tidal flats (*apicum* ecosystems): the weak link in the tropical wetlands chain. Environ. Rev. 22, 1-11.

Albuquerque, A.G.B.M., Ferreira, T.O., Nóbrega, G.N., Romero, R.E., Souza Júnior, V.S., Meireles, A.J.A., Otero, X.L., 2014b. Soil genesis on hypersaline tidal flats (HTF ecosystem) in a tropical semi-arid estuary (Ceará, Brazil). Soil Res. 52, 140-154.

Andrade, G.R.P., Azevedo, A.C., Cuadros, J., Souza-Júnior, V.S., Furquim, S.A.C., Kiyohara, P.K., Vidal-Torrado, P., 2014. Transformation of kaolinite into smectite and iron-illite in Brazilian mangrove soils. Soil Sci. Soc. Am. J. 78,655-672

Andrade, G.R.P., Cuadros, J., Partiti, C.S.M., Cohen, R., Vidal-Torrado, P., 2018. Sequential mineral transformation from kaolinite to Fe-illite in two Brazilian mangrove soils. Geoderma 309, 84-99

Badaut, D., Risacher, F., 1983. Authigenic smectite on diatom frustules in Bolivian saline lakes. Geochem Cosmochim Ac. 47, 363-375.

Barbiero, L., Berger, G., Rezende-Filho, A.T., Meunier, J.F., Martins-Silva, E.R., Furian, S., 2016. Organic control of dioctahedral and trioctahedral clay formation in an alkaline soil system in the Pantanal Wetland of Nhecolândia, Brazil. PLoS ONE, 11(7).

Bétard, F., 2012. Spatial variations of soil weathering processes in a tropical mountain environment: the Baturité massif and its piedmont (Ceará, Brazil). Catena 93, 18-28.

Bétard, F., Caner, L., Gunnel, Y., Bourgeom, G., 2009. Illite neoformation in plagioclase during weathering: evidence from semi-arid Northeast Brazil. Geoderma 152, 53-62.

Bezerra, F.H.R., Amaro, V.E., Vita-Finzi, C., Saadi, A., 2001. Pliocene-Quaternary fault control of sedimentation and coastal plain morphology in NE Brazil. J. South Amer. Earth Sci. 14, 61-75.

Bouza, P.J., Simón, M., Aguilar, J., del Valle, H., Rostagno, M., 2007. Fibrous-clay mineral formation and soil evolution in Aridisols of northeastern Patagonia, Argentina. Geoderma 139, 38-50.

Brown, G., Brindley, G.W., 1980. X-ray diffraction procedures for clay minerals identification, in: Brindley, G.W., Brown, G. (Eds.), Crystal structures of clay minerals and their X-ray identification. Mineralogical Society, London, p. 205-359.

Conley, J.D., 2002. Terrestrial ecosystems and the global biogeochemical silica cycle. Global Biogeochem. Cy. 16, 1121-2002.

Corrêa, M.M., Ker, J.C., Barrón, V., Torrent, J., Fontes, M.P.F., Curi, N., 2008. Crystallographic properties of kaolinite soils from coastal tablelands: the Amazon and the great bay “Reconcavo Baiano”. Rev. Bras. Cienc. Solo 5, 1857-1872

Cuadros, J., Andrade, G., Ferreira, T.O., Partiti, C.S.M., Cohen, M., Vidal-Torrado, P., 2017. The mangrove reactor: Fast clay transformation and potassium sink. Appl. Clay Sci. 140 (2017) 50–58.

Cuadros, J., Dudek, T., 2006. FTIR investigation of the evolution of the octahedral sheet of kaolinite-smectite with progressive kaolinization. Clay Clay Miner. 54, 1-11.

Cuevas. J., De La Vila, R., Ramirez, S., Petit, S., Meunier, A., Leguey, S., 2003. Chemistry of Mg smectites in lacustrine sediments from the Vicalvaro sepiolite deposit, Madrid neogene basin (Spain). Clay Clay Miner. 51, 457-472.

Darragi, F., Tardy, Y., 1987. Authigenic trioctahedral smectites controlling ph, alkalinity, silica and magnesium concentrations in alkaline lakes. Chem. Geol. 63, 59-72.

Deconinck, J.F., Strasser, A., Debrabant, P., 1988. Formation of illitic minerals at surface temperatures in Purbeckian sediments (Lower Berriasian, Swiss and French Jura). Clay Miner. 23, 91-103.

Deocampo, D.M., Cuadros, J., Wing-Dudek, T., Olives, J., Amouric, M., 2009. Saline lake diagenesis as revealed by coupled mineralogy and geochemistry multiple ultrafine clay phases: Pliocene Olduvai Gorge, Tanzania. Am. J. Sci. 309, 834-868.

Diniz, S.F., 2010. Caracterização fisiográfica e pedológica da região norte do estado do Ceará. São Paulo State University, PhD. Thesis.

Dixit, S., Van Cappellen, P., van Bennekom, A.J., 2001. Processes controlling solubility of biogenic silica and pore water build-up of silicic acid in marine sediments. Mar. Chem. 73, 333-352.

Dixon, J.B., Rees LR, 1989. Kaolin and serpentine group minerals, in: Dixon JB, Weed SB (eds) Minerals in soil environments. Soil Science Society of America Book Series No. 1, Madison, p. 913-974.

Eberl, D., Środoń, J., Northrop, R., 1986. Potassium fixation in smectite by wetting and drying, in: Geochemical processes at mineral surfaces. Ed: Davis JA, Hayes KF, Eds. ACS Symposium Series 323. American Chemical Society, Washington, D.C, p. 296-326.

Furian, S., Barbiéro, L., Boulet, E., Curmi, P., Grimaldi, M., Grimaldi, C., 2002. Distribution and dynamics of gibbsite and kaolinite in an oxisol of Serra do Mar, southeastern Brazil. Geoderma 106, 83-100.

Furquim, S.A.C., Barbiero, L., Graham, R.C., Queiroz Neto, J.P., Ferreira, R.P.D., Furian, S., 2010. Neoformation of micas in soils surrounding an alkaline-saline lake of Pantanal wetland, Brazil. Geoderma 158, 331-342.

Furquim, S.A.C., Graham, R.C., Barbiero, L., Quiroz Neto, J.P., Valles, V., 2008. Mineralogy and genesis of smectites in an alkaline-saline environment of Pantanal wetland, Brazil. Clay Clay Miner. 56, 579-595.

Gac, J.Y., Droubi, A., Fritz, B., Tardy, Y., 1977. Geochemical behaviour of silica and magnesium during the evaporation of waters in Chad. Chem. Geol. 19, 215-228.

Gill, S., Yemane, K., 1999. Illitization in a Paleozoic, peat-forming environment as evidence for biogenic potassium accumulation. Earth and Planet. Sc. Let. 170, 327-334.

Harder, H., 1972. The role of magnesium in the formation of smectite minerals. Chem. Geol. 10, 1-39.

Hesp, P.A., Maia, L.P., Claudino-Sales, V., 2009. The Holocene Barriers of Maranhão, Piauí and Ceará States, Northeastern Brazil, in: Dillenburg, S., Hesp, P. (Eds.), Geology and geomorphology of Holocene coastal barriers of Brazil. Springer-Verlag, Berlin, Heidelberg, p. 325-343.

Hover, V.C., Walter, L.M., Peacor, D.R., Martini, A.M., 1999. Mg-smectite authigenesis in a marine evaporative environment, salina Ometepec, Baja California. Clay Clay Miner. 47, 252-268.

Huggett, J., Cuadros, J., Gale, A., Wray, D., Adetunji, J., 2016. Low temperature, authigenic illite and carbonates in a mixed dolomite-clastic lagoonal and pedogenic setting, Spanish Central System, Spain. Appl. Clay Sci. 132-133, 296-312.

Huggett, J.M., Cuadros, J., 2005. Low-temperature illitization of smectite in the late Eocene and early Oligocene of the Isle of Wight (Hampshire basin), U.K. Am. Mineral. 90, 1192–1202.

Huggett, J.M., Cuadros J., 2010. Glauconite formation in lacustrine/palaeosol sediments, Isle of Wight (Hampshire Basin), UK. Clay Miner. 45, 35-49.

Hurd, D.C., 1973. Interactions of biogenic opal, sediment and seawater in the Central Equatorial Pacific. Geochim. Cosmochim. Ac. 37, 2267-2282.

Koo, T., Jang, Y., Kogure, T., Kim, J.H., Park, B.C., Sunwoo, D., Kim, J., 2014. Structural and chemical modifications of nontronite associated with microbial Fe (III) reduction: indicators of illitization. Chem. Geol. 377, 87-97.

Mayayo, M.J., Bauluz, B., Lopez, J.M.G., 2000. Variations in the chemistry of smectites from the Calatayud Basin (NE Spain). Clay Miner. 35, 365-374.

Mehra, O.P., Jackson, M.L., 1960. Iron oxide removal from soils and clays by a dithionite-citrate system buffered with sodium bicarbonate. Proceedings of the Seventh National Conference on Clays and Clay Minerals. London.

Mendonça-Santos, M.L., Santos, H.G., Dart, R.O., Pares, J.G., 2007. Mapeamento digital de classes de solos no Estado do Rio de Janeiro. Dados eletrônicos, Rio de Janeiro: Embrapa Solos, Boletim de pesquisa e desenvolvimento.

Michalopoulos, P., Aller, R.C., Reeder, R.J., 2000. Conversion of diatoms to clays during early diagenesis in tropical, continental shelf muds. Geology 28, 1095-1098.

Michalopoulos, P., Aller, R., 1995. Rapid clay mineral formation in Amazon delta sediments: reverse weathering and oceanic elemental cycles. Science 270, 614-617.

Moore, D.M., Reynolds, R.C., 1997. X-ray Diffraction and the Identification and Analysis of Clay Minerals, second ed. Oxford University Press, Oxford.

Muehe, D., Lima, C.F., Lins-de-Barros, F.M., 2006. Rio de Janeiro, in: Muehe, D. (Ed.), Erosão e progradação no litoral brasileiro. MMA, Brasília, p. 265-296.

Newman, A.C.D., Brown, G., 1987. The chemical constitution of clays, in: Newman, A.C.D. (Ed.), Chemistry of Clays and Clay Minerals (Mineralogical Society Monograph No. 6). Longman Scientific and Technical, London, p. 1-128.

Presti, M., Michalopoulos, P., 2008. Estimating the contribution of the authigenic mineral component to the long-term reactive silica accumulation on the western shelf of the Mississippi River Delta. Cont. Shelf Res. 28, 823-838.

Reynolds Jr., R.C., Reynolds, R.C., 1996. NEWMOD for Windows. The calculation of one-dimensional X-ray diffraction patterns of mixed-layered clay minerals, Hanover, New Hampshire.

Russell, J.D., Fraser, A.R., 1994. Infrared methods, in: Wilson M.J. (eds) Clay Mineralogy: Spectroscopic and Chemical Determinative Methods. Springer, Dordrecht, p. 11-67.

Ryan, P.C., Huertas, F.J., 2013. Reaction pathways of clay minerals in tropical soils: insights from kaolinite-smectite synthesis experiment. Clay Clay Miner. 61, 303-318.

Schaefer, M.V., Guo, X., Gan, Y., Benner, S.G., Griffin, A.M., Gorski, C.A., Wang, Y., Fendorf, S., 2017. Redox controls on arsenic enrichment and release from aquifer sediments in central Yangtze River Basin. Geochim Cosmochim Ac. 204, 104-119.

Sommer, M., Kaczorek, D., Kuzyakov, Y., Breuer, J., 2006. Silicon pools and fluxes in soils and landscapes - a review. J. Plant Nutr. Soil Sci. 2006, 169, 310-329.
Souza-Júnior, V.S., Vidal-Torrado, P., Garcia-Gonzaléz, M.T., Otero, X.L., Macías, F., 2008. Soil mineralogy of mangrove forests from the state of São Paulo, southeastern Brazil. Soil Sci. Soc. Am. J. 72, 848-857.

USDA, 2014. Soil Survey Field and Laboratory Methods Manual. United States Department of Agriculture Natural Resources, Conservation Services (NRCS) (Soil Survey Investigations Report No. 51, Version 2.

Weaver, R.M., Jackson, M.L., Syers, J.K., 1975. Clay mineral stability as related to activities of aluminium, silicon, and magnesium in matrix solution of montmorillonite-containing soils. Clay Clay Miner, 24, 246-252.